الجمهورية الجزائرية الديمقراطية الشعبية
REPUBLIQUE ALGERIENNE DEMOCRATIQUE ET POPULAIRE
وزارة التعليـــم العالـــي والبحـــث العلمـــــــي
MINISTERE DE L'ENSEIGNEMENT SUPERIEUR ET DE LA RECHERCHE SCIENTIFIQUE

جـامـعـة فرحات عباس- سطيــف-1

UNIVERSITE FERHAT ABBAS - SETIF 1

UFAS (ALGERIE)

THESE

Présentée à la Faculté de Technologie
Département d'électrotechnique
Pour l'obtention du Diplôme de

DOCTORAT EN SCIENCES

Option : **Machines Electriques**

Par

Mr. BENDIB Mohamed Elhadi

Magister dans les Machines Electriques Université de Batna
Ingénieur d'État en Électrotechnique Université de Sétif

Thème

Contribution a l'étude et la commande d'une machine synchrone à aimants permanents

Soutenu le **...**……**.....** *devant un Jerry composée de :*

Mr. …….....	Pr. Université de ……	Président
Mr. HACHEMI Mabrouk	Pr. Université de Sétif-1-	Rapporteur
Mr. FABRIZIO Maregnetti	Pr. Université de Cassino (Italie)	Co-Rapporteur
Mr. ……	Pr. Université de……..	Examinateur
Mr. …….	Pr. Université de …….	Examinateur

ملخص:

في هذه الأطروحة قمنا بدراسة آلة كهربائية متزامنة ذات مغناطيس دائم مهجنة بين الآلات ذات التدفق المحوري و التدفق العرضي فتحقق كثافة عزم دوران عالية. الخطوة القطبية للعضو الساكن والمتحرك هي نفسها. الآلة مناسبة لتربينات الرياح. كما يمكن آن تكون الآلة متعددة الأوجه. الجزء الساكن للآلة يحتوى عل مجموعة من الأقطاب الزوجية متجاورة على شكل حرف U وذوى ملف حلقي، أما العضو المتحرك يحتوي علي زوجين من المغناطيس الدائم، مجموعة في الجهة الداخلية ومجموعة ثانية في الجهة الخارجية. الشكل الخاص لأقطاب الجزء الساكن يسمح بتغيير مسار التدفق المغناطيسي دون تغيير قطبية التغذية. المعادلات التحليلية عند عدم التحميل للقوة الكهربائية وعزم الدوران قد تم استنباطها وهذا بعد تطوير النموذج المغناطيسي المكافئ (CEM). لتحليل المجال المغناطيسي تم استخدام طريقة العناصر المحدودة (EF).

كلمات مفتاحيه: آلة ذات تدفق محوري، آلة ذات تدفق عرضي، عزم الدوران، العناصر المحدودة (EF)، النموذج المغناطيسي المكافئ (CEM)، ممانعة مغناطيسية، آلة متزامنة، لف حلقي.

Résumé :

Cette thèse analyse nouvelle machine synchrone à aimants permanents (PM) à flux axial- transversal hybride a une densité de couple élevée. Le pas polaire du stator et le pas polaire du rotor sont les mêmes. La machine est destinée aux systèmes à éoliennes. La nouvelle machine transversale axiale a un entrefer simple ou double face. La machine a deux noyaux de stator en forme de quasi-U et adjacents avec un enroulement de type annulaire, et le rotor a deux groupes d'aimants, l'un externe et l'autre interne. La forme du noyau du stator quasi-U permet de modifier le trajet du flux sans modifier la polarité de l'alimentation. Les expressions analytiques de la FEM sans charge et le couple sont dérivées, après le développement de ce modèle de circuit d'équivalence magnétique (MEC). La méthode des éléments finis 3D (FE) est utilisée pour analyser le champ magnétique, le couple, et le couple de détente pour les différentes inclinaisons d'aimants.

Mots clés: machine à flux axial, machine à flux transversal, couple de détente, éléments finis (EF), circuit magnétique équivalent (CME), circuit à réluctance, machine synchrone, enroulement annulaire.

Abstract :

This thesis analyzes a novel hybrid axial-transverse flux permanent magnet (PM) synchronous machine achieving high torque density. The stator pole pitch and the rotor pole pitch are the same. The machine is suitable for wind turbines. The new axial transverse machine has a single-sided or double-sided air gap. The machine has two adjacent quasi-U stator cores with ring-type winding, and the rotor has two PM groups, one outer and one inner. The shape of quasi-U stator core allows changing the flux path without changing power supply polarity. The analytical expressions of the no-load back-EMF and the torque are derived, after the development of 3-D magnetic equivalent circuit (MEC) model. The 3-D finite element method (FE) is used to analyze the magnetic field, torque, and cogging torque for different skewing of the PMs.

Keywords: axial flux machine, transverse flux machine, cogging torque, finite element (FE), MEC circuit model, reluctance circuit, synchronous machine, ring winding;

Remerciements

A l'issue de ces années de thèse, et avant que ce manuscrit ne suive son propre chemin, je tiens à remercier tous ceux qui ont contribué de près ou de loin à la bonne conduite de ma thèse.

***Le** travail présenté dans cette thèse a été effectué sous la direction de Monsieur Fabrizio Maregnetti Professeur à Universita Degli Studi Di Cassino E Del Lazio Meridionale, Italie. Je tiens à le remercier pour la confiance qu'il m'a témoignée en acceptant de Co-encadrer ce travail. Sa disponibilité et ses encouragements mon été d'un grand apport pour l'aboutissement de ce travail.*

***Je** remercie infiniment Monsieur HACHEMI Mabrouk Professeur à l'Université Ferhat Abass de Setif. Pour la confiance qu'il m'a témoignée en acceptant de diriger ce travail. Je tiens à exprimer ma haute reconnaissance pour sa contribution scientifique qui a été très fructueuse dans l'avancement de ce travail.*

Dédicace

Je dédie ce modeste travail à :

Mes chers parents qu'ALLAH les protège ;

Ma femme

Mes chers enfants Acil et Meryem

Mes frères et sœurs ;

Sans oublier tout mes amies de l'université.

Mohamed EL Hadi

Contents

Chapter Two

A-TFPMS Machine Construction and Design Variations

Chapter Three

3D-FEA and Analytical Modeling

Chapter Four

MEC Study of Axial-Transverse Flux Permanent Magnet Machine

List of Figures

Chapter 1

Chapter 2

Chapter 3

Chapter 4

List of Tables

Publications

A- Internationals Publications

1. Bendib M, Hachemi M, Marignetti F. "electromagnetic Design and Analysis of a Novel Axial-Transverse Flux Permanent Magnet Synchronous Machine", **Electric Power Components and Systems**, DOI:10.1080/15325008.2017.1310954.Volume 45, Issue8, 2017.

2. Bendib, M.; Belhouchat, K.; Hachemi, M.**,** "3D Finite Element Analyses and Design Optimization of AFPM for Flywheel Energy Storage System". **IEEE Conference Publications**, 2015.

B- Internationals Conferences

1. **BENDIB, M.,** "Efficient Pole-Arc Coefficients for Maximum Flux Leakage in Axial Flux Permanent Magnet DC Machine Double Gap ", IEEE ICEE, Algiers, May 2012.
2. **BENDIB, M.,** ABDELHADI, B., BENOUDJIT, A., "Design and Optimization Axial Flux Permanent Magnet DC Machine Double Gap ", CEE, Batna, October 2012.
3. **BENDIB, M.,** ABDELHADI, B., BENOUDJIT, A., "Design and Optimization of Axial Flux Permanent Magnet DC Machine Double Gap ", ICPEED, Oran, December 2012.
4. **BENDIB, M.,** HACHEMI, M., "Design and Optimization by Using GA and PSO of Axial Flux Permanent Magnet DC Machine With Double Gap ", ICEEAC, Setif, November, 2013.
5. **BENDIB, M.,** BELHOUCHET, K., HACHEMI, M.," Modeling and Optimization By 3D Finite Elements of AFPM For Flywheel Energy Storage System", IECEC, Sétif, May 2015.
6. **BENDIB, M.,** BELHOUCHET, K., HACHEMI, M.," 3D Finite Elements Analyses and Design Optimization of AFPM For Flywheel Energy Storage System", CEIT, Tlemcen May 2015.
7. **BENDIB M.,** M. Hachemi, K. Belhouchat,"Axial Flux Permanent Magnet Torus Moto Design Using Sizing Equation and FEA", CEE, Batna, 2016.
8. **BENDIB M.,** M. Hachemi, K. Belhouchat," V-Interior Permanent Magnet Machine Optimization and Transient 3D Finite Element Analyses", CEE, Batna, 2016.

Introduction

Today, the expected performance of electrical machines is becoming higher; simultaneously costs and design time are significantly reduced. Similarly, the cost of prototypes is increasingly prohibitive and especially as the power of the machine increases. In order to avoid the construction of prototypes for test and validation of a machine, computer-aided design software is required. The latter have developed as the computing tools raise and their power grows each year. These software's allow the development and validation of machines with a relatively low cost. At the same time, the demand for design quality increases, so that the various operating modes of the machine design must be taken into account and simulated.

It is not uncommon for a designer of electric machines to state that the principles of machine design have been established over 100 years ago and have not changed since and therefore only leave room for small improvements. In recent years this prejudice has given way due to dramatic advances in material science in the area of permanent magnet materials and the introduction of the new machine topology.

The transverse flux machine, as it will be referred to here, has a magnetic flux path with sections where the flux is transverse to the rotation plane. There are three general concepts for transverse flux machines: C-core, E-core, U-core and claw pole. In TFPMSM with U-type stator cores, the cores of each phase are displaced of twice the pole pitch, and half of the permanent magnets are inactive. Therefore the machine is characterized by a large rotor flux leakage. In fact, in the U-shape TFPMSM, the number of PMs is twice the number of cores. In the C-type, E-type, and other stator core pieces, the flux direction is the same, and the stator core pieces are spaced twice the pole pitch

The small size and the low weight makes transverse flux motor a superior choice for mobile applications such as hub motors for electrical vehicles. Several implementations of variable speed active rotor transverse flux hub motors for wind energy can be found in the literature that confirm the high torque capability and high power to weight ratios achievable with those machines. Avoiding the need for a gearbox reduces the overall weight of the

drive system significantly. Other applications of transverse flux motors, such as ship drives and train drives show the successful implementation of this motor type in a wide range of drive applications. The light weight transverse flux machine allows for new train concepts with a distributed drive system. A distributed drive system also eliminates the need for a heavy weight drive head. Which reduces the track construction cost significantly because of the lower stresses imposed on the driveway.

For variable speed applications it is also beneficial that transverse flux motors with field magnets have a large operating frequency range: due to their favorable behavior when operated under field weakening conditions. This beneficial behavior is caused by the large inductance of the armature winding.

The large armature winding induction results in a low power factor this low power factor cannot be eliminated within the machine through design changes and must be taken as a price that must be paid for the high Specific torque output. The price for the low power factor is paid explicitely for the converter design that must have a higher VA rating, or preferably the converter compensates for the low power factor through a power factor correction design. Therefore closed loop control with a position encoder on the shaft is required for a variable speed drive using transverse flux machines.

Another advantage is that the phases are electromechanically decoupled as the phases are separated. Also, the position of the rotor or stator parts can be varied in the circumferential direction to decrease cogging torque. Another advantage is that there is no need for end windings.

The first step is to take search about the new structures in order to identify the main characteristics and the performances specific to each structure. This first step will be essentially bibliographic and will highlight the essential elements of the proposed structures and analyze their advantages and disadvantages. This analysis will include physical aspects as well as aspects related to manufacturing and industrialization. Indeed, it does not seem useful to develop a structure that is certainly powerful, but difficult or impossible to achieve at the industrial level. At the end of this first phase, most of the existing machines will be exposed. A classification will be realized. This will

help in the selection of existing structures that are considered interesting or in the definition of an original structure. These structures will meet criteria for both intrinsic performance and industrial feasibility.

One of the new items of research that we propose in this thesis is the study of new structure of electrical machines carried out using recent modeling tools, and new materials using at present. This thesis is divided into four chapters, whose content is organized from the following way:

The first chapter provides a general overview of various permanent magnet synchronous machines. In beginning the radial flux machine followed by axial flux machine and the transverse flux machines are the last. The emphasis is placed on the transverse flux topology and its principles of operation, performances, advantages and disadvantages. Various configurations of transverse flux topologies are reviewed and their properties are outlined. In the last chapter we have done a preview about the wind power generation and their characteristics.

The second chapter comprises calculations of the geometry dimensional, magnetic parameters and windings values of an axial-transverse flux PMs synchronous machine with the use of analytical calculation combined with finite element analysis as primary design tool. The leakage permeances are calculated by geometry methods. The equivalent electric circuit of this machine is presented. The efficiency estimation is the fruit of all different losses calculations. The mechanical constraints are also necessary during the design features; the main task is making the clearance (air-gap) constant as possible.

The third chapter deals with two-dimensional, three-dimensional static and transient finite element analyses of an axial-transverse flux permanent magnet machine at no-load condition. The dimensions of the magnetic circuit are analytically computed are calculating in the previews chapter are inserted into a FEM-software. The machine employing two transverse flux topologies: The basic topology utilizing three phases for one face and the one utilizing only one phase for each face are evaluated. The analysis of the torque and of the back-EMF is developed. The skewing permanent magnet of the studied

machine is used with the help of finite element method (FEM) calculations to calculate cogging torque.

The fourth chapter applies the results of the studies conducted in the two previous chapters to estimate the electromechanically dimensions and performance of axial-transverse flux PMs synchronous machine. In addition to using equivalent model to predict output performance of electric machinery, magnetic equivalent circuits have been used to predict flux density magnitudes within electric machinery. air-gap flux density results from models presented in compare with finite element calculations, and demonstrate the possibility of the MEC method replacing FEM, as a primary design tool, for some applications.

This method shows a good agreement with the FEM analysis and thus can be used to reduce calculation time, as the need for the rather time consuming dynamic FEM simulations is eliminated. The flux loop reluctance network model is typically used, to use MEC model the approximation equations of permeability are presented, the reluctance network MEC predicts the spatial distribution of air gap flux density, the back EMF and the electromagnetic torque. This analysis can help the designers of transverse flux machines to select the appropriate set of dimensions when opting for the desired performance.

Conclude this thesis by summarizing the presented work. Some guidelines for future work are outlined.

Chapter One

State of the Art on Permanent Magnet Machines

Chapter One

State of the Art on Permanent Magnet Machines

1. Introduction

Nearly almost of electric machines used in industry uses technologies known for a long time: asynchronous and synchronous machines. For some decades now, the electric machine designers studying new structures (permanent magnet or reluctance machines with axial, radial or transverse flux). These innovations are possible thanks to technological advances in power electronics, materials and numerical calculations.

The aim of this chapter is analyzing the technology and design of the existing machine concepts and discuss the potential structures, in this chapter we will give an overview of the family of electrical machinery radial flux, axial flux and transverse flux, their operating principles and their designs and also the purpose of this chapter is to select one machine with strong industrial potential for further analysis that we will conduct thereafter.

2. Machines Technology

In reality we have lot off machines structure, the task is how can classify them, and try to take the flux direction as criterion.

2.1. Flux Directions

For synchronous PM machines there are three types of structures: the radial flux structure, the axial flux structure and the transverse flux structure. The radial flux machine is most used. The flux in the air gap is radials to the axis of rotation of the machine (Fig. 1.1). For the axial flux machine, the flux in the air gap is axial to the axis of rotation of the machine (Fig. 1.2). For very specific applications, such as direct drive and low speeds, designers have introduced the transverse flux machine (Fig. 1.3). The flux is both axial and radial to the axis of rotation of the machine.

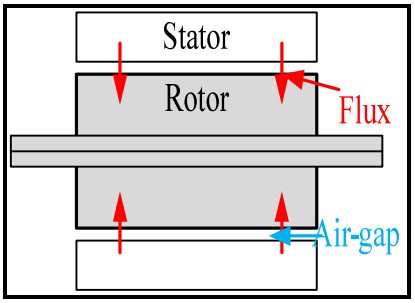

Fig.1.1: Radial flux machine.

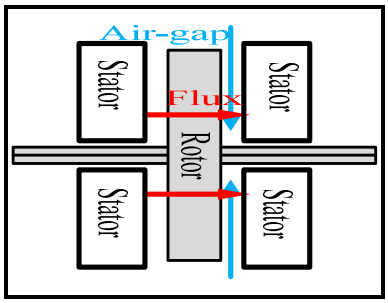

Fig.1.2: Axial flux machine.

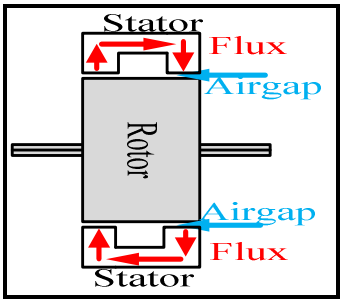

Fig.1.3: Transversal flux machine.

2.2. Windings

There are three main ways of winding an electrical machine: the distribute winding, the concentrated winding and in Gramme ring winding. The distribute winding is show in Fig. 1.4 and Fig. 1.7. The main disadvantage of this winding type is the ends winding, since they are source of Joule losses.

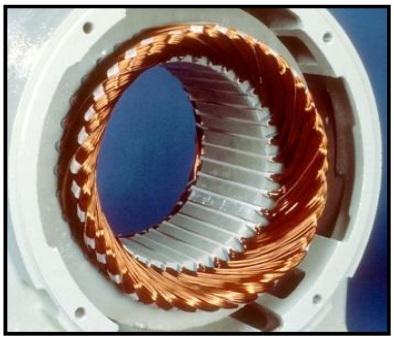

Fig. 1.4: Distributed winding [1].

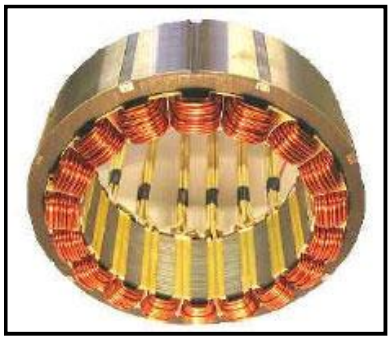

Fig. 1.5: Concentrated winding [2].

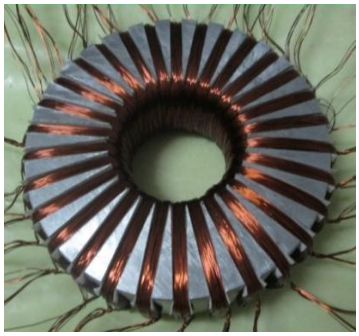

Fig. 1.6: Gramme Winding [3].

Therefore, electrical machinery designers have developed the concentrated (Fig. 1.5 and Fig. 1.8). The coil includes only a tooth instead of more teeth to the left winding. By this method, the end winding are reduced and therefore the Joule losses reduced. Although more frequently used in electrical machines. For very particular machines, the winding ring is formed Gramme (Fig. 1.6 and Fig. 1.9). This winding is made up of several rings along the stator. Easy to design, it is very suitable for the radial or the axial Torus machine double gap. However the Joule losses handicap this winding type.

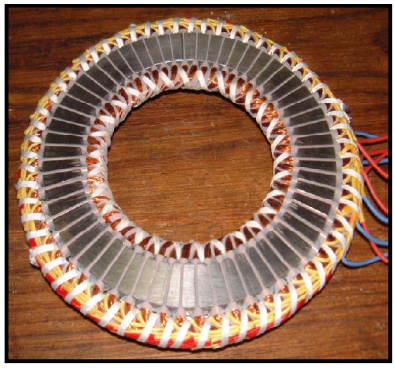

Fig. 1.7: Distributed winding [4].

Fig. 1.8: Concentrated winding [5]

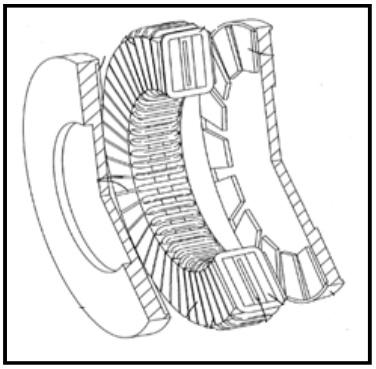

Fig. 1.9: Gramme Winding [1].

As we show in the previous discussions about the winding of electrical machines especially radial and axial configurations, after my bibliography researches I found only tow transversal windings types, the first is full ring (toroidal) winding and the second is portion ring winding[7].

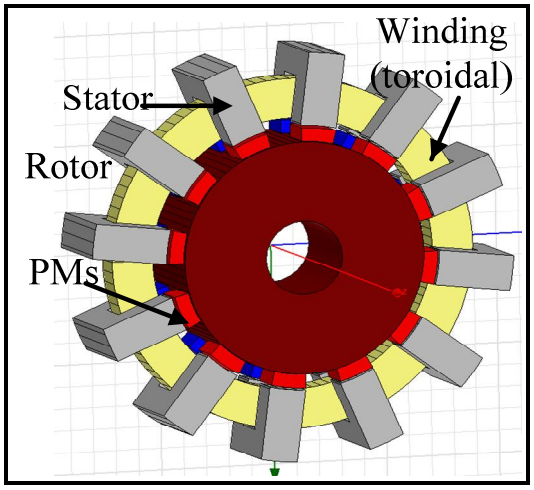

Fig. 1.10: Ring (toroidal) winding [6].

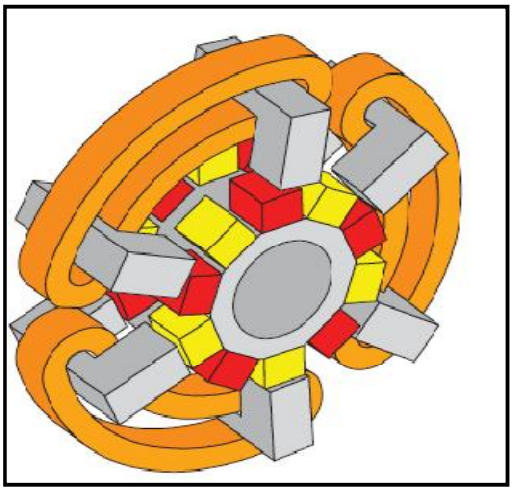

Fig. 1.11: Ring portion winding [7].

3. Choosing the Innovative Concept

3.1. Radial Flux Machines

The radial flux synchronous machine is the first permanent magnet machine appeared in the industry. Due to advances in power electronics and PM performances, it begins to replace the asynchronous machine. The first radial flux synchronous machine being developed as surface magnets machine distributed winding (Fig. 1.12). In literature, it is possible to find it to fit a turbocharger (50kW 70000 rev/min, 8 poles) [8] or in the automotive field (40kW 6000 rev/min, 4 poles) (6kW, 6000 rev/min, 12 poles) [9] [10]. These studies highlight the performance and power density compared with asynchronous machines. At present, this structure with simple gap frequently used as reference when make comparison with innovative machines [11] [12] [13]. The major drawback of this machine is the location of the magnets.

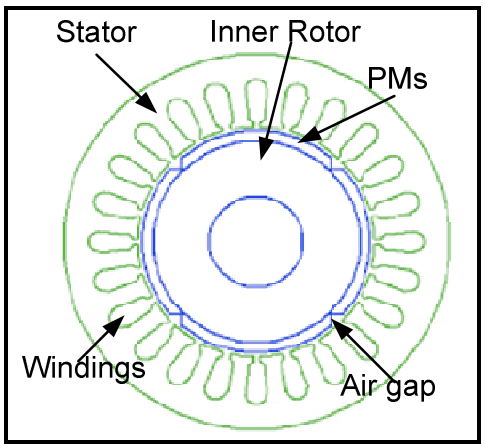

Fig. 1.12: Interior rotor PM synchronous machine.

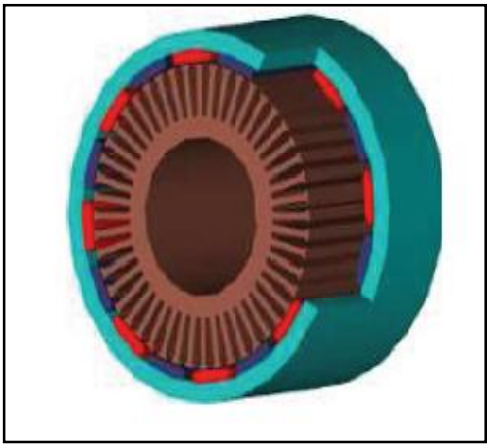

Fig. 1.13: Outer rotor PM synchronous machine.

The rotor of the machine can be placed outside the stator (Fig. 1.13), to reduce the risk of disconnection of the magnets. The wind turbine application (20kW, 210 rev/min, 36 poles) [14] and elevator are also good examples.

Indeed, the synchronous inductance distributed winding SPM is relatively small because of the relative permeability of the permanent magnets close to unity and the importance of the gap while the flux from PM can be reduced.

The other alternative of the magnets disconnection is burying the magnets, leakage flux of burying magnet is significantly decreased and especially the

magnets are used in flux concentration. In [15] has used this concept to study a prototype (11kW, 2000 rev/min, 12 poles) (Fig. 1.14) for vehicle application.

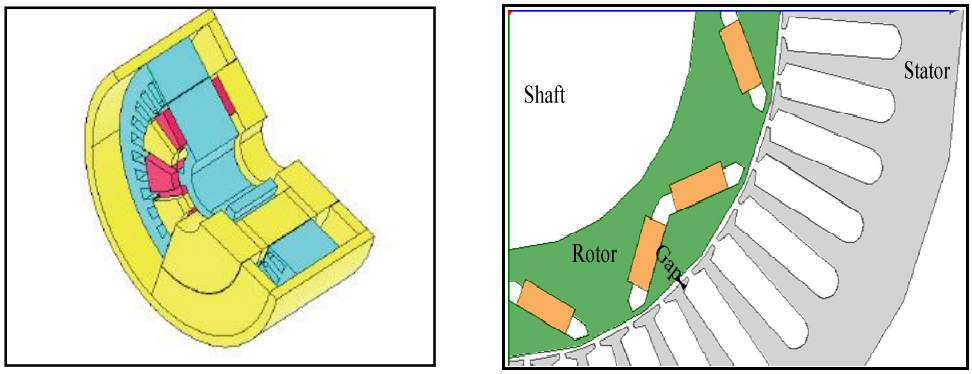

Fig. 1.14: Distributed winding and buried PM [15].

Fig 1.15: Distributed winding V-interior PM [16].

In the same application, [10] and [17] show that burying magnets, they can reduce noise and increase the field weakening capacity without changing the electrical performance of the machine (6kW, 6000 rev/min, 12 poles) (Fig. 1.15). Many papers studied on optimization [11], location, and shape of the magnets [18] [19]. The combination outer rotor and buried magnets have been studied in [20].

However, the distributed winding has Joule losses significant due the ends coils. To solve this problem, designers have thought of concentrated winding [21]. This winding type is interesting in industry (Fig. 1.16).

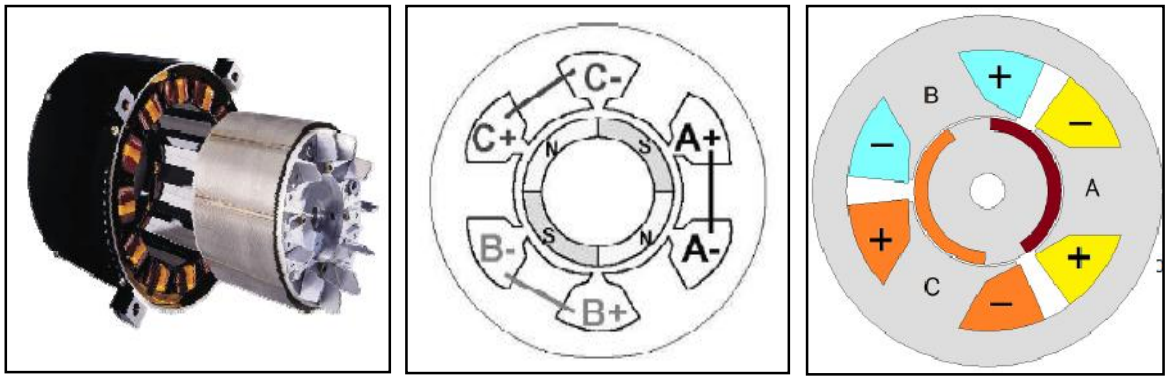

(a) (b) (c)

Fig.1.16: (a) Concentrated winding (Leroy Somer), (b) one phase per slot, (c).two phases per slot.

The buried magnet applications are similar to those of the distributed winding, in vehicle applications exposed by [15] with a prototype 11kW, 2000 rev/min, 12 poles and [22] which the machine delivers a power of 280W to 3000 rev/min with 4 poles.

In other papers, the authors attempt to examine specific items of their machine as iron losses [23] as support with a machine 750W, 4800 rev/min and 4 poles or compare with distributed winding machines [15]. [24] Analyzing the possibility of establishing an outer rotor to directly attach the blades of the ventilation system on the engine. He developed a machine of 230W, 4 poles getting 90% efficiency.

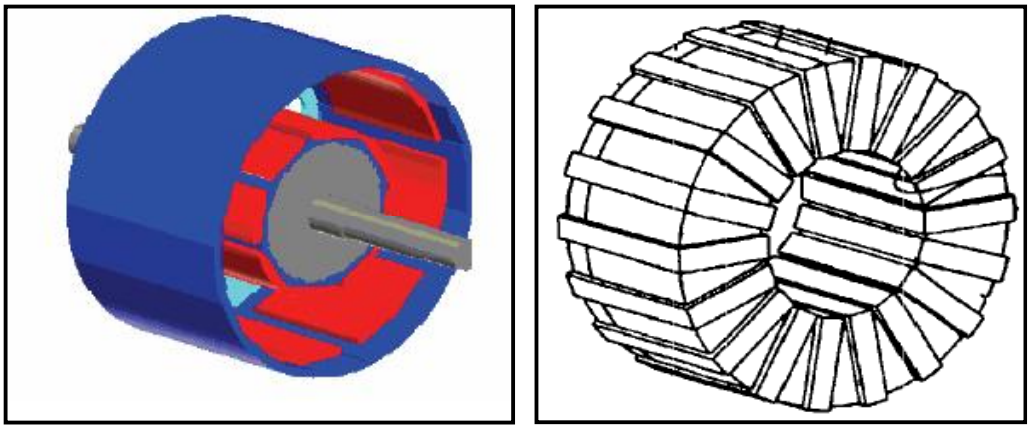

Fig. 1.17: Duel rotor PMSM with Gramme winding [25].

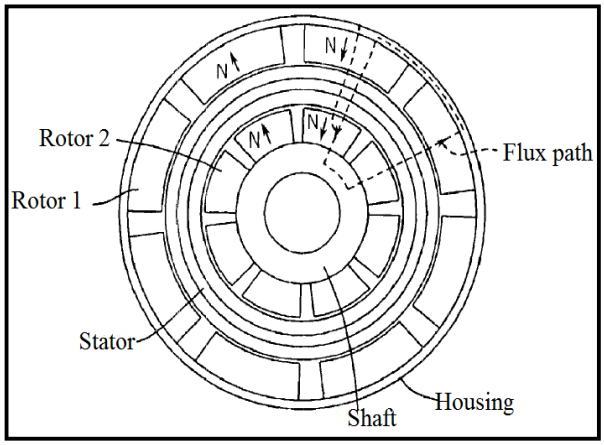

Fig. 1.18: Flux path of duel rotor PMSM.

The best way to increase machine performance as the torque or power is increasing the air-gaps number. The radial flux machine is not suitable for this kind of design, but some authors have ventured to study. The best known

example is the radial flux machine developed by [25], [3] and [26] which uses a Gramme winding to maximize the power of the machine (Fig. 1.17). The disadvantage of winding Gramme is Joule losses. Nevertheless, good results are obtained for a power range from 2.5kW to 36kW, 8 to 16 poles.

3.2. Axial Flux Machines

After the radial flux machines in the 80, the axial flux machines were primarily designed to reduce the size. Thus, the specific power and mass couples could be advantageously increased.

3.2.1.Axial Flux Machines With Single Side

The operation of this type of machine is simple because it involves stator and rotor. The flux created by a conventional distributed winding; this will interact with the flux created by the PM glued on the surface of the rotor to create electromagnetic energy and thus an electromagnetic torque (Fig. 1.24).

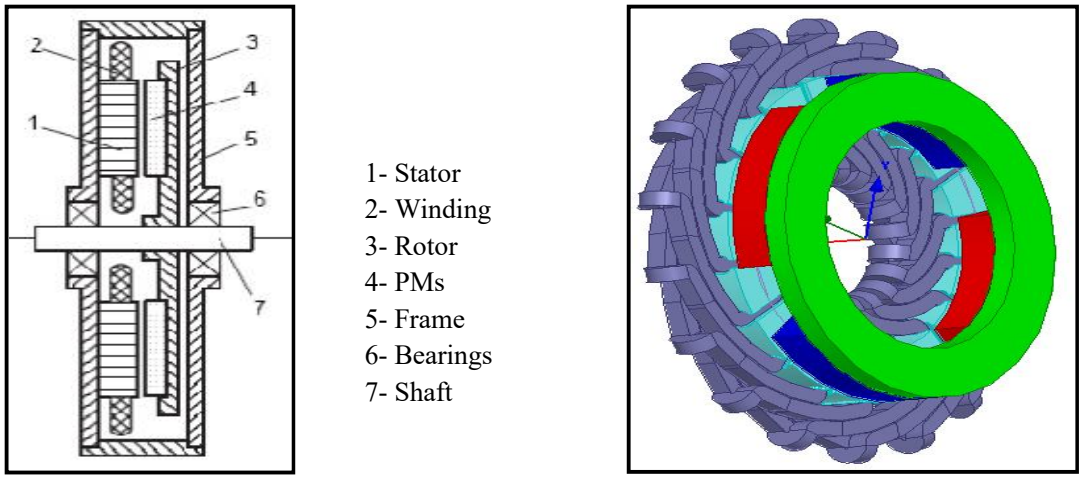

Fig. 1.19: AFPM one sided, 1 stator 1 rotor [27].

[27] Use this machine as a basis for comparison (Fig. 1.19). Numerous patents [28] [29] have been filed on that kind of axial flux machine and launch the progress for new discoid machine structures.

3.2.2.Axial Flux Machines With Internal or External Stator

Designers have focused on machines with two air gaps commonly referred to internal or external stator (Fig. 1.20 and Fig. 1.21). Unlike radial flux machines, the axial flux machine is well suited to this kind of concept. The presence of two rotors or two stators helps to balance the forces of attractions between the active parts of the machine.

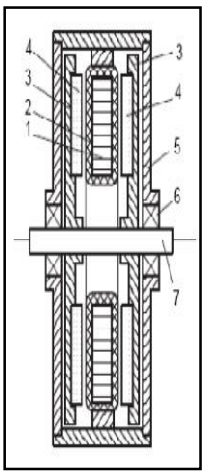

Fig. 1.20: Inner stator AFPM [30].

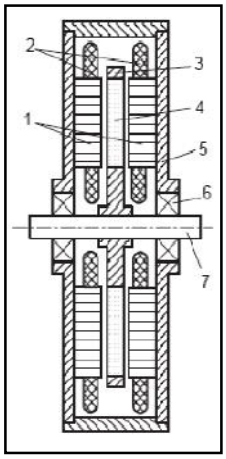

Fig. 1.21: Outer stator AFPM [30].

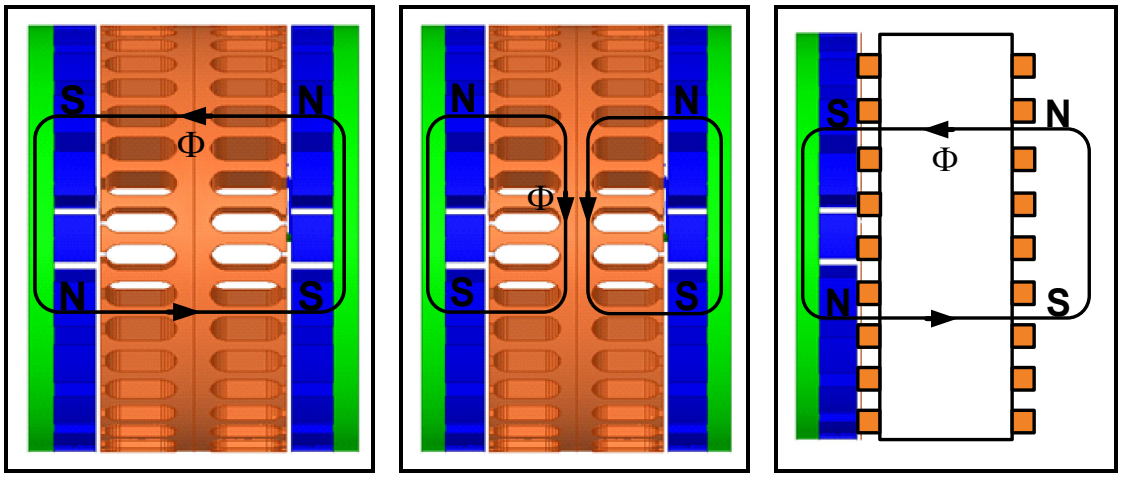

Flux path of Torus machines

Fig.1.22: Slotted NS. **Fig.1.23:** Slotted NN. **Fig.1.24:** Slotless NN.

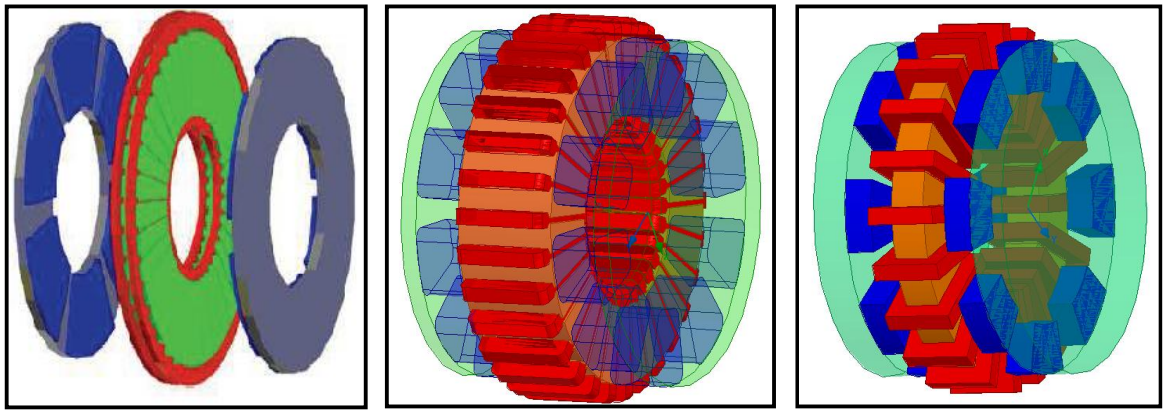

Winding of Torus machines

Fig.1.25: Slotted NS [41]. **Fig.1.26:** Slotted NN [27].**Fig.1.27:** Slotless NN [27].

These sometimes called Torus machines can be either NS type (Fig. 1.22), the magnets facing each other have different polarity, or NN-type (Fig. 1.23 and 1.24), the magnets placed face to face are of the same polarity. The Torus machine has two types of winding slotted (Fig. 1.25 and Fig. 1.26) or slottless (Fig. 1.27), the end winding is increased Joule losses. The designers of these machines, pride their efficiency and power density [27] [41].

NN Torus machines are used for slow speeds such as elevators [31] (5kW and 95 rev/min, 24 poles), hybrid vehicles [32] (30kW 4000 rev/min, 6 poles) and wind turbines [33] (1kW 490 rev/min, 12 poles). [34] [35] studied the field weakening phenomenon of Torus machine and add a DC ring coil on the stator to control the air gap flux induction.

Finally, it was shown in [36] that this type of machine has a sound level (cogging torque) less than radial flux machines.

This is why designers develop this machine for electric vehicles [37] (3kW 750 rev/min, 8 poles), [38] (72kW 3000 rev/min, 16 poles). In general, the Torus Machine includes a variety of applications ranging from variable speed [39] (880W, 2800 rev/min, 4 poles) at slow speeds [40] (14MW 195 rev/min, 80 poles).

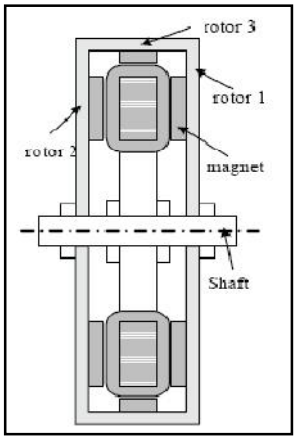

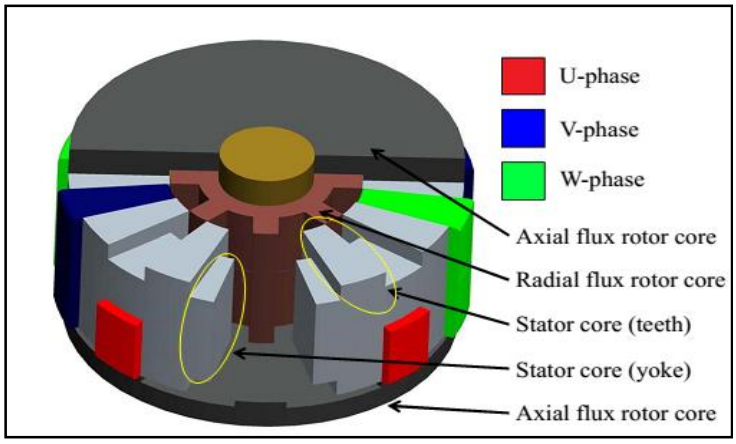

Fig. 1.28: Axial-radial flux machine [42]. **Fig. 1.29:** Axial-radial flux machine [43].

One of the latest developments of the internal stator Torus machine is adding rotors at the outer radius of the stator. This machine is called axial-radial flux machine (Fig. 1.28 and Fig. 1.29). Thus, only the internal parts of the stator winding are not involved in torque production. The use of the active parts of

the stator is optimized [42] [43]. This configuration increases the power of the machine and therefore gets very good torque and power density.

In Fig. 1.30 and Fig. 1.31 the rotor in this case is ironless. Two winding possibilities can be used: a slotted winding distributed or slotless Torus winding

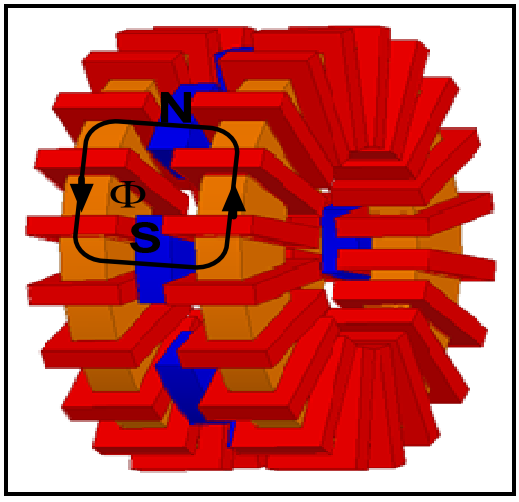

Fig. 1.30: Flux path of outer slottless stator [25].

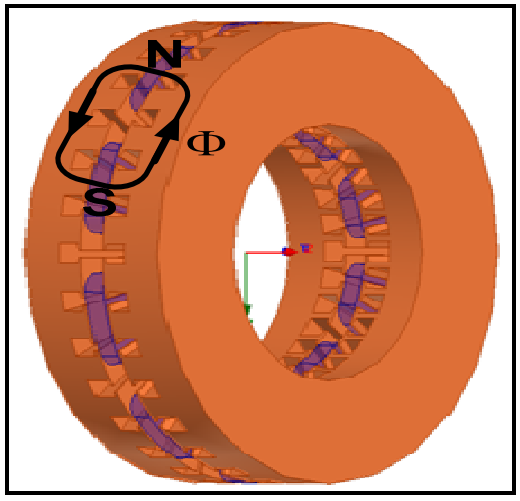

Fig. 1.31: Flux path of outer slotted stator.

In case where the machine must be incorporated into system, [44] has also studied this type of machine (55kW, 600rev/min, 6 poles) for the wheel motors [45] (1.5kW, 500rev/min, 4 phases).

3.3. Transverse Flux Machines

Many transverse flux PM machines discussed in the papers are surveyed in order to identify the possibility and potential of the machines for direct drive (Fig.1.32). The configurations, advantages and disadvantages of the TFPM machines have been discussed in a number of references [46] [47] [48] [49] [50] [51] [52] [53] [54] [55] [56] [57] [58].

The difference between TFPM machine and RFPM and AFPM machines is that the TFPM machine allows an increase of the space for the windings without decreasing the available space for the main flux. The TFPM machines has small pole pitch with compared with other machines, this feature will be done the TFPM machine in higher density than RFPM and AFPM machines [59] [60]. The copper winding of the TFPM machine is simple, and end winding is significantly smaller than other machines. Thus, the active mass of the TFPM

machine needed to produce the required torque can be smaller than other machines [61]. However, the TFPM machine has disadvantages such as a complicated construction especially stator core, a low power factor and difficulties in manufacturing [62]. The TFPM machine seems to be a suitable machine type for direct-drive applications [63].

3.3.1.Surface-Mounted TFPM Machines

Different configurations of surface-mounted TFPM machines were discussed by a number of authors. In this thesis the surface-mounted TFPM machines are mainly categorized as sided and single double -sided. Single-sided surface-mounted TFPM machines were discussed in [64] [65] [66] [67]. Double-sided surface-mounted TFPM machines were discussed in [69] [70].

Double sided surface mounted TFPM machine with double windings (Fig. 1.33a) [71]. Another double-sided, surface-mounted TFPM machine with reduced flux leakage was also discussed as shown in Fig. 1.33b [72]. It was stated that both current loading and flux density were the determining factors for force density. The current loading of the TFPM machine was higher than seven times the current loading of the RFPM machines with the same current density.

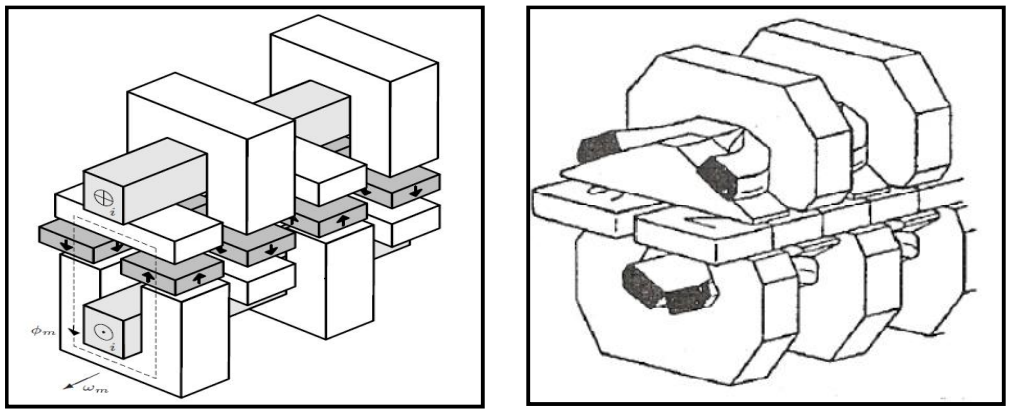

(a) [71] (b) [72]

Fig. 1.33: Double-sided surface-mounted TFPM machines.

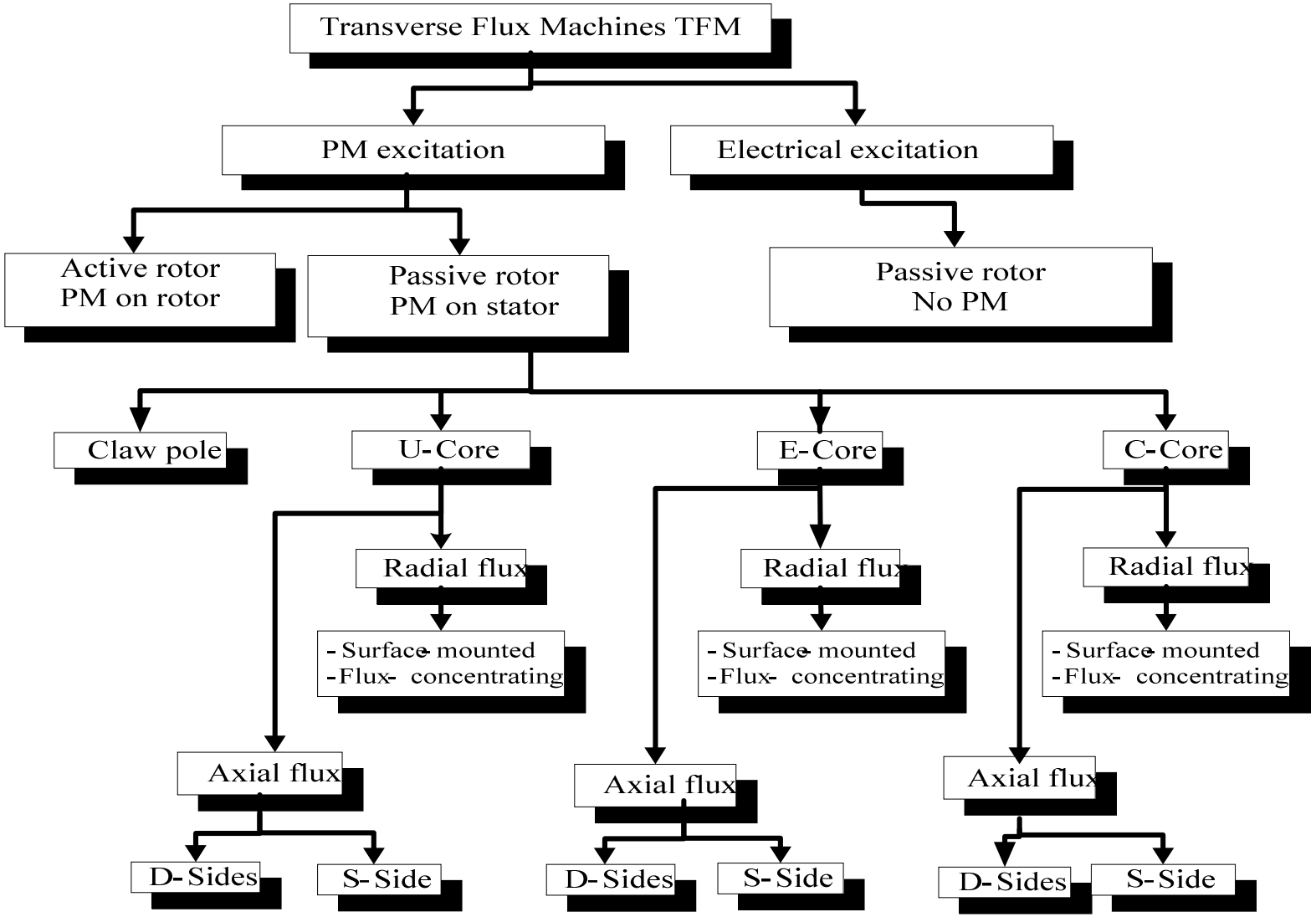

Fig. 1.32: Transverse flux permanents magnets machines classification

A double-sided TFPM machine combined with modular structure, axial flux configuration and double windings for wind turbine generators was proposed by [73]. As shown in Fig. 1.34. They showed that the ring stator winding could be easily assembled and automatically produced and the winding is exposed to open air, which improves cooling. A single-phase machine with 650 W power rating at 667 rpm was discussed [73]. The machine consists of stator and rotor cores with 18 pole PMs.

Torque ripple reduction of a double-sided axial type TFPM machine was discussed by [74].

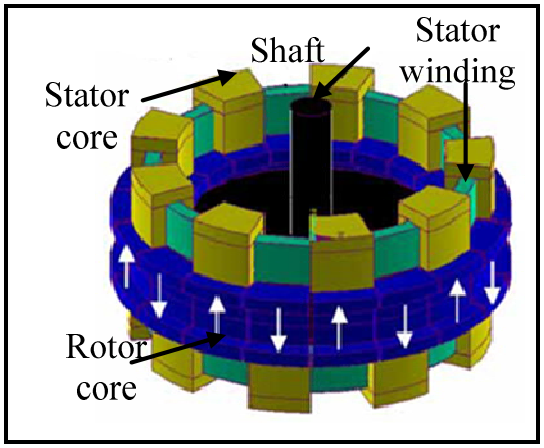

Fig. 1.34: A double-sided TFPM machine with axial air gap [73].

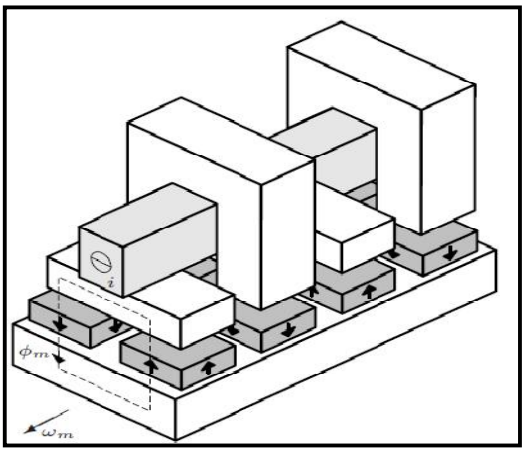

Fig. 1.35: A single sided surface mounted TFPM machine with single windings [75].

A single-sided surface-mounted TFPM machine with single winding shown in Fig. 1.35, an outer rotor type of the machine was discussed by [75] as shown in Fig. 1.36. The torque densities of a single-sided surface-mounted TFPM

machine with outer rotor were compared with the torque density of an induction machine [76] [77] [78]. The TFPM machine of which the torque rating is 69.1 Nm showed the torque density is 4.9 times higher by volume and 7 times higher by mass than the values of the induction machine.

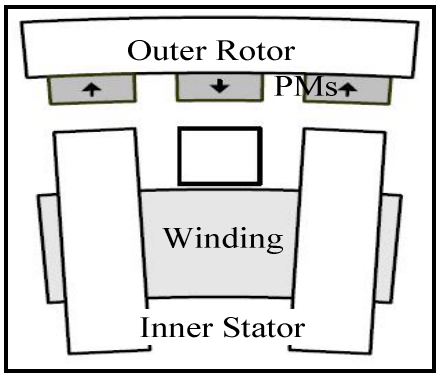

Fig. 1.36: Outer rotor type of the machine was discussed by [75].

The design, performance analysis, and experimental results of the surface-mounted transverse flux PM machine using soft magnetic composites (SMC) have been discussed in [79]. Fig. 1.37 represents the surface-mounted TFPM machine with outer rotor and SMC cores. The measured performance of the SMC TFPM machine was compared with three different motors, namely an induction motor, a radial flux PM DC motor and an SMC claw pole motor. The output power rating of the SMC TFPM motor was 690W at 1800 rpm. The SMC TFPM motor had the highest values of torque to volume ratio compared to the other motors.

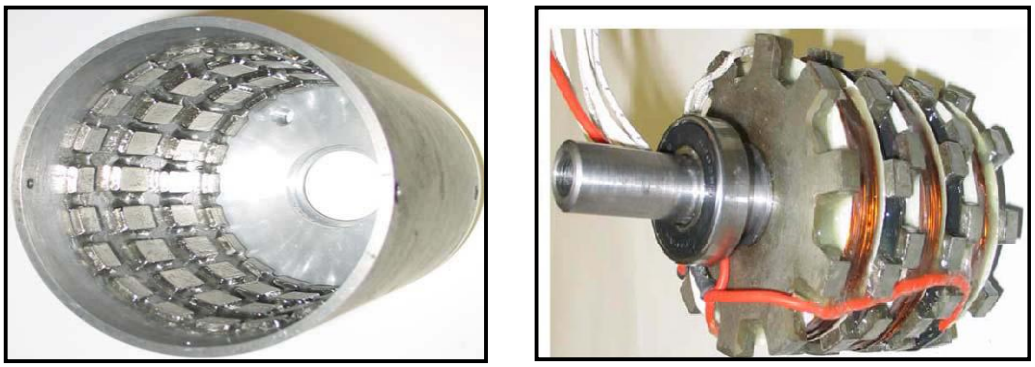

(a) (b)

Fig. 1.37: Outer rotor surface mounted TFPM machine with SMC cores (a) rotor (b) stator [79].

The torque to volume ratio of the SMC TFPM motor was almost 4.5 times higher than the torque to volume ratio of the induction motor.

The authors design a single-sided surface mounted TFPM machine with an outer rotor, the design results of the machine were compared with the results of both a double-sided flux-concentrating TFPM machine with single windings [80] and a surface-mounted TFPM machine [81]. The single-sided surface-mounted TFPM machine with an outer rotor [79] had higher torque to volume values than the other two machines. The double sided surface mounted TFPM in [81] had the highest power factor.

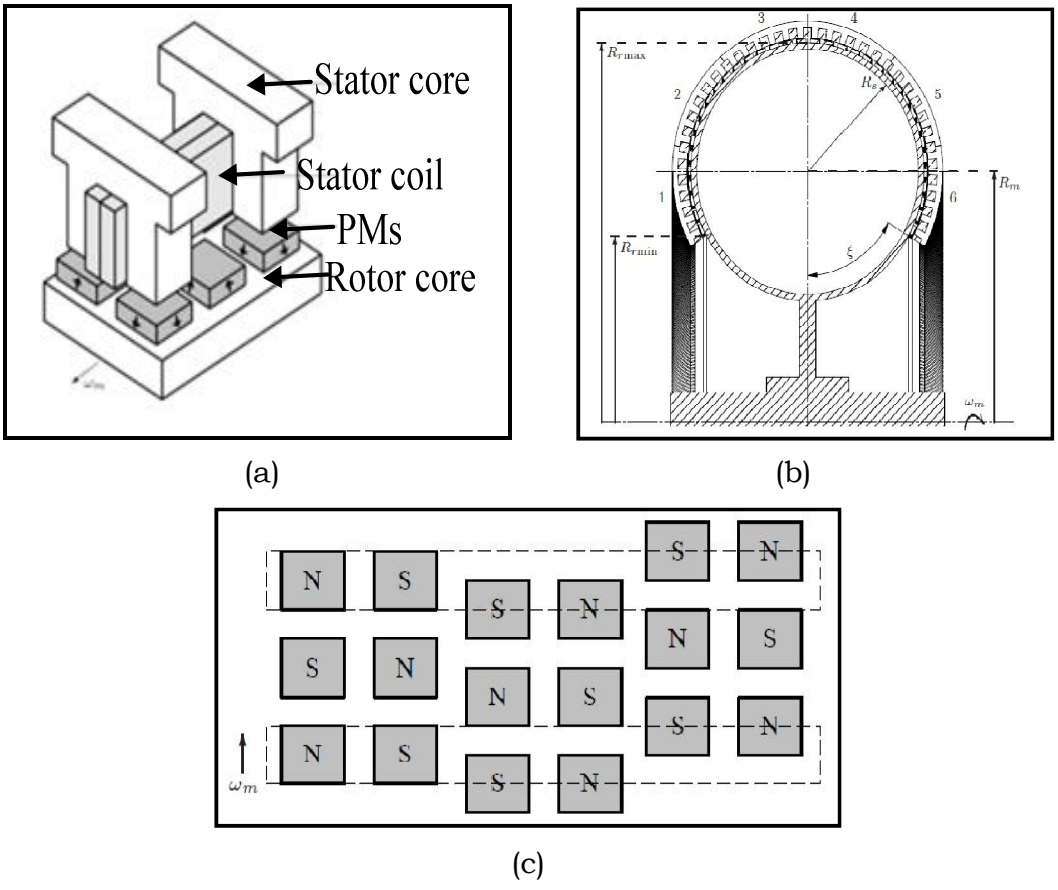

Fig. 1.38: A novel TFPM (Ω) topology for a direct-drive wind turbine, (a) Elements necessary of this machine, (b) Mechanical construction, (c) PMs Arrangements [82].

A novel single-sided surface-mounted TFPM machine with single windings for direct-drive was proposed and analyzed in [82]. The power ratings of the generators are 3, 5, 7 and 10 MW at 18.6 rpm, 13.2 rpm, 10.6 rpm and 8.3

rpm, respectively. Fig. 1.38 illustrates the novel TFPM machine that consists of a hollow rotor (Ω omega form) with the surface mounted PMs embraced by the laminated stacks with the windings placed in the slots.

New concept of a single-sided TFPM machine with single windings and stator bridges, the stator of the machine consists of laminated U-cores with stator bridges and ring-shaped windings in [83]. The rotor of the machine consists of laminated iron cores and an axially magnetized PM ring as shown in Fig. 1.39.

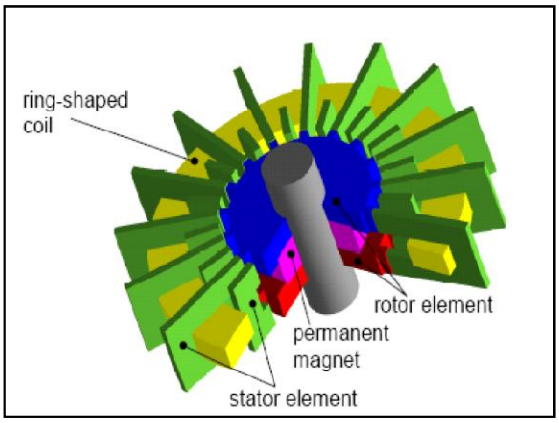

Fig. 1.39: Single-sided TFPM machine with stator bridges and axially magnetized magnets [83].

The analysis and performance of a single-sided surface mounted TFPM machine with single windings, stator bridges and an outer rotor [84]. The stator of the machine consists of U-shaped and I-shaped laminated iron cores and ring windings. The rotor consists of a back iron core with surface-mounted PMs. Fig.1.40. The power rating of the machine was 6kW at 594 rpm.

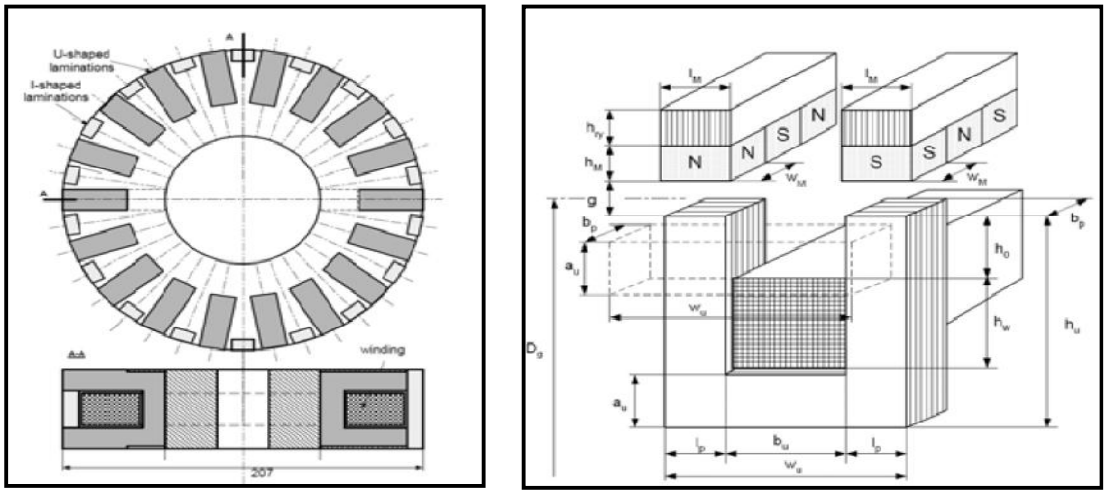

Fig.1.40: A surface mounted single sided TFPM machine with stator bridges [84].

The improved the performance of the single-sided surface-mounted TFPM machine with single windings and claw poles are doing by [85]. To build the claw pole structure of the machine soft magnetic composites (SMC) were used. In order to reduce the leakage flux of the machine, they optimized the shape of claw pole using both finite element analyses and an equivalent reluctance model. Fig. 1.41 illustrates the main flux path of a claw pole surface mounted TFPM machine. The average torque of the machine was 25.6 Nm, which corresponds to 9.3 Nm/kg at the thermally limited current.

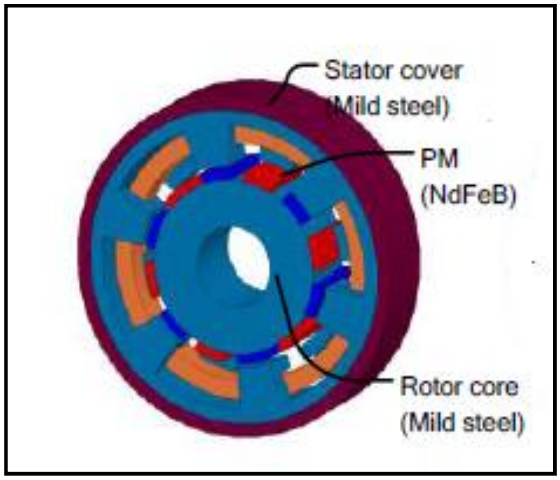

Fig. 1.41: Claw pole surface-mounted TFPM machines [85]

3.3.2. Flux-Concentrating TFPM Machines

The flux-concentrating TFPM machines have been discussed as a superior machine type regarding their specific torque and power factor. The disadvantages of their complicated construction and lower robustness were also discussed. The flux-concentrating TFPM machines are also categorized into the single-sided type and the double-sided type. Double-sided flux-concentrating TFPM machines were discussed in [86] [87] [88] [89] [90] [91] [92] [93]. The single-sided flux-concentrating TFPM machines were discussed in [94] [95] [96].

A double-sided flux-concentrating TFPM machine with double windings and U-core arrangement shown in Fig. 1.42 was proposed by [90]. Power densities of three different 75 kW machines, namely the 4-pole induction machine, the 16-pole TFPM machine with ferrite magnets, and the 16-pole TFPM machine with

rare earth magnets, were compared using the sizing and power density equations.

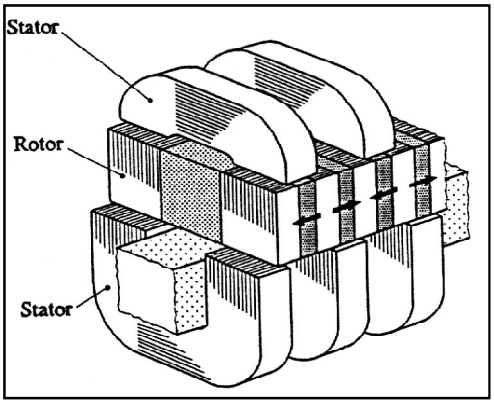

Fig. 1.42: TFPM machine with double-sided with double winding and U-core arrangement [90].

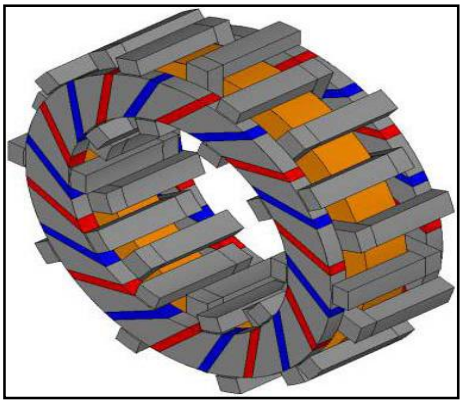

Fig. 1.43: A double-sided flux-concentrating TFPM machine with single windings [92].

In the comparison between the induction machine and the two TFPM machines, the TFPM machine with rare earth magnets had the highest power density over the whole speed range. The induction machine had the lowest power density.

A novel TFPM generator (TFPMG) with double C-hoop stator and flux-concentrated rotor is proposed [92] Fig 1.43 for low-speed applications, such as direct-drive power generation, which has larger torque capability and more poles than traditional double-side TFPMGs. In this paper the 3-D finite-element method (3-D FEM) is employed to compute the no-load magnetic field distributions.

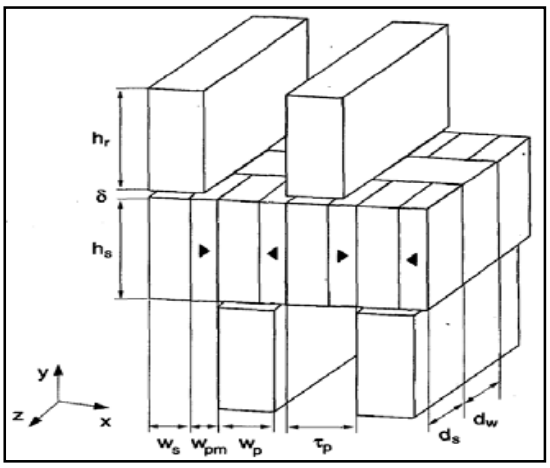

Fig. 1.44: Flux-concentrating TFPM machine with a passive rotor and single windings [91].

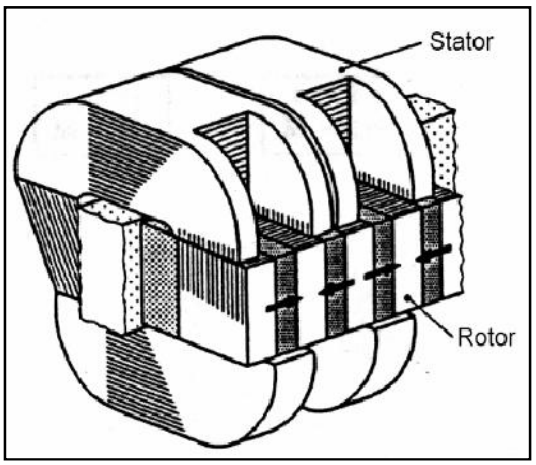

Fig. 1.45: A double-sided TFPM machine with single windings and C-core stator made of laminated steel [88].

The analysis of the design limitations of a double-sided flux concentrating TFPM machine with a passive rotor and single windings as shown in Fig. 1.44 [91], In this paper, optimum dimensions of pole pitches, PM widths, and rotor pole widths were discussed.

A double-sided flux-concentrating TFPM machine with single windings and C-core arrangement was proposed by [89], where the stator core consists of laminated steel as shown in Fig. 1.45.

The paper [88] introduced a demonstrator of a 2 MW TFPM machine rated at 308 rpm for ship propulsion. The TFPM machine was a double-sided flux-

concentrating type with single windings and C-core stator arrangement as shown in Fig. 1.48.

The cogging torque reduction and power loss reduction of a double-sided TFPM machine with single winding and a C-core stator Fig. 1.46 is discussed in [87].

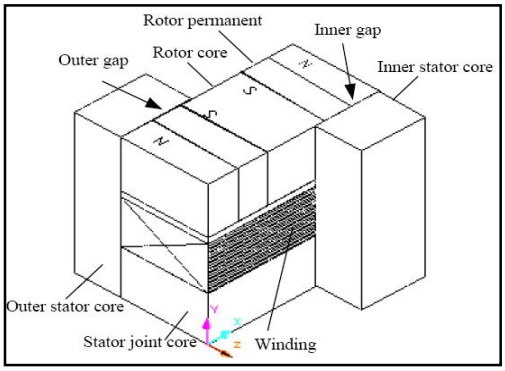

Fig. 1.46: A double-sided TFPM machine with single winding and C-core stator [87].

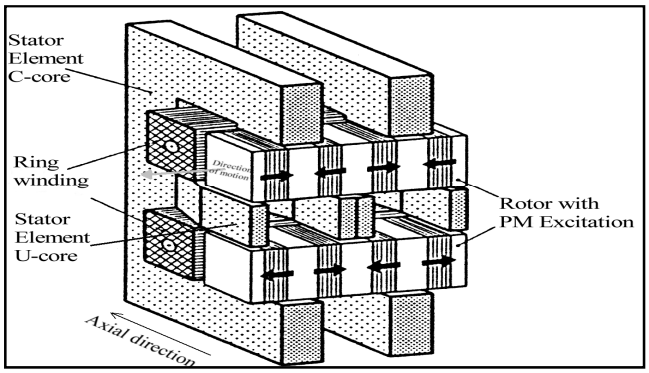

Fig. 1.47: A flux-concentrating TFPM machine with an E-core configuration [93].

Torque ripples, low power factor and complicated construction have been discussed as the disadvantages of TFPM machines compared to conventional machines. In order to reduce the torque ripples and the low power factor, the optimizations of electromagnetic dimensions and current wave forms can provide some solutions.

A flux-concentrating TFPM machine with double windings and an E-core was discussed in [93]. The stator of the TFPM machine consists of E-cores with laminated steel and two windings. The rotor consists of two sets of flux-concentrating magnets and iron cores as shown in Fig. 1.47.

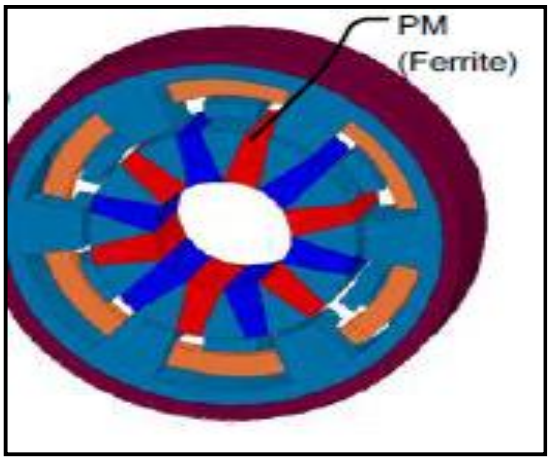

Fig. 1.48: Claw pole flux-concentrating TFPM machine [79]

[79] Has a prototype 52W claw transverse flux machine with a magnet rotor placed in flux concentration position for a servo type application. The machine (Fig.1.48) has 6 pairs of pole for a maximum speed of 3000 rpm and an outside diameter of 67 mm for a length of 55 mm. The machine provides a torque of 0.2 Nm/kg and efficiency of 0.71. Also the material cost of these machines, the price for each material is estimated.

4. Analysis and Determination of Innovative Concept

Throughout this literature search, an innovative concept of electric machine emerges. This is the surface mounted permanent magnets axial-transverse flux machine with dual gaps and winding ring on queasy U stator core. Given the objective of this thesis, the axial-transverse flux machine can meet the criteria of versatility, innovation and performance.

Versatility, because the design of axial-transverse flux machine allow for easy addition of module "rotor-stator" to increase the power.

Innovation as the axial flux machine and transverse machine are in its early development. Little studied the combination of transverse flux and axial flux surface mounted magnets can bring an interesting development in terms of performance.

Finally, because of the two air gaps allows doubling the electromagnetic torque and power. The surface mounted magnets it possible to increase the flux in the gap, reduce leakage flux and easy attachment of them in rotor.

5. Wind Turbine Concepts and Generator Systems

Wind power is one of the fastest growing renewable energy sources over the past decade Fig.1.49 and Fig.1.50. Wind energy production is increasing by approximately 30% annually. This growth accounts for both the amount and the size of new turbines installed.

The increase in size and output power of a typical wind turbine for the last 20 years is depicted in Fig. 1.51. A typical size of a recently installed turbine exceeds 2 MW. Several wind turbines above 3 MW are being tested at the time of writing and in a few years the turbines up to 5 MW should be reasonably expected on the market. At the same time, the cost of electricity produced by wind has dropped quite considerably since it re-emerged in the beginning of the 1980s. A value of up to one sixth of the initial price has been reported [98]. This trend is likely to continue in the foreseeable future as more cost effective wind turbines are being developed and installed worldwide.

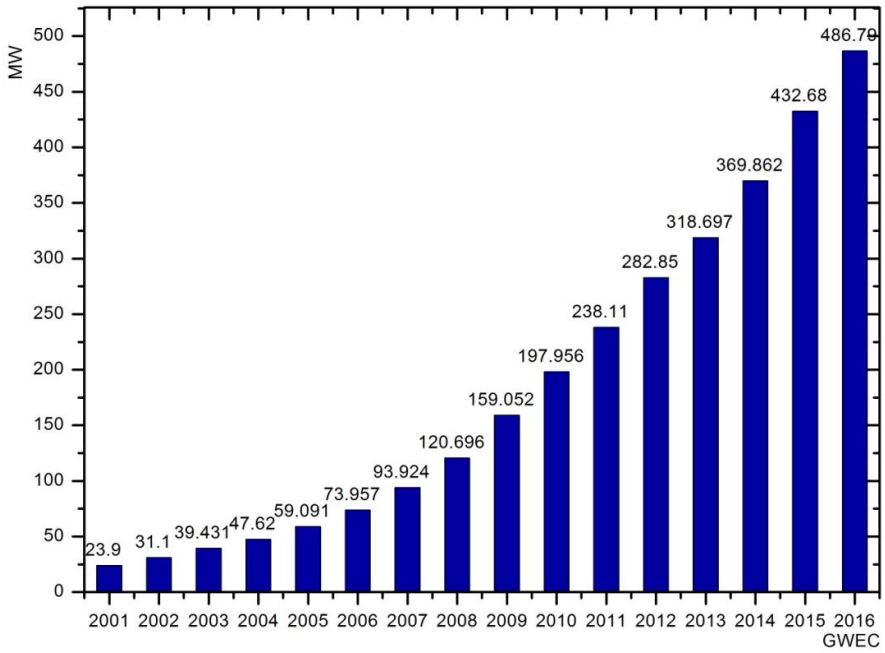

Fig. 1.49: World cumulative wind power capacity.

In order to maximize the energy harnessed, to minimize the cost, to improve the power quality and to ensure safety together with the growth of the size, various wind turbine concepts have been developed during last three decades [99]. Until the late 1990's, most wind turbine manufacturers built fixed-speed

stall-controlled turbines with a squirrel cage induction generator system and a three-stage gearbox. Due to the high thrust load in the rotor blades of the fixed-speed turbines and other reasons, most wind turbines with a power rating over 1.5 MW have changed to the variable speed pitch-controlled concept since the late 1990's. In addition, direct-drive wind turbines have been built to increase energy yield, reduce gearbox failures, lower maintenance problems and to obtain better power quality to the grid since 1991.

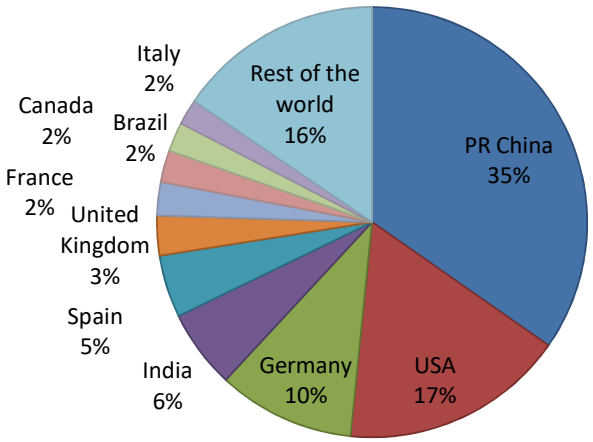

Country	MW	%Share
PR China	168.732	34.7
USA	82.184	16.9
Germany	50.018	10.3
India	28.700	5.9
Spain	23.074	4.7
U. Kingdom	14.543	3.0
France	12.066	2.5
Canada	11.900	2.4
Brazil	10.740	2.2
Italy	9.257	1.9
Rest of the world	75.576	15.5
Total TOP 10	411.214	84
World Total	486.790	100

Fig. 1.50: Top 10 cumulative capacities 2016 (GWEC).

A hybrid system, namely the Multibrid system, has been built and discussed as an interesting alternative for wind turbines. The Multibrid system is equipped with a medium speed permanent magnet synchronous generator and a single-stage gearbox. An electrically excited synchronous generator system with mechanical and hydraulic gearboxes has also appeared on the market.

5.1 Technology of Wind Turbines

Wind turbines can be operated either at fixed or variable speed. Fixed-speed wind turbines use an older and relatively simple technology with a constant-speed mechanical input. They are often intended only for a certain wind speed at which the maximum efficiency can be achieved. The rotational speed of an electrical generator can be changed in a stepwise manner by changing the pole number. For example, the synchronous speed can be changed from 1500 rpm

to 1000 rpm by switching the pole number from four to six. Because of the fluctuations of generated power, fixed-speed turbines have a less positive impact on power systems, as compared to the variable speed turbines. Turbines of this type have a possibility to control the amount and the frequency of produced electricity, although it requires a more complicated electrical system. Variable-speed wind turbines can also be designed for a broader wind speed range.

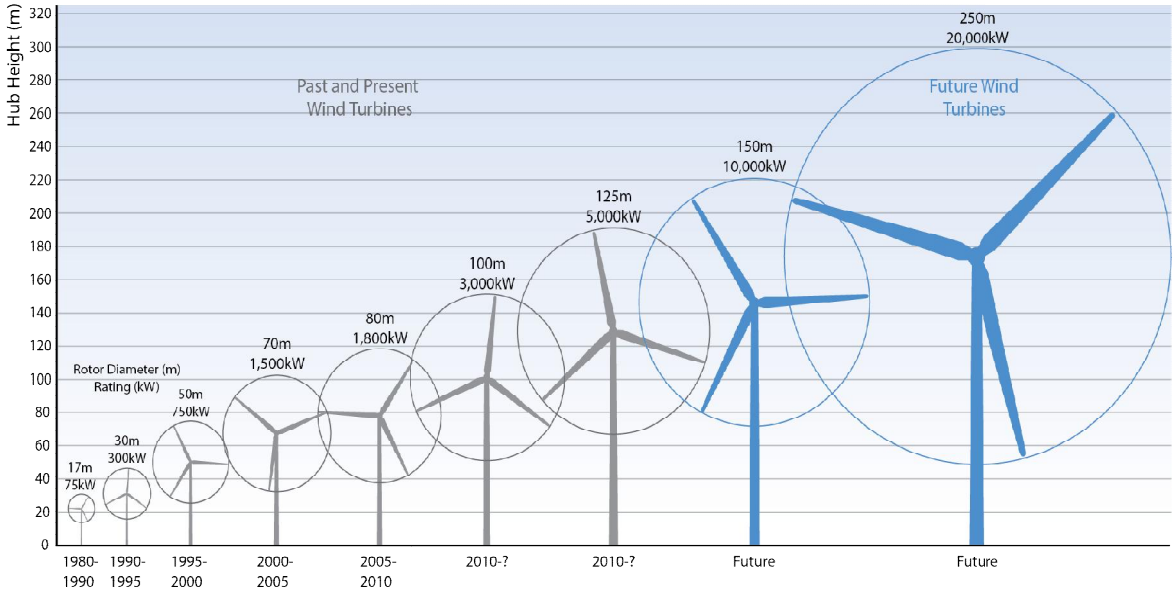

Fig.1.51: Growth in size of typical commercial wind turbines.

Generator systems used in variable speed pitch-controlled wind turbine concepts can be classified as:

- Doubly-fed induction generator system with a three-stage gearbox.
- Squirrel cage induction generator system with a three-stage gearbox.
- Permanent magnet synchronous generator system with a three-stage gearbox.
- Direct-drive electrically excited synchronous generator system.
- Direct-drive permanent magnet synchronous generator system.

5.1.1 Wind Turbines with a Gearbox

The basic wind turbine configuration with a fixed-speed mechanical input is illustrated in Fig. 1.52. The shaft of the electric generator (typically, a squirrel

cage induction generator) is connected to the turbine shaft through a step-up gearbox.

The gearbox is introduced to adjust a low-speed turbine shaft (in the range of tens of rpm) to the higher rotational speed of a conventional generator (up to several thousands rpm) with the gear ratio of approximately 100. To compensate the reactive power consumed by the induction generator, a capacitor bank is integrated into the system. The soft-starter is used to assure a softer connection to the grid [100].

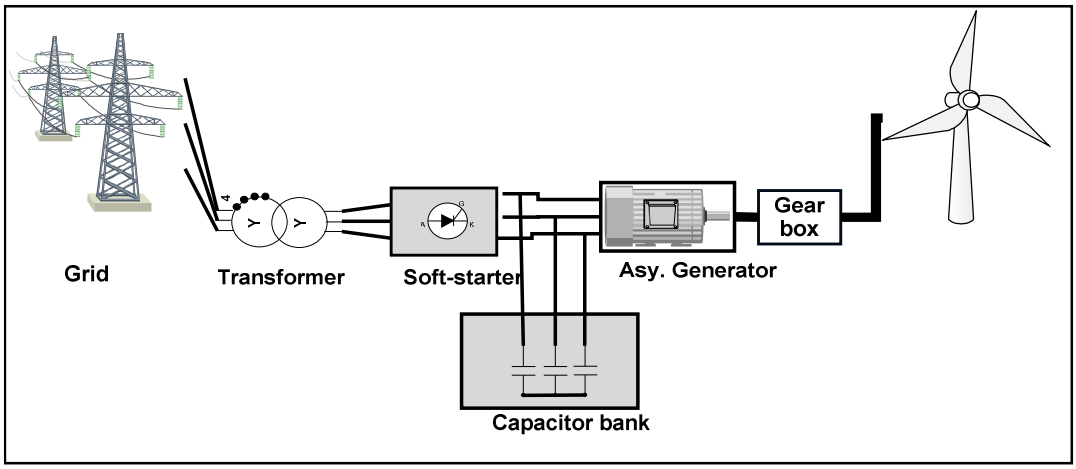

Fig.1.52: Squirrel cage induction generator system with a three-stage gearbox.

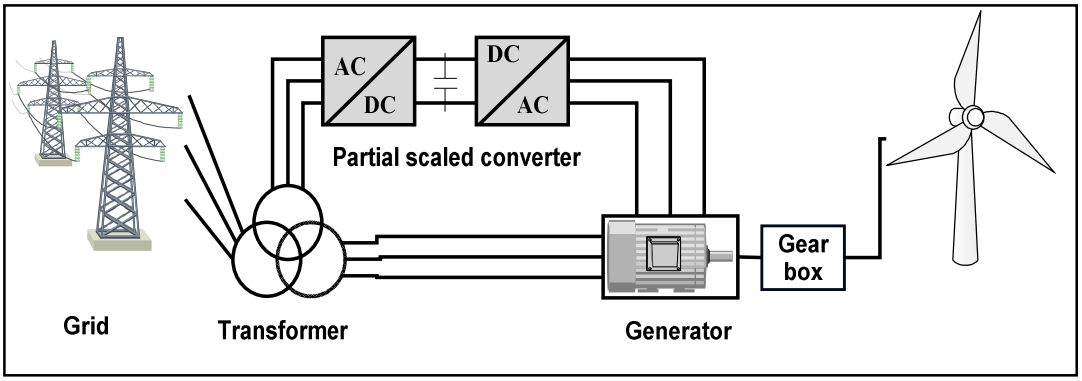

Fig.1.53: Doubly-fed induction generator system with a three stage gearbox.

The configuration depicted in Fig. 1.53 uses a doubly-fed induction generator concept, where the stator winding of a wound rotor induction generator is directly connected to the grid whereas the rotor winding is connected through a frequency converter. The power converter, rated only for a part of the generator nominal output power (about 30 %), is used to regulate the production of reactive power and to smoothen the grid connection. Depending

on the converter nominal power, it can vary within the interval between 40% below and 30% above the synchronous speed [101].

In the topology in Fig. 1.54, the turbine shaft and generator shaft are coupled to each other through a step-up gearbox [102]. The gear ratio between the turbine and generator speed is only about 10, which results in a generator that has a medium torque and rotational speed.

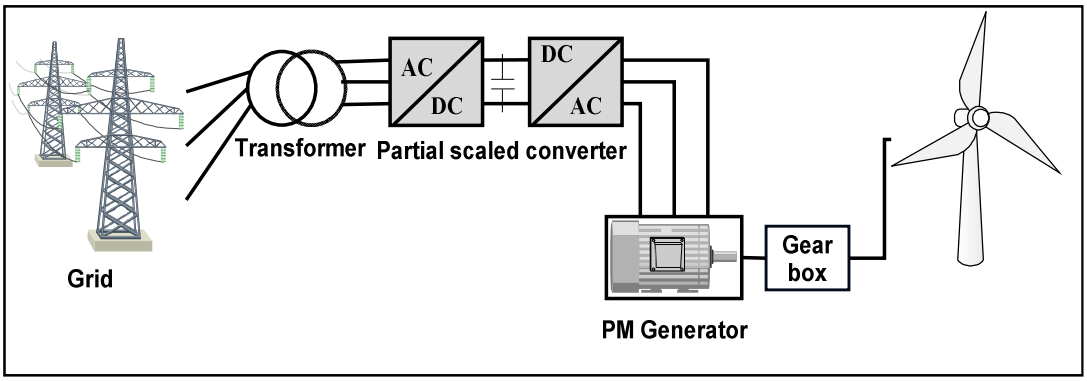

Fig.1.54: PM synchronous generator system with a three-stage gearbox.

5.1.2 Wind Turbines without a Gearbox

Gearless Wind Turbines With further development of wind turbine technology and increased wind power penetration level in power systems, the issues of availability and reliability of generating units become of great importance. This particularly applies for stand-alone and offshore applications due to their often hard to reach locations. The overall reliability of a wind turbine is somewhat reduced by gearbox used in wind energy systems. In addition, the gearbox is subject to mechanical wear, vibrations, requires lubrication and more frequent maintenance at considerable cost [103].

As a result, the gearless wind energy system has drawn the attention of wind turbine manufacturers. A schematic of such system is presented in Fig. 1.55.

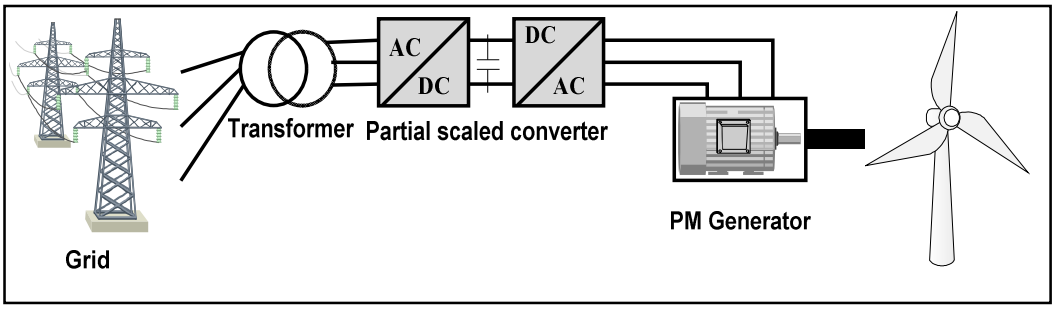

Fig.1.55: Direct drive PM synchronous generator system.

5.2 Common Wind Turbine Configurations

For the connection of a generator to the network, a converter scaled for the full output power is required. This introduces extra cost and additional losses. Yet the efficiency of such a system can be somewhat higher than the efficiency of the system containing a gearbox and an induction generator directly connected to the grid [104].

On the other hand, a full scaled converter offers an opportunity of a variable speed control over a large speed range. This allows a better utilization of the available wind power and therefore has a potentially higher energy yield. The interest in gearless energy systems is likely to continue growing in the near future as larger power converters become available at decreasing cost.

A direct driven low speed generator with a large number of poles and larger than conventional generator outer diameter is required in the gearless wind system. Electrically excited direct-driven synchronous and induction generators are utilized by a number of wind turbine manufacturers.

In the last few decades, a reduced magnet price has made synchronous generators with PM excitation an attractive alternative. In comparison to the electrical excitation, the permanent magnet excitation favors a reduced active weight, decreased copper losses, yet the energy yield is somewhat higher [105].

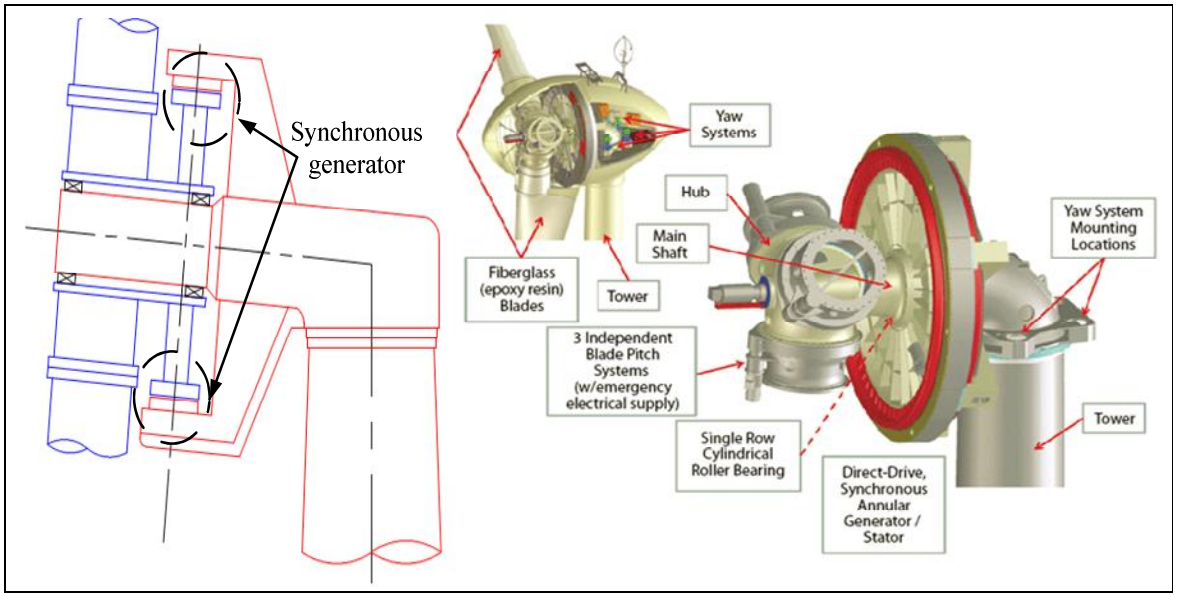

Fig. 1.56: Direct drive synchronous generator compositions.

A number of studies have been conducted investigating different topologies of PMSG suited for direct driven low speed wind generators [104, 106]. A possibility of utilizing a transverse flux permanent magnet topology in the gearless wind energy system was discussed by [107] as early as in 1990. An attractive feature of the TFPM is that with an increasing number of poles, the machine rating can be increased and as a result a higher value of specific torque density can be achieved [108].

The TFPM generator has a magnetic flux path perpendicular to the direction of the rotor rotation. Compared with the conventional PM generators, the TFPM generator has been discussed as a generator with high force density. Thus, the TFPM generators have more potential to reduce both the volume and the mass than the longitudinal flux RFPM generators. However, in [55] concluded that RFPM generators are better than the TFPM generator with toothed rotor based on the mass and the cost of active part, if the air gap length is larger than 1.5 mm?. Therefore, it is needed to find TFPM generators which are lighter and cheaper than RFPM generators for direct drive wind turbines!.

A novel transverse flux permanent magnet topology for wind power generation is discussed in this work. Further description of this topology, its features and design possibilities are presented in detail in next Chapters.

6. Conclusion

The literature searches on machines topologies that allow us meet their specifications and characteristics.

Using a classification depending on the flux direction, the winding and the number of gaps, two structures are likely to provide good electromagnetic performance (mass torque, specific power, performance). This is the surface mounted axial flux machine double gap and Torus winding, and the surface mounted transverse flux machine double gap and ring winding type.

- Radial machines are the subject of numerous prototypes. Among the most interesting structures for the application, buried magnet machines are currently the best challengers in terms of mass power, power factor.

The following advantages of the radial flux (RF) machines can be listed.

- Structural stability

- Easy production (compared to the slotted axial flux machine and transverse flux machine)

Because of these advantages, the RF machines have mostly been used in the industry.

➢ Axial flux machines are the future machines, because of their high specific power and low inertia (especially for machines with a rotor and two stators). These machines nevertheless meet mechanical problems of maintaining the axial air gaps and choices of isotropic materials.

Many technological possibilities for permanent magnets synchronous machines have been exposed.

The first studies of this type of machine show that gains in weight and overall dimensions facilitate its integration in systems where space is limited. The axial flux machine is very suitable for embedded systems and direct drive.

The following advantages of the axial flux permanent magnet (AFPM) machines compared to the radial flux permanent magnet (RFPM) machines have been discussed in the references.

- Simple winding (in a slotless machine).
- Low cogging torque and noise (in a slotless machine).
- Short axial length.
- Higher torque/volume ratio.
- The machine can operate as a low speed generator.

➢ The study of transverses flux machines is described. It is explained why TFM achieve higher force densities than RFM. Different magnet circuit layouts of stator are reviewed and several possible rotor designs using permanents magnets are discussed. A description of the working principals and their characteristics are investigated. The major disadvantages of TFM are the large armature winding results in a low power factor and largely inductance influenced by the design of permanent magnet.

The advantages of transverse flux machines (TFM) compared than another machines can be summarized as.

- A better utilization of active materials than in standard (longitudinal flux) PM brushless motors for the same cooling system, i.e., higher torque density or higher power density.
- Simple windings (no end connection).
- Unity winding factor.
- A three phase TFM can be fed from a standard three phase inverter for PM brushless motors using a standard encoder.
- The machine can operate as a low speed generator.

Bibliography -1-

[1] Mebarki et al, United States Patent, Application Publication, Pub. No. US0241460 A1, Oct. 2011.

[2] Qu, R., Aydin, M., Lipo, T.A., "Performance Comparison of Dual-Rotor Radial-Flux and Axial-Flux Permanent-Magnet BLDC Machines". In Proceedings of IEEE Electric Machines and Drives Conference, IEMDC'03, Madison, United States, 1-4 June 2003, Vol. 3, pp. 1948-1954.

[3] BENDIB M., M. Hachemi, K. Belhouchat, "Axial Flux Permanent Magnet Torus Moto Design Using Sizing Equation and FEA", CEE, Batna, 2016.

[4] A. P. Ferreira1, A. M. Silva, A. F. Costa, "Prototype of an Axial Flux Permanent Magnet Generator for Wind Energy Systems Applications", School of Technology and Management, Polytechnic Institute of Bragança, Portugal,2005.

[5] F.Marignetti, G.Tomassi, P.Cancelliere, V.Delli Colli, R. Di Stefano, M.Scarano, "Electromagnetic and Mechanical design of a Fractional-slot-windings Axial-flux PM synchronous machine with Soft Magnetic Compound Stator", IAS'06, 2006.

[6] D. Oleksandr, "Study on Permanent Magnet Transverse Flux Machine", Doctor of Philosophy in the Department of Electrical & Computer Engineering, Louisiana State University, USA, May 2012.

[7] Kremers, M.F.J., "Analytical Design of a Transverse Flux Machine", Doctorate Thesis, Technische Universiteit, Eindhoven, Sept. 2016.

[8] K. Sitapati, R. Krishnan, "Performance Comparisons of Radial and Axial Field, Permanent Magnet, Brushless Machines", IEEE Trans. on Ind. App., 2001.

[9] C.C. Mi, "Analytical Design of Permanent-Magnet Traction-Drive Motors", IEEE Tran. on Mag., 2006.

[10] A.M. El-Refaie, T.M. Jahns, "Comparison of Synchronous PM Machine Types for Wide Constant-Power Speed Range Operation", IAS'05, 2005.

[11] M.A.Jabbar, A.M. Khambadkone, L. Qinghua "Design and Analysis of Exterior and Interior Type High-Speed Permanent Magnet Motors", Proc. Aust. University Power Electronics Conference, pp 484-489, 2001.

[12] M.Aydin, S.Huang, T.A Lipo, "Torque Quality and Comparison of Internal and External Rotor Axial Flux Surface-Magnet Disc Machines", IEEE Trans. on Ind. Elec., Vol.53, n°3, Juin, 2006.

[13] Han-Wook Cho, Seok-Myeong Jang, Sang-Kyu Choi, "A Design Approach to Reduce Rotor Losses in High-Speed Permanent Magnet Machine for Turbo-Compressor", IEEE Trans. on Mag., 2006.

[14] W.Wu, V.S.Ramsden, T.Crawford, G.Hill, "A Low-Speed, High-Torque, Direct-Drive Permanent Magnet Generator for Wind Turbines", IEEE Industry Applications Conference, 2000.

[15] L.Vido, Y.Amara, E.Hoang, M.Gabsi, F.Chabot, M.Lecrivain, "Design and Comparison of Concentrated Windings and Distributed Windings Interior PM Machines for a Hybrid Vehicle Application", IEEE Transactions on Magnetics, 2004.

[16] A.M. El-Refaie, T.M. Jahns, D.W. Novotny, "Analysis of Surface Permanent Magnet Machines with Fractional-Slot Concentrated Windings", IEEE Trans. on Ene. Conv., 2006.

[17] E.C.Lovelace, T.M. Jahns, T.A. Keim, J.H. Lang, "Mechanical Design Considerations for Conventionally Laminated, High-Speed, Interior PM Synchronous Machine Rotors", IEEE Transactions on Industry Applications, 2004.

[18] Damir Zarko, Drago Ban, Thomas A. Lipo, "Design Optimization of Interior Permanent Magnet (IPM) Motors With Maximized Torque Output in the Entire Speed Range", EPE'05, 2005.

[19] S-O.Kwon, S-Il.Kim, P.Zhang, J.-P.Hong, "Performance comparison of IPMSM with distributed and concentrated windings", Industry Applications Conference, 2006.

[20] Y.Li, H.Qian-sheng, "Design and Simulation of Interior Permanent Magnet Brushless DC Motor", Proceedings of the 8th International Conference Electrical Machines and Systems, 2005.

[21] N.Bianchi, S.Bolognani, M.Dai Pre, G.Grezzani "Design Considerations for Fractional-Slot Winding Configurations of Synchronous Machines", IEEE Trans. on Ind. App., Vol.42, N°4, Jui. 2006.

[22] D. Iles-Klumpner, M. Risticevic, I. Boldea, "Advanced Optimization Design Techniques for Automotive Interior Permanent Magnet Synchronous Machines", IEMDC'05,2005.

[23] H.Murakami, Y.Honda, S.Morimoto, Y.Takeda, "A Study of Rotor Configuration for IPMSM with concentrated Winding Considering the Iron Loss", Electrical Engineering in Japan, Vol. 139, No. 4, 2002.

[24] Liang-Yi Hsu, Mi-Ching Tsai, Chien-Chin Huang, "Efficiency Optimization of Brushless Permanent Magnet Motors Using Penalty Genetic Algorithms", IEMDC'03, 2003.

[25] R. Qu, T. A. Lipo, "Sizing Equations and Power Density Evaluation of Dual-Rotor, Radial-Flux, Toroidally Wound, Permanent-Magnet Machines", 2004.

[26] C-E. Neagoe, "Etude de nouvelles structures de machines électriques", Thèse de Doctorat de l'Institut National Polytechnique de Grenoble, France, 1996.

[27] M.Aydin, S.Huang, T.A Lipo, "Axial Flux Permanent Magnet Disc Machines: A Review", EPE-PEMC' 04, 2004.

[28] A.Yoshinari, N.Shin, K. Atsushi," Rotating Electrical Machine", Japon Patent, Patent number: 2008199811; 2008.

[29] A.Parviainen, A.Piispanen, "Axial Flux Induction Electrical Machine", World Wilde Patent, Patent Number 3048723; 2008.

[30] J.F.GIERAS, R.WANG et M.J. KAMPER, "Axial Flux Permanent Magnet Brushless Machines ", Dordrecht, The Netherlands : Kluwer, 2006.

[31] R.L.Ficheux, F.Caricchi, F.Crescimbini, O.Honorati, "Axial-Flux Permanent-Magnet Motor for Direct-Drive Elevator Systems without Machine Room", IEEE Transactions on Industry Applications, 2001.

[32] M. Cirani, "Analysis of an Innovative Design of an Axial Flux Torus Machine", Licentiate thesis, Juin 2002, Stockholm, Sweden.

[33] Y.Chen, P.Pillay, "Axial-flux PM wind generator with a soft magnetic composite core", 4th IAS Annual Meeting Industry Applications Conference 2005, Oct. 2–6 2005, Vol. 1, pp 231-237.

[34] M. Aydin, S. Huang and T. A. Lipo, "A new axial flux surface mounted permanent magnet machine capable of field control" IEEE Industry Applications Society Annual Meeting, 2002, pp. 1250-1257.

[35] M. Aydin, S. Huang and T. A. Lipo, "Performance Evaluation of an Axial Flux Consequent Pole PM Motor Using Finite Element Analysis", IEEE International Conference on Electrical Machines and Drives, Madison, 2003.

[36] S. Huang, M. Aydin and T. A. Lipo, "Low noise and smooth torque permanent magnet propulsion motors: Comparison of non-slotted and slotted radial and axial flux topologies", IEEE International Aegean Electrical Machine and Power Electronic Conference, Kusadasi- Turkey, 2001, pp. 1-8.

[37] J.Braid, A.Van Zyl, C.Landy, "Design, Analysis and Development of Multistage Axial-Flux Permanent Magnet Synchronous Machine", Africon'02, 2002.

[38] F.Caricchi, F.Crescimbini, O.Honorati, "Low-Cost Compact Permanent Magnet Machine for Adjustable-Speed Pump Application", IEEE Transactions on Industry Applications, Vol.34, n°1, Janvier/Février, 1998.

[39] F.Caricchi, F.Crescimbini, O.Honorati, G.Lo Bianco, E.Santini, "Performance of Coreless-Winding Axial-Flux Permanent-Magnet Generator with Power Output at 400 Hz, 3000 r/min", IEEE Trans. on Ind. App., Vol.34, n°6, Nov., 1998.

[40] F.Caricchi, F.Crescimbini, O.Honorati, A.Di Napoli, E.Santini, "Compact Wheel Direct Drive for EVs", IEEE Industry Applications Magazine, Nov., 1996.

[41] S.Huang, M.Aydin, T.A. Lipo "TORUS Concept Machines: Pre-Prototyping Design Assessment for Two Major Topologies", IAS'01, 2001.

[42] J.S.Hsu et al. "Permanent magnet energy conversion machine with magnet mounting arrangement", United States Patent, Patent Number: 5,952,756; 1999.

[43] D. Fukai and S. Shimomura, "Integrated Radial and Dual Axial-flux Variable-reluctance Vernier Machine", IEEE, 2014.

[44] A. Parviainen, J. Pyrhönen, M. Niemelä, "Axial Flux Interior Permanent Magnet Synchronous Motor with Sinusoidally Shaped Magnets", ISEF'01, 2001.

[45] Y-P.Yang, C-P. Lo, "Current distribution control of dual directly driven wheel motors for electric vehicles", Control Engineering Practice, 2008, pp. 1285-1292.

[46] J. Doering, G. Steinborn, and W. Hofmann,Torque, "Power, Losses, and Heat Calculation of a Transverse Flux Reluctance Machine With Soft Magnetic Composite Materials and Disk-Shaped Rotor", IEEE Trans. on Ind. App., Vol. 51, No. 2, pp.1494-1504, March/April 2015.

[47] Q. Wang, B. Zhao, J. Zhang, Y. Li, J. Zou, and H. Zhao, "Inductances and Phase Coupling Analysis of Tubular Permanent Magnet Machines With Transverse Flux Configuration", IEEE Trans. On Plas. Sci., January 2015.

[48] H. Ahn, G. Jang, J. Chang, S. Chung, and D. Kang, "Reduction of the Torque Ripple and Magnetic Force of a Rotatory Two-Phase Transverse Flux Machine Using Herringbone Teeth", IEEE Trans. on Mag., Vol. 44, No. 11, pp. 4066-4069, Nov. 2008.

[49] P. Zheng, C. Tong, G. Chen, R. Liu, Y. Sui, W. Shi, and S. Cheng, "Research on the Magnetic Characteristic of a Novel Transverse-Flux PM Linear Machine Used for Free-Piston Energy Converter", IEEE Trans. on Mag., Vol. 47, No. 5, pp.1082-1085, May 2011.

[50] G. Yang, D. Cheng, H. Zhang, and B. Kou, "Bidirectional Cross-Linking Transverse Flux Permanent Magnet Synchronous Motor", IEEE Trans. on Mag., Vol. 49, No. 3, pp.1242-1248, Mar. 2013.

[51] H. Weh, "Transverse-flux machines in drive and generator application", in Proceedings of the IEEE Symposium on Electric Power Eng. (Stockholm Power Tech), Strockholm, Sweden, 1995, Vol. Invited speaker' session, pp. 75-80.

[52] M.R. Harris and B.C. Mecrow, "Variable reluctance permanent magnet motors for high specific output", in Proc. 1993 IEE Conf. Elec. Mach. and Drives, pp. 437-442.

[53] A.J. Mitcham, "Transverse flux motors for electric propulsion of ships", in Proc. 1997 IEE Colloquium on New Topologies for PM Machines, pp. 3/1-3/6.

[54] S. Huang, J. Luo and T.A. Lipo, "Analysis and evaluation of the transverse flux circumferential current machine", in Proc. 1997 IEEE Conf. Ind. Appl. Soc., Vol. 1, pp. 378-384.

[55] M.R. Dubois, H. Polinder and J.A. Ferreira, "Comparison of generator topologies for direct-drive wind turbines", in Proc. 2000 Nordic Countries Pow. and Indust. Elec., pp. 22-26.

[56] P. Dickinson, A.G. Jack and B.C. Mecrow, "Improved Permanent Magnet Machines with Claw Pole Armatures", in Proc. 2002 Int. Conf. on Elec. Mach., paper 245.

[57] J.F. Gieras, "Performance Characteristics of a Permanent Magnet Transverse Flux Generator", in Proc. 2005 IEEE Conf. Elec. Mach. and Drives, pp. 1293-1299.

[58] Y.G. Guo, J.G. Zhu, P.A. Watterson and W. Wu, "Development of a PM transverse flux motor with soft magnetic composite core", IEEE Transactions on Energy Conversion, Vol. 21, No. 2, pp. 426-434, June 2006.

[59] L. H. Hansen, L. Helle, et al. "Conceptual Survey of Generators and Power Electronics for Wind Turbines", Riso-R-1205(EN), 2001.

[60] T. Husain; I. Hasan; Y. Sozer; I. Husain and E. MuljadiA. “Comprehensive review of permanent magnet transverse flux machines for direct drive applications”. IEEE Conferences Pages: 1255 – 1262. 2017.

[61] O. Dobzhanskyi; R. Gouws; E. Amiri. “Comparison analysis of AC PM transverse-flux machines of different designs in terms of power density and cost”. 2017 IEEE 58th International Scientific Conference on Power and Electrical Engineering of Riga Technical University (RTUCON). 2017.

[62] Oleksandr Dobzhanskyi; Rupert Gouws; Ebrahim Amiri. “Analysis of PM Transverse-Flux Outer Rotor Machines With Different Configuration”. IEEE Trans. on Ind. App.. Vol. 53, Issue: 5 PP: 4260 – 4268. 2017.

[63] Z. Wan; A. Ahmed; I. Husain; E. Muljadi. “A novel transverse flux machine for vehicle traction aplications”. IEEE Power & Energy Society General Meeting PP: 1–5. 2015.

[64] K. Y. Lu; E. Ritchie; P. O. Rasmussen; P. Sandholdt. “A simple method to estimate inductance profile of a surface mounted permanent magnet transverse flux machine”. The Fifth International Conference on Power Electronics and Drive Systems. IEEE Conferences. Vol. 2, PP 1334–1338. 2003.

[65] K. Y. Lu; E. Ritchie; P. O. Rasmussem; P. Sandholdt. “Modeling and power factor analysis of a single phase surface mounted permanent magnet transverse flux machine” IEEE Conferences. Vol.2 PP: 1609-1613. 2003.

[66] C. Espanet; J-M. Kauffmann; R. Bernard. “Comparison of Two In-Wheel Permanent Magnet Motors for Military Applications”.IEEE Vehicle Power and Propulsion Conference. PP: 1–6. 2006.

[67] M. Gärtner; P. Seibold; N. Parspour. “Laminated circumferential transverse flux machines - lamination concept and applicability to electrical vehicles” IEEE International Electric Machines & Drives Conference (IEMDC). 2011.

[68] K. Y. Lu; E. Ritchie; P. O. Rasmussen; P. Sandholdt. “Modelling a single phase surface mounted permanent magnet transverse flux machine based on Fourier series method”. Electric Machines and Drives Conference, IEMDC'03. IEEE International. vol.1. PP: 340-345. 2003.

[69] I. Hasan; T. Husain; Y. Sozer; I. Husain; E. Muljadi. “Analytical modeling of a double-sided flux concentrating E-Core Transverse Flux Machine with pole windings”. IEEE International Electric Machines and Drives Conference (IEMDC). 2017.

[70] R. H. Manno; E. G. Diez. “Direct force control for a three-phase double-sided linear induction machine with transverse magnetic flux”. 28th Annual Conference of the Industrial Electronics Society. IECON 02. vol.4, PP: 2826-283. 2002.

[71] D. SVECHKARENKO. “Analytical Modeling and Design of a NovelTransverse Flux Generator for Offshore Wind Turbines”. Thesis. Stockholm, Sweden 2007.

[72] H. Weh and H. May, “Achievable force densities for permanent magnet excited machines in new configurations”, in Proc. Int. Conf. on Elec. 1986.

[73] E. Muljadi, C. P. Butterfield and Y. Wan, "Axial-flux modular permanent-magnet generator with a toroidal winding for wind-turbine applications", IEEE Trans. Ind.Applicat., Vol. 35, No. 4, pp. 831-836, July/Aug. 1999.

[74] Jang-Young Choi; Yu-Seop Park; Kyoung-Jin Ko; Seok-Myeong Jang . "Electromagnetic analysis of double-sided axial flux permanent magnet motor with ring-wound type slotless stator based on analytical modeling" International Conference on Electrical Machines and Systems. 2010.

[75] D. Svechkarenko, "On Analytical Modeling and Design of a Novel Transverse Flux Generator for Offshore Wind Turbines", Thesis Stockholm, Sweden 2007.

[76] Gang Lv; Z. Liu; S. Sun. "Analysis of Torques in Single-Side Linear Induction Motor With Transverse Asymmetry for Linear Metro", IEEE Transactions on Energy Conversion. Volume: 31, Issue: 1 PP: 165-173, 2016.

[77] U E. Doğru; N. G. Özçelik; H. Gedik; M. İmeryüz; L. T. Ergene, "Numerical and experimental comparison of TLA synchronous reluctance motor and induction motor". IEEE International Power Electronics and Motion Control Conference (PEMC), 2016.

[78] K. Lu; E. Ritchie. "Preliminary comparison study of drive motor for electric vehicle application", ICEMS Proceedings of the 5th International Conference on. Electrical Machines and Systems Vol.: 2. PP: 995-998 vol.2. 2001.

[79] C. Liu, J. Zhu, Y. Wang, G. Lei, and Y. Guo, "Design Considerations of PM Transverse Flux Machines with Soft Magnetic Composite Cores", IEEE Trans. on App. Superc., 2016.

[80] P. Anpalaham, "Design of transverse flux machines using analytical calculations and finite element analysis", Tech. Licentiate Thesis, Royal Institute of Technology,Stockholm, 2001.

[81] Y.G. Guo, J.G. Zhu, P.A. Watterson and W. Wu, "Development of a PM transverse flux motor with soft magnetic composite core", IEEE Trans. on Ene. Conv., Vol. 21, No. 2, pp. 426-434, June 2006.

[82] D. Svechkarenko, J. Soulard and Chandur Sadarangani, "Analysis of a novel transverse flux generator in direct-driven wind turbines", International Conference on Electrical Machines(ICEM), pp. 424.1-6, Sep. 2006.

[83] G. Kastinger and A. Schumacher, "Reducing torque ripple of transverse flux machines by structural designs", in Proc. 2002 IEE Conf. Power Electronics, Mach. and Drives, pp. 320-324.

[84] J.F. Gieras, "Performance characteristics of a permanent magnet transverse flux generator", in Proc. 2005 IEEE Conf. Elec. Mach. and Drives, pp. 1293-1299.

[85] C. Liu, J. Zhu, Y. Wang, Y. Guo, and G. Lei, "Comparison of Claw Pole Machines with Different Rotor Structures", IEEE Tran. on Mag, 2015.

[86] G.Q. Bao and J.Z. Jiang, "A new transverse flux permanent motor for direct drive application", in Proc. IEEE Conf. Elec. Mach. and Drives, pp. 1192-1195. 2005.

[87] G.Q. Bao, D. Zhang, J.H. Shi and J.Z. Jiang, "Optimal design for cogging torque reduction of transverse flux permanent motor using particle swarm optimization algorithm", in Proc. IEEE Conf. Power Electronics and Motion Control(IPEMC),Vol. 1, pp. 260-263. 2004.

[88] M. Siatkowski; B. Orlik. "Flux linkage in Transverse Flux machines with flux concentration". 11th International Conference on Optimization of Electrical and Electronic Equipment. 2008.

[89] Y. Guo; J. Zhu; H. Lug; S. Wang and J. Jin. "Performance analysis of an SMC transverse flux motor with modified double-sided stator and PM flux concentrating rotor" International Conference on Electrical Machines and Systems (ICEMS) 2007.

[90] B. Zhang; A. S. Wang; M. Doppelbauer . "Optimization of a transverse flux machine with claw-pole and flux-concentrating structure". IEEE International Electric Machines & Drives Conference (IEMDC) 2015.

[91] B. Zhang; A. Wang; Martin Doppelbauer. "Multi-Objective Optimization of a Transverse Flux Machine With Claw-Pole and Flux-Concentrating Structure". IEEE Transactions on Magnetics , Volume: 52, Issue: 8. 2016.

[92] T. Husain; I. Hasan; Y. Sozer; I. Husain and Eduard Muljadi, Design of a Modular E-Core Flux Concentrating Transverse Flux Machine IEEE Transactions on Industry Applications, 2018.

[93] E. Schmidt. "Finite Element Analysis of a Novel Design of a Three Phase Transverse Flux Machine With an External Rotor", IEEE Transactions on Magnetics, Volume: 47, Issue: 5 ;PP: 982 – 985, 2011.

[94] A. Njeh, A. Masmoudi and A. Elantably, "Cogging torque minimization of a claw pole TF-motor: FEA in the Maxwell 3D environment", in Proc. IEEE Conf. Signals, Systems, Decision, and Information Technology (SSD'03), Sousse, Tunisia, March 2003.

[95] M. Dubois, "Optimized permanent magnet generator topologies for direct drive wind turbines", Ph.D. dissertation, Delft University of Technology, Delft, The Netherlands,2004.

[96] M. Siatkowski; B. Orlik, Flux linkage in Transverse Flux machines with flux concentration 11th International Conference on Optimization of Electrical and Electronic Equipment Pages: 21–26, 2008.

[97] Lundmark, S., "Application of 3D computation of magnetic field to the study of claw pole motors."Thesis. 2005.

[98] T. Ackermann, editor. Wind power in power systems. John Wiley & Sons, Ltd, 2005.

[99] J. Manwell, J. McGowan, A. Rogers, "Wind energy explained", Wiley, 2002.

[100] http://www.powergeneration.siemens.com/.Siemens Power Generation GmbH.

[101] http://www.repower.de/, REpower Systems AG.

[102] Multibrid Entwicklungsgesellschaft mbH. http://www.multibrid.com/..

[103] B.J. Chalmers, W. Wu, and E. Spooner. An axial-flux permanent-magnet generator for a gearless wind energy system. IEEE Trans. Energy Conversion, 14(2):251–267, June 1999.

[104] A. Grauers. Design of direct-driven permanent-magnet generators for wind turbines. PhD thesis, Chalmers University of Technology, Gothenburg, Sweden, 1996.

[105] H. Polinder, F.F.A. van der Pijl, G.J. de Vilder, and P. Tavner. Comparison of direct-drive and geared generator concepts for wind turbines. In Proc. IEEE Int. Conf. Electric Machines and Drives, pages 543–550, San Antonio, USA, 2005.

[106] M.R. Dubois. Optimized Permanent Magnet Generator Topologies for DirectDrive Wind Turbines. PhD thesis, Delft University of Technology, Delft, The Netherlands, 2004.

[107] H. Weh, H. Hoffmann, and J. Landrath. New permanent magnet excited synchronous machine with high efficiency at low speeds. In Proc. Int. Conf. Electrical Machines, volume 3, pages 35–40, Pisa, Italy, 1990.

[108] H. Weh and H. May. Achievable force densities for permanent magnet excited machines in new configurations. In Proc. Int. Conf. Electrical Machines, volume 3, pages 1107–1111, Munich, Germany, 1990.

Chapter Two

A-TFPMS Machine Construction and Design Variations

Chapter Two

A-TFPMS Machine Construction and Design Variations

1. Introduction

The design of electrical machines is usually preceded by an initial design during which the requirements of speed and flexibility must be met. In this first phase, analytical models are often used. Numerical models are then exploited to refine the solutions obtained by simulating reliably the electromagnetic, mechanical and thermal behaviors with a minimum of simplistic hypotheses.

This chapter is devoted to the analytical derivation of the basic equations, such as torque, emf, and power for the A-TFPMS machine. The final choice based on this discussion incorporates a double rotors structure on which the magnets are placed. The magnets are located in between three stator quasi-U shape, each having one-phase windings excited in first time with sinusoidal currents, second time with PWM supply by using co-simulation Simplorer and Ansoft Maxwell software.

The design procedure will be developed in the form of a program. The designer can evaluate quickly and give several alternatives. The example will be given on a machine that has been studied and used in wind turbines or electric vehicles. Then, we calculate its various geometric parameters, electrical and magnetic parameters while determining the dimensions and the shape of the permanent magnets.

2. Description of the Machine Prototype and 3D FEM Model

The prototype of the A-TFPMS machine that is the object of study in this chapter, the machine was designed accordingly to biographic research which has been discussed in Chapter 1. The stator consists of three rings, each of them for different phase. The rotor, placed inside of the stator, has also three ferromagnetic rings attached to the rotor shaft. Two rows of PMs are glued to each of the rotor back iron.

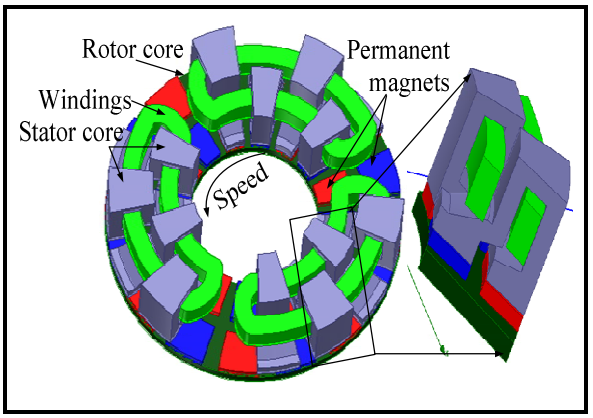

(a) (b)

Fig.2.1: (a) 3-D model first design of A-TFPMS machine, (b) two poles pairs of A-TFPMSM.

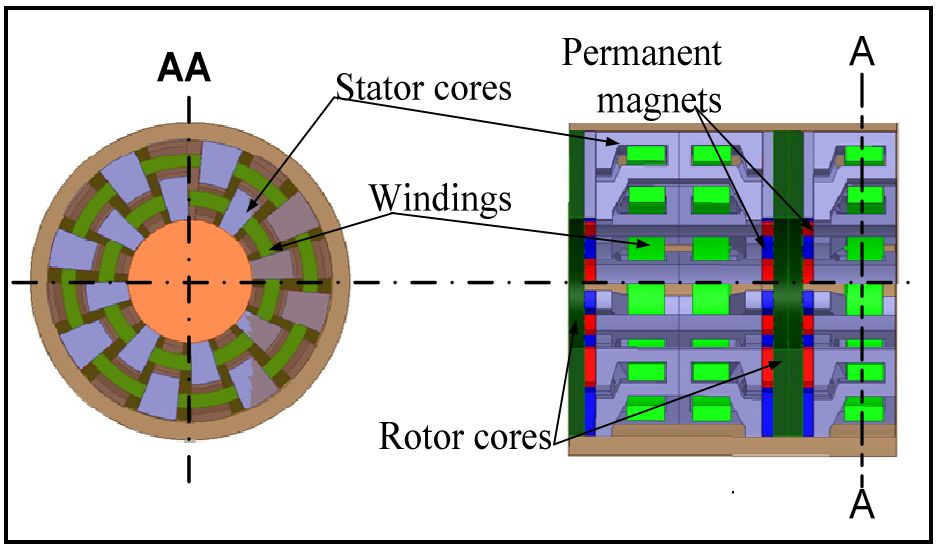

Fig. 2.2: Scheme of second design PMTF machines designed.

In Fig. 2.1, the stator winding form is ring portion, in this design has two disadvantages, the one is the end rings and the second is the poles pitch of the

stator and the rotor aren't equals. And in the anther side the main advantage of this design is, can be use it as simple face or multi face.

For analyzing the generator performance its 3D FEM model was built. Since all three parts of the generator do not influence one another magnetically the analysis of the generator operation can be carried out for a single phase. The structure of one machine phase is shown schematically in Fig. 2.3.

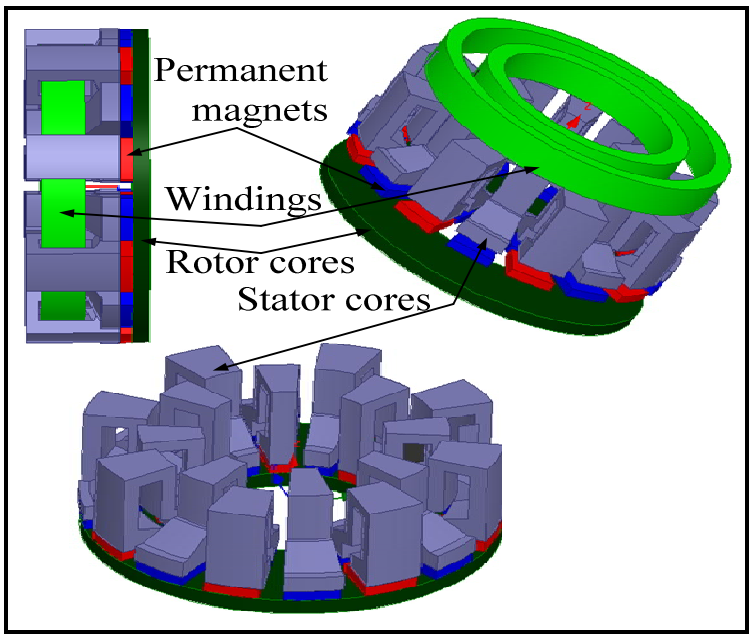

Fig. 2.3: Machine structure for one phase.

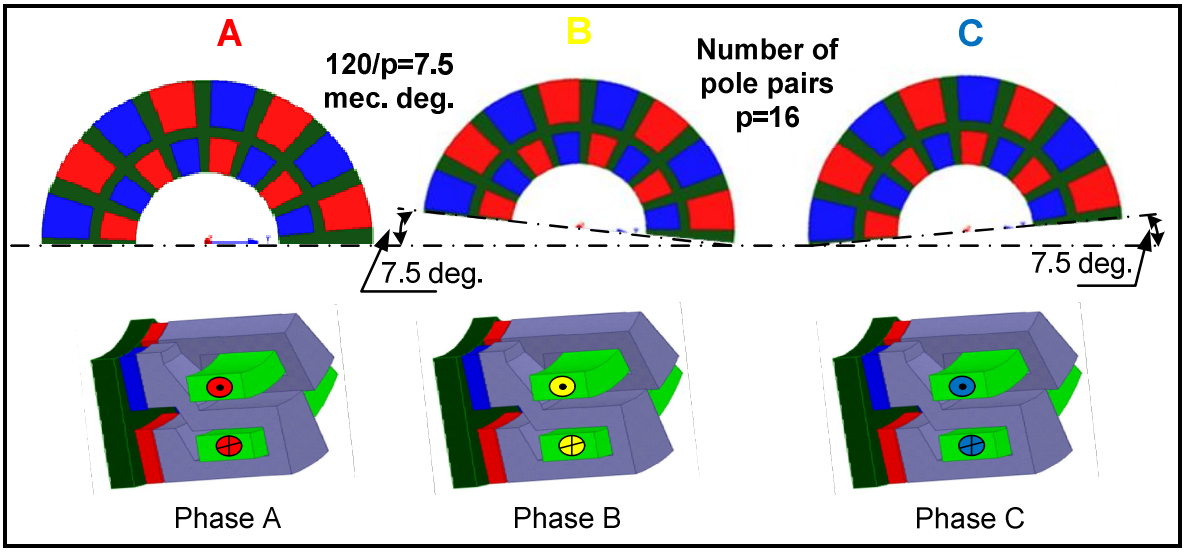

Fig. 2.4: PMs rotor layout for 3 phases machine configuration.

The stator core has 12 U-shape poles made of laminated steel. The stator winding has a form of double O-ring and is placed inside of the core poles. The rotor ring, made of solid iron, has two rows of PMs with 24 magnets in each row. The design parameters of the machine for a single phase are enclosed in Table 2.1. The dimensions of the stator and rotor parts shown in Fig. 2.4 are enclosed in Table 2.2.

Description	**Symb.**	**Value**
Output power	S	2KW
Input voltage	V_{ph}	220V
Speed	n	375rpm
Coercive field magnets	H_c	90KA/m
Peak current	I_a	10A
Flux density of PM	B_r	1.2T
Average magnetic flux density in the air gap	B_{av}	0.9T
Flux density in the stator core	B_{SFe}	1.6T
Flux density in the rotor core	B_{rFe}	1.6T
Wire current density	J_w	$4A/mm^2$
Supply Frequency	f	100Hz
Air gap	g	0.5mm
Magnet type	NdFeB	1.3 T
Current loading density	J	19KA/m
Poles numbers	p	32
Number of windings turns	N	220
Coefficient $B_{av} / B_{\max}$	C_m	0.9
Winding filling coefficient	K_w	0.7
Iron core type		-Steel 1008 -Iron- Si3% -SMC

Table 2.1 Specifications of the Designed A-TFPMS Machine.

The magnetic flux set by the PMs during the rotation is closed through the stator poles in axially oriented plane. When the rotor rotates its magnets change their polarity with respect to the stator pole inducing voltage in the stator winding with frequency (f=n*p/60) Where ***p***. is the number of poles pairs on the rotor circumference and ***n*** is the rotor speed in rpm.

To obtain a phase shift between phase voltages permanent magnets of each phase must be displaced by 120 electrical degrees (7.5 mechanical degrees). The magnet axial layout is shown in Fig. 2.5.

3. Electromechanical Parameters of A-TFPMS Machine

The estimated electromechanical parameters of the machine which will calculate in the next step are shown in Table 2.1.

3.1 Determination of Design Parameters of A-TFPMS Machine

To determine the provisional dimensions of the generator the magnetic circuit model is applied in which the real machine is simplified. This simplification is described by the assumptions that are declared. Once the dimensions are determined and the winding parameters are calculated the generator is modeled in FEM software and its designed parameters are optimized.

3.2 Magnetic Circuit Model of the Generator and Design Calculations

The machine model is defined by following assumptions:

- The magnetic permeability of the stator and rotor cores is infinitely high.
- The magnetic flux that links the stator winding changes in time sinusoidally.
- There is no magnetic link between phase windings.
- The coil current does not influence the magnetic flux in the air-gap which is set by the permanent magnets.

The initial data of the generator to be designed are as follows (Table 2.1):

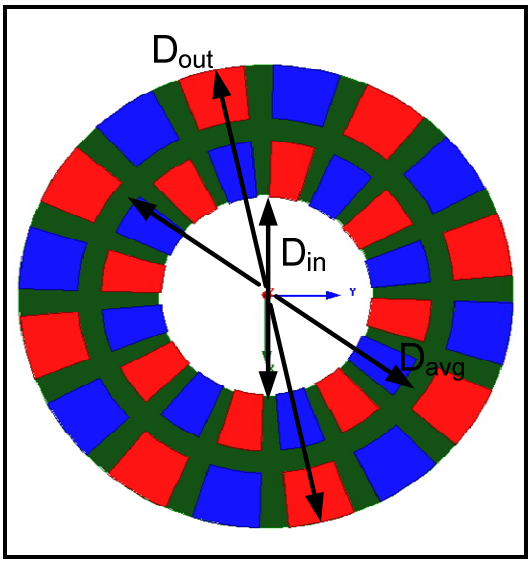

Fig. 2.5 Dimensionig details of A-TFPMS machine.

3.3 Determination of Generator Dimensions.

- Magnet height.

Referring to Fig. 2.6, equations for calculating the magnet height can be derived. The magnet height depends on the type of magnet material (its B-H characteristic) and the air-gap. To derive the equation for the magnet height let the half of stator pole rotor magnet be considered as in Fig. 2.7.

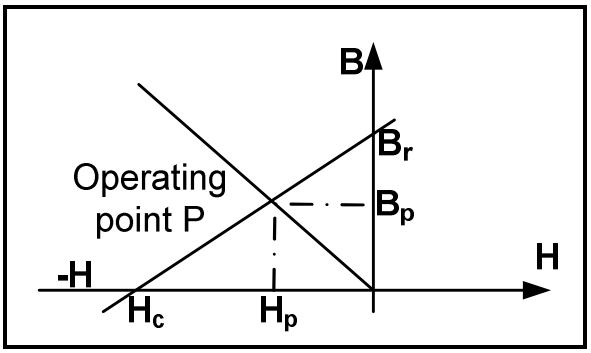

(a)

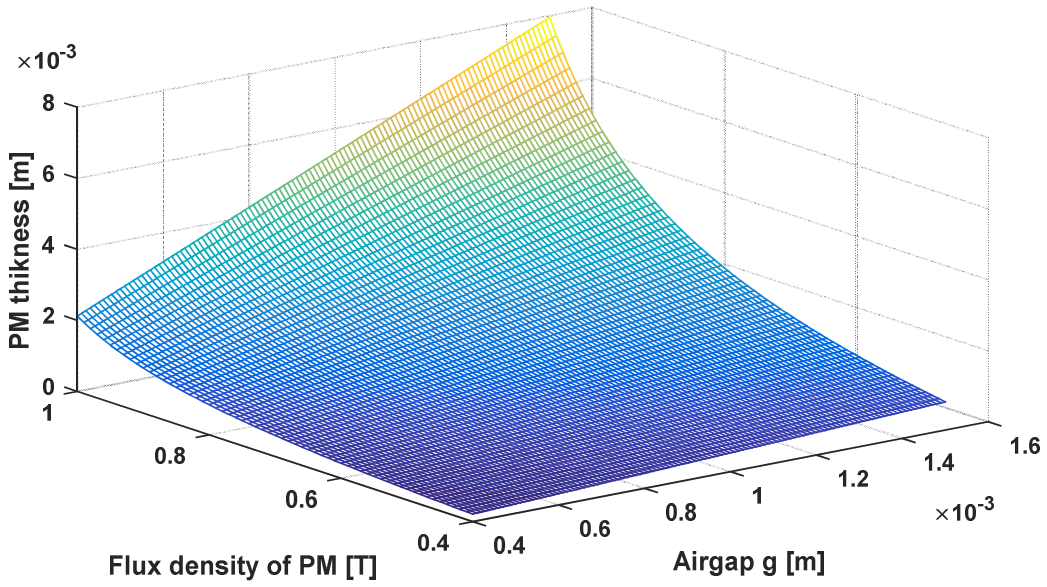

(b)

Fig. 2.6: (a) Demagnetization part of B-H characteristic for air gap and (b) PM thickness variation.

The permanent magnet operating point are presented in Fig. 2.6 (a), therefore, its mention as static operating point, in fact this point are dynamic. I will try to present dynamic operating point by using a FEA in the next chapter.

Assuming stator and rotor core permeability $mu_c = \infty$ according to Ampere law

$$H_{PM} h_{PM} + H_g g = 0 \tag{2.1}$$

Where

H_{pm} Magnetic field intensity of the PM

H_g Magnetic field intensity of the air gap

h_{PM} Magnet high

g Air gap width

From equation 2.1 the field intensity in the air gap is

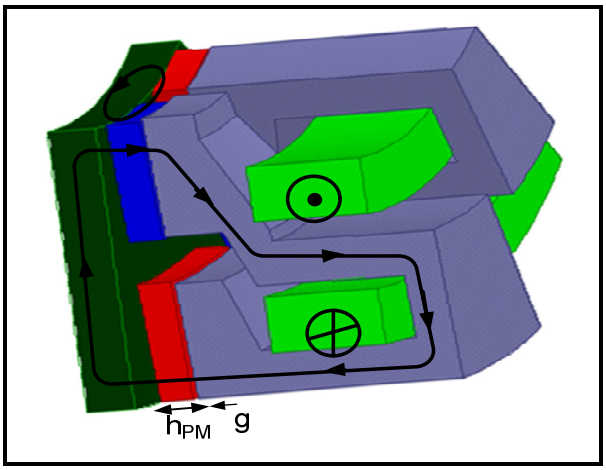

Fig. 2.7 Stator and rotor poles with PM

$$H_g = -\frac{h_{PM}}{g} H_{PM} \tag{2.2}$$

After multiplication by ***μ_0***

$$B_g = -\frac{h_{PM}}{g} H_{PM} \mu_0 \tag{2.3}$$

Since for NdFeBo magnets the demagnetization curve shown in Fig 2.6 is straight line it can be described as

$$\begin{cases} B_m = \dfrac{B_r H_{PM}}{|H_c|} + B_r \\ H_{PM} = \dfrac{(B_m - B_r)|H_c|}{B_r} \end{cases} \tag{2.4}$$

For air gap from equ 2.2

$$H_{PM} = -\frac{B_g g}{\mu_0 h_{PM}} \tag{2.5}$$

Equaling equations 2.4 and 2.5 for H_{PM} gives

$$-\frac{B_g g}{\mu_0 h_{PM}} = \frac{(B_m - B_r)|H_c|}{B_r} \tag{2.6}$$

At the operation point P $B_m=B_g$ thus solving 2.6 for h_{PM}

$$h_{PM} = \frac{g B_r B_g}{\mu_0 |H_c| (B_r - B_g)} \tag{2.7}$$

- Number of poles pairs *p* is found from

$$p = \frac{120 f}{n} \tag{2.8}$$

- Stator outer diameter $\boldsymbol{D_{out}}$ calculation

The stator outer diameter can be found from the equation for the input power $\boldsymbol{S_{ph}}$ considering one phase

$$S_{ph} = E_{ph} I_a \tag{2.9}$$

Where

$\boldsymbol{I_{ph}}$ is RMS current and $\boldsymbol{E_{ph}}$ is RMS EMF.

$$E_{ph} = 2\pi f \phi_{\max} N_{ph} K_f \tag{2.10}$$

Where

N number of turns per phase

$\boldsymbol{\Phi_{max}}$ Maximum in time flux

The magnetic flux $\boldsymbol{\Phi_{max}}$ is found as

$$\phi_{\max} = B_{av} A_{PM} \tag{2.11}$$

Where $\boldsymbol{A_{PM}}$ is section area under the stator pole in the air gap

$$A_{PM} = \alpha D_{out}^2 \left(1 - K_d^2\right) \tag{2.12}$$

Where $K_d = \frac{D_{in}}{D_{out}}$

α Pole arc coefficient (=0.83)

Hence,

$$\phi_{\max} = \frac{\pi}{8} D_{out}^2 \left(1 - K_d^2\right) B_{av} \tag{2.13}$$

Substituting 2.13 into 2.12 the induced phase voltage is

$$E_{ph} = \sqrt{2}\pi f \frac{\pi}{8} B_{av} N_{ph} K_f D_{out}^2 \left(1 - K_d^2\right) \tag{2.14}$$

Expressing the voltage frequency as

$$f = pn/120 \tag{2.15}$$

And substituting 2.14 into 2.9 the equation for input power **S_{ph}** looks like

$$S_{ph} = \sqrt{2}\pi f \alpha B_{av} N_{ph} K_f D_{out}^2 \left(1 - K_d^2\right) I_a \tag{2.16}$$

Since the current loading

$$J = \frac{2\sqrt{2} N_{ph} I_a}{\pi D_{avg}} \tag{2.17}$$

Where $D_{avg} = 0.5\left(D_{out} + D_{in}\right) = 0.5 D_{out}\left(1 + K_d\right)$

Substituting it into 2.16 results

$$S_{ph} = \frac{1}{4}\pi^2 \frac{pn}{120} J K_f \alpha B_{av} D_{out}^3 \left(1 - K_d^2\right)\left(1 + K_d\right) \tag{2.18}$$

From this equation of the power generator, the outer of the machine is found

$$D_{out} = \sqrt[3]{\frac{S_{ph}}{\frac{1}{4}\pi^2 \frac{pn}{120} J K_f B_{av} \left(1 - K_d^2\right)\left(1 + K_d\right)}} \tag{2.19}$$

D_{out} can be assumed on this stage of calculation. The assumption is based on the choice of the designer who can decide about generator proportion as inner diameter to the outer diameter ratio.

- Pole pitch of the stator poles τ at outer diameter is determined by

$$\tau = \frac{D_{out}\pi}{p/2} \tag{2.20}$$

Since, according to design configuration Fig 2.5

- Stator inner periphery

$$D_{in} = K_d D_{out} \tag{2.21}$$

- Stator core height

$$h_s = h_{s1} + h_{st} + w_{st} tg\gamma \tag{2.22}$$

- Width of stator shoe

$$2w_{st} = K_{PM}\left(R_o - R_{\text{in}}\right)/2 \tag{2.23}$$

- Magnet PM length

$$l_{pm} = \frac{K_{PM}\left(R_o - R_i\right)}{2} \tag{2.24}$$

Where ***K_{PM}*** radial length PM coefficient (=0,83)

- Width of the stator core see Fig 2.8

$$b_{st} = \frac{B_{av} w_{st}}{B_{sFe}} \tag{2.25}$$

- high of stator yoke

$$h_{sy} = b_{st} \tag{2.26}$$

- High of the rotor core

$$h_r = \frac{B_{av} w_{st}}{B_{rFe}} \tag{2.27}$$

- Width of the stator coil

$$b_s = w_{st} - b_{st} \tag{2.28}$$

- Rotor inner diameter

$$D_{rout} = D_{out} \tag{2.29}$$

- Rotor outer diameter

$$D_{rin} = D_{in} \tag{2.30}$$

3.4 Determination of Machine Torque

The maximum no load flux is achieved when the rotor magnets and the stator cores are aligned. Accordingly this position will be taken as the initial position for the analysis. According to rotor rotation the air-gap can be expressed as:

$$\varphi = k_f \Phi_{gap} \cos \omega t \tag{2.31}$$

Where $\boldsymbol{K_f}$ is the air-gap flux waveform coefficient [1], and $\boldsymbol{\Phi_{gap}}$ is the maximum value of the no load flux.

The flux coefficient in Eq. (2.31) can be achieved as:

$$k_f = \frac{8}{\pi} \sin \frac{\alpha \pi}{2} \tag{2.32}$$

Where $\boldsymbol{a}$ is the pole arc coefficient in the rotational direction.

For $I_d=0$ the total current $I_a=I_q$ is torque producing and the angle between the current and the EMF is 0 i.e. $\cos\psi = 1$

The generated electromagnetic power of A-TFPMSM is

$$P_{elem} = m\sqrt{2}2\pi k_f f N_{ph} \Phi_{gap1} I_a \left(\frac{1 - \cos 2\omega t}{2} \right) \tag{2.33}$$

Where Φ_{gap1} is the fundamental main flux will calculate by MEC (Magnetic Equivalent Circuit) method in the last chapter, p is the number of pole pairs, and m is the number of phases. The torque can be obtained by

$$T = \frac{P_{elem}}{2\pi n} = \sqrt{2} mpN_1 \Phi_{gap1} I_a \left(\frac{1-\cos 2\omega t}{2} \right) \tag{2.34}$$

From Eq. (2.34) the torque of one phaseof A-TFPMS machine is sinusoidal. The torque waveform has two peaks, and the average torque is different from zero.

The electromagnetic torque peak for one phase is

$$T_{\max} = \frac{1}{2} \sqrt{2} mpN_{ph} \Phi_{gap1} I_a \tag{2.35}$$

The angle between the phase currents is $2\pi/3$; the three phase torques T_A, T_B and T_C can be written as follows:

$$\begin{cases} T_A = \sqrt{2} mpN_{ph} \Phi_{gap1} I_a \dfrac{1}{2} (1-\cos 2\omega t) \\ T_B = \sqrt{2} mpN_{ph} \Phi_{gap1} I_a \dfrac{1}{2} \left(1-\cos\left(2\omega t - \dfrac{2\pi}{3} \right) \right) \\ T_C = \sqrt{2} mpN_{ph} \Phi_{gap1} I_a \dfrac{1}{2} \left(1-\cos\left(2\omega t + \dfrac{2\pi}{3} \right) \right) \end{cases} \tag{2.36}$$

The total torque is the sum of the all torques generated by the three phase power supply, that is

$$T = T_A + T_B + T_c = \frac{3}{2} \sqrt{2} mpN_{ph} \Phi_{gap1} I_a \tag{2.37}$$

3.5 Determination of Machine Winding Parameters

Due to the voltage drop across generator phase impedance, the output voltage V_{ph} is smaller than EMF E_{ph} and this can be expressed by coefficient K_E thus electromotive force.

$$E_{ph} = \frac{V_{ph}}{K_E} \tag{2.38}$$

Where K_E is the EMF to voltage ration

Number of turns N_{ph} can be found rearranging the equation 2.14 for electromotive force

$$N_{ph} = \frac{V_{ph}}{\sqrt{2}\pi f \alpha B_{av} K_f K_E D_{out}^2 \left(1 - K_d^2\right)} \tag{2.39}$$

Calculated number of turns N_{ph} can be rounded by a designer, verified to satisfy phase

Wire nude section mm²	Wire nude diameter mm	Wire Diameter with 1 insulation layer mm	Wire Diameter with 2 insulation layer mm
0.384	0.7	0.79	0.86
0.411	0.75	0.84	0.91
0.502	0.8	0.89	0.96
0.975	0.9	1.03	1.08
1.08	1	1.13	1.18
1.18	1.1	1.23	1.28
1.28	1.2	1.33	1.38
1.33	1.25	1.38	1.43
1.38	1.3	1.43	1.48
1.48	1.4	1.53	1.58
1.585	1.5	1.63	1.72
1.685	1.6	1.75	1.82
1.785	1.7	1.85	1.92
1.885	1.8	1.95	2.02
2.09	2	2.15	2.22

Table 2.2: Standardization wire diameter winding for electrical machines [ ].

For a three phase Y connected supply, depending on load power factor cos(phi) the current rating is obtained:

$$I_a = \frac{S}{3V_{ph}} \tag{2.40}$$

- Wire diameter

$$d_w = \frac{2I_a}{J_w \pi} \tag{2.41}$$

Based on the calculated wire diameter, the wire type can be selected from gauge table (Table 2.2) which is shown below

- Coil cross section area is

$$A_c = \frac{\pi d_w^2}{4} N_{ph} \tag{2.42}$$

Parameter	Value (mm)	Parameter	Value (mm)
PM thickness	h_{PM}=6mm	High of stator shoe	h_{st}=11mm
PM length	l_{PM}=15mm	High of rotor	h_r=10mm
Width of stator coil	b_s=15mm	Width of stator shoe	w_{st}=27mm
Width of stator core	b_{st}=10mm	Inner diameter	R_i=50mm
High of stator	h_s=56mm	Outer diameter	R_o=95mm
High of stator yoke	h_{sy}=10mm	Pole pitch	τ=37.3mm
High of stator coil	h_{s1}=32mm	Pole arc coefficient	α=0.80

Table 2.3: Geometrical Parameters of the Designed A-TFPMS Machine.

- Total area of the slot is calculated taking into account winding insulation

$$A_{slot} = \frac{A_c}{K_w} \tag{2.43}$$

Where $\boldsymbol{K_w}$ is winding filing coefficient

- Height of the coil

$$h_c = \frac{A_{slot}}{b_s} \tag{2.44}$$

- Actual height of the stator core

$$h_{s1} = h_c + h_{sy} \tag{2.45}$$

- Average length of the coil, in A-TFPMs machine the coil have two ring, one outer and another inner, the total length is

$$L_c = L_{cout} + L_{cin} = \left(\pi(D_{sout} - 2b_{st}) + \pi(D_{\sin} + 2b_{st})\right) N_{ph} \tag{2.46}$$

3.6 Leakage and Armature Reaction Reactance

The mutual reactance corresponding to the armature reaction reactance in a synchronous machine can analytically be calculated in an approximate way. One quasi C-shaped core (pole pair) of the stator can be regarded as an AC electromagnet with $\boldsymbol{N_{ph}}$ turn coil which, when fed with the sinusoidal current $\boldsymbol{I_a}$, produces peak MMF equal to $\sqrt{2}I_a N_{ph}$. The equivalent d-axis field MMF per pole pair per phase which produces the same magnetic flux density as the armature reaction MMF is

$$\sqrt{2}I_{ad}N_{ph} = \frac{B_{ad}}{\mu_0}g' = \frac{B_{ad1}}{\mu_0 k_{fd}}g' \tag{2.47}$$

Where ***g'*** is the equivalent air gap and k_{fd} is the d-axis form factor of the armature reaction.

$$k_{fd} = \frac{\alpha\pi + \sin\alpha\pi}{\pi} \tag{2.48}$$

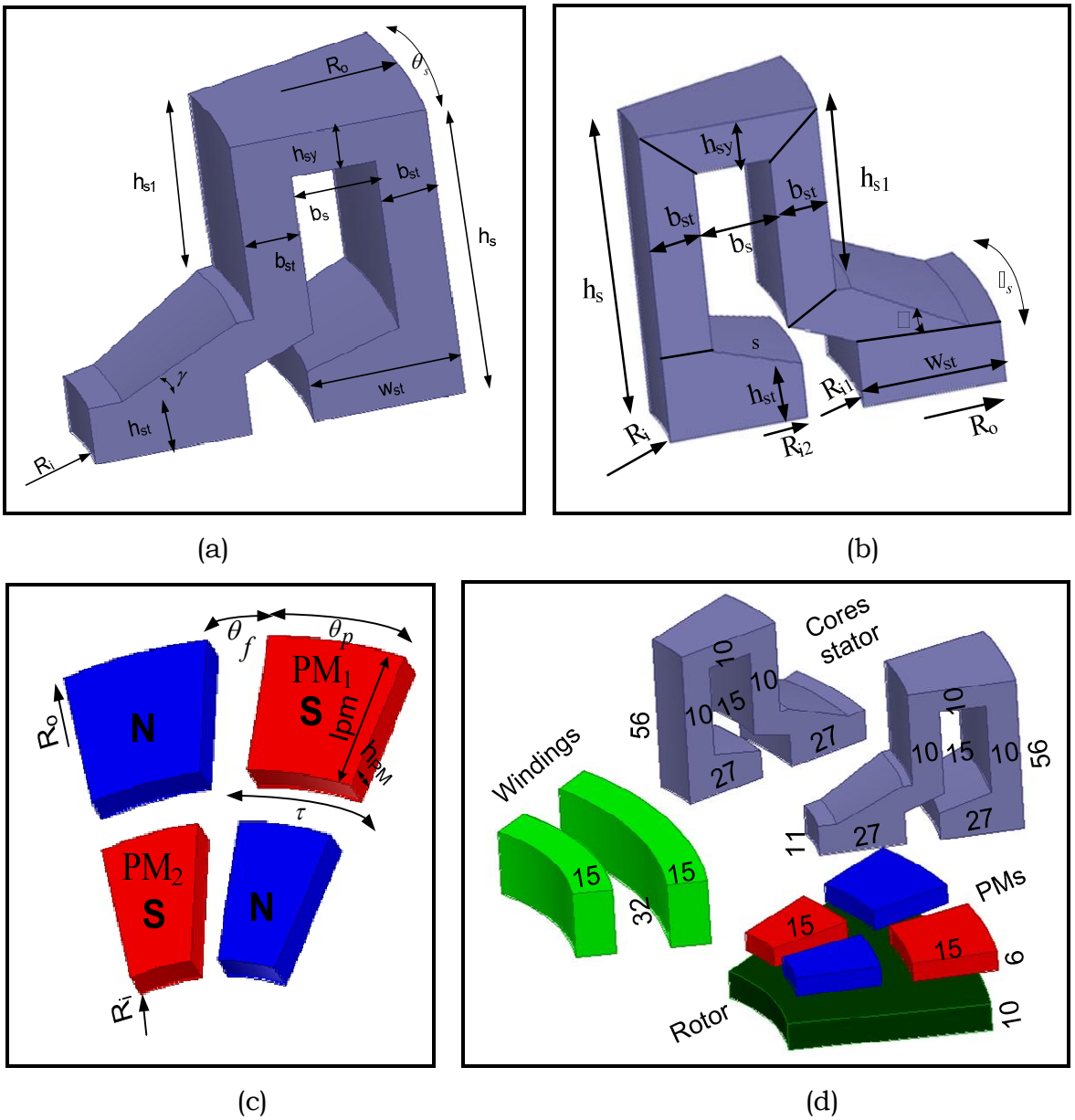

Fig.2.8: Machine dimensions. (a) (b) Stator cores, (c) Permanents magnets and (d) final dimensions all in (mm).

Thus, the d-axis armature current is

$$I_{ad} = \frac{B_{ad1}}{\mu_0 k_{fd}} \frac{g'}{\sqrt{2} N_{ph}} \tag{2.49}$$

At constant magnetic permeability, the d-axis armature EMF

$$\sqrt{2}I_{ad}N_{ph} = \frac{B_{ad}}{\mu_0}g' = \frac{B_{ad1}}{\mu_0 k_{fd}}g' \tag{2.50}$$

At constant magnetic permeability, the d-axis armature EMF

$$E_{ad} = 2\sqrt{2}fN_{ph}p\tau w_{st}B_{ad1} \tag{2.51}$$

Thus the d-axis armature reaction reactance is

$$X_{ad} = \frac{E_{ad}}{I_{ad}} = 4\mu_0 fN_{ph}^2 p\frac{\tau w_{st}}{g'}k_{fd} \tag{2.52}$$

$$X_{aq} = \frac{E_{aq}}{I_{aq}} = 4\mu_0 fN_{ph}^2 p\frac{\tau w_{st}}{g'}k_{fq} \tag{2.53}$$

Where $\boldsymbol{k_{fq}}$ is the q-axis form factor of the armature reaction.

$$k_{fq} = \frac{\alpha\pi - \sin\alpha\pi}{\pi} \tag{2.54}$$

Where $\boldsymbol{\alpha}$ is pole arc coefficient, equal the pole-shoe arc-to-pole pith ration ($\alpha<1$)

The d and q-axis form factors of the armature reaction are calculated in [1]. Most TFMs are designed with surface configuration of PMs and $k_{fd}=k_{fc}=1$ ($X_{ad}=X_{aq}$).

Neglecting the saturation of the magnetic circuit, the equivalent air gap is calculated as

$$g' = 2\left(g + \frac{h_{PM}}{\mu_{rrec}}\right) \tag{2.55}$$

Where $\boldsymbol{g}$ is the mechanical clearance in the d-axis, $\boldsymbol{h_{PM}}$ the radial height of the PM and $\boldsymbol{\mu_{rrec}}$ is the relative recoil magnetic permeability of the PM. To take into account the magnetic saturation, the air gap $\boldsymbol{g}$ should be multiplied by the saturation factor $\boldsymbol{k_{sat}}$ and Carter's coefficient $\boldsymbol{k_c}$.

The armature reaction inductances

$$L_{ad} = \frac{X_{ad}}{2\pi f} = \frac{2}{\pi}\mu_0 N_{ph}^2 p\frac{\tau w_{st}}{g'}k_{fd} \tag{2.56}$$

$$L_{aq} = \frac{X_{aq}}{2\pi f} = \frac{2}{\pi}\mu_0 N_{ph}^2 p\frac{\tau w_{st}}{g'}k_{fq} \tag{2.57}$$

The leakage inductance of the stator winding is approximately equal to the sum of the slot leakage inductance and pole-top leakage reactance. The approximate equation is

$$L_s = \mu_0\pi N_{ph}^2\left(\left(2R_o - h_c + h_{st}\right)\cdot\left(\lambda_{ls} + \lambda_{lp}\right)\right) \tag{2.58}$$

Where h_c , is the height of coil, $h_c=h_{s1}-h_y$ and h_{st} is the top portion of the "slot" not filled with conductors.

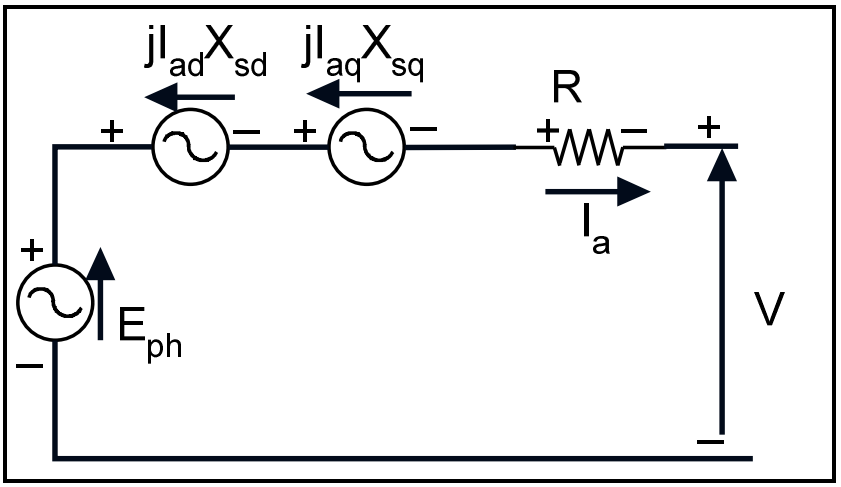

Fig.2.9: Equivalent circuit per phase of an A-TFPMs synchronous machine.

The coefficients of leakage permeances are

- Coefficient of slot leakage permeance

$$\lambda_{ls} = \frac{h_c}{3b_s} + \frac{h_{st}}{b_s} \tag{2.59}$$

- Coefficient of pole-top leakage permeance

$$\lambda_{lp} \approx \frac{5g/b_s}{5+4g/b_s} \tag{2.60}$$

Where λ_{ls} and λ_{lp} are coefficients of slot permeance and pole-top leakage permeance respectively. For most TFPMs $L_s>L_{ad}$ and $L_s>L_{aq}$. The synchronous reactances in the d and q axis are the sums of the armature reaction reactances and leakage reactance $X_s=2\pi fL_s$.

3.7 Characteristics of A-TFPMs Synchronous Machine

When drawing phasor diagrams of synchronous machines (Fig. 2.9), for generator system:

$$\begin{aligned} E_{ph} &= V + I_a R + jI_{ad}X_{sd} + jI_{aq}X_{sq} \\ &= V + I_{ad}\left(R + jX_{sd}\right) + I_{aq}\left(R + jX_{sq}\right) \end{aligned} \tag{2.61}$$

With $X_{sd} = X_s + X_{ad}$ and $X_{sq} = X_s + X_{aq}$ are the d-axis and-axis synchronous reactance.

Where $I_{ad} = I_a \sin\Psi$ and $I_{aq} = I_a \cos\Psi$

The angle Ψ is between the q-axis and armature current I_a.

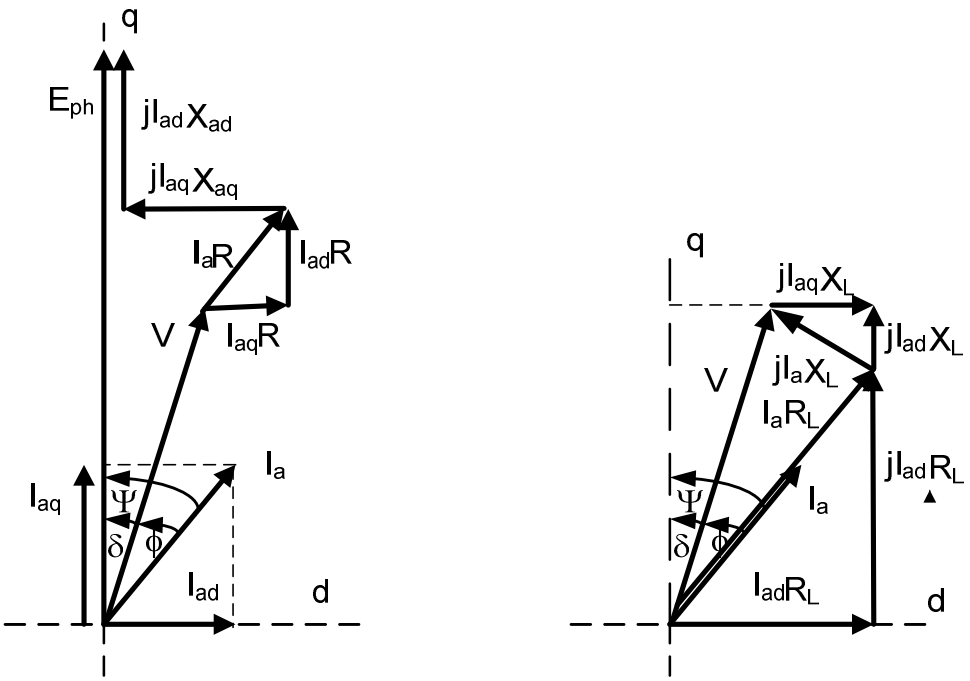

Fig.2.10: Phasor diagram of synchronous generator machine for RL load.

the projection of voltage vector in phasor diagram on d-axis and q-axis as

$$\begin{aligned} V\sin\delta &= I_{aq}X_{sq} - I_{ad}R \\ V\cos\delta &= E_{ph} - I_{ad}X_{sd} - I_{aq}R \end{aligned} \tag{2.62}$$

And by using phasor diagram of synchronous generator machine for RL load (for load side)

$$\begin{aligned} V\sin\delta &= I_{ad}R_L - I_{aq}X_L \\ V\cos\delta &= I_{ad}X_L + I_{aq}R_L \end{aligned} \tag{2.63}$$

Where δ is the load angle between the voltage V and EMF (q-axis), and $Z = R_L + jX_L$ is the load impedance per phase across the output terminals. The d-axis and q-axis currents are

- By using the equation (2.62) for calculating I_{ad} and I_{aq}

$$\begin{aligned} I_{ad} &= \frac{E_{ph}X_{sq} - V\left(X_{sq}\cos\delta + R\sin\delta\right)}{X_{sd}X_{sq} + R^2} \\ I_{aq} &= \frac{E_{ph}R + V\left(X_{sd}\sin\delta - R\cos\delta\right)}{X_{sd}X_{sq} + R^2} \end{aligned} \tag{2.64}$$

- By using the equation (2.63) for calculating I_{ad} and I_{aq}

$$I_{ad} = \frac{V\left(X_{sq}\cos\delta + R\sin\delta\right)}{X_L^2 + R_L^2}$$
$$I_{aq} = \frac{V\left(R_L\sin\delta - X_L\cos\delta\right)}{X_L^2 + R_L^2} \quad (2.65)$$

The load angle between the voltage $\boldsymbol{V}$ and EMF can be determined, from equation (2.62)

$$\delta = \arcsin\left(\frac{I_{ad}R_L - I_{aq}X_L}{V}\right) \quad (2.66)$$

Combining equations (2.62) and (2.63), the d-axis and q-axis currents are independent of the load angle δ.

$$I_{ad} = \frac{E_{ph}\left(X_{sq} + X_L\right)}{\left(X_{sd} + X_L\right)\left(X_{sq} + X_L\right)\left(R + R_L\right)^2}$$
$$I_{aq} = \frac{E_{ph}\left(R + R_L\right)}{\left(X_{sd} + X_L\right)\left(X_{sq} + X_L\right)\left(R + R_L\right)^2} \quad (2.67)$$

The angle $\boldsymbol{\Psi}$ between the current $\boldsymbol{I_a}$ and d-axis and the angle $\boldsymbol{\phi}$ between the current $\boldsymbol{I_a}$ and voltage $\boldsymbol{V}$ are respectively.

$$\psi = \arccos\left(\frac{I_{aq}}{I_a}\right) = \arccos\left(\frac{I_{aq}}{\sqrt{I_{ad}^2 + I_{aq}^2}}\right) \quad (2.68)$$

$$\phi = \arccos\left(\frac{I_a R_L}{V}\right) \approx \frac{E_{ph} - I_a R}{V} \quad (2.69)$$

4. Losses and Efficiency

In order to estimate the efficiency accurately, much attention is paid to the calculation of the losses. The calculation of the loss components and the prediction of the machine's efficiency map are discussed. The loss components of the machine can be summarized as

$$P_{loss} = P_{fe} + P_{cu} + P_{ro} + P_{mec} \quad (2.70)$$

Where P_{fe}, P_{cu}, P_{ro}, P_{mec} are stator core (iron) losses, copper losses, rotor eddy current losses and mechanical losses respectively.

4.1 Core Losses

The core losses are generally the second largest loss component in AC machines [2]. The magnetic flux in the stator core is nonsinusoidal. The rotor

PM produces a trapezoidal shape of the magnetic flux density waveform, normally; core losses in the stators are viewed as being caused mainly by the fundamental frequency variation of the magnetic field. The stator windings are fed from sources sinusoidal or with PWM control. Moreover the exposure to the flux density variation at different parts of the core is not the same, especially in an A-TFPMs machine, where the slot to tooth ratio changes with the radius.

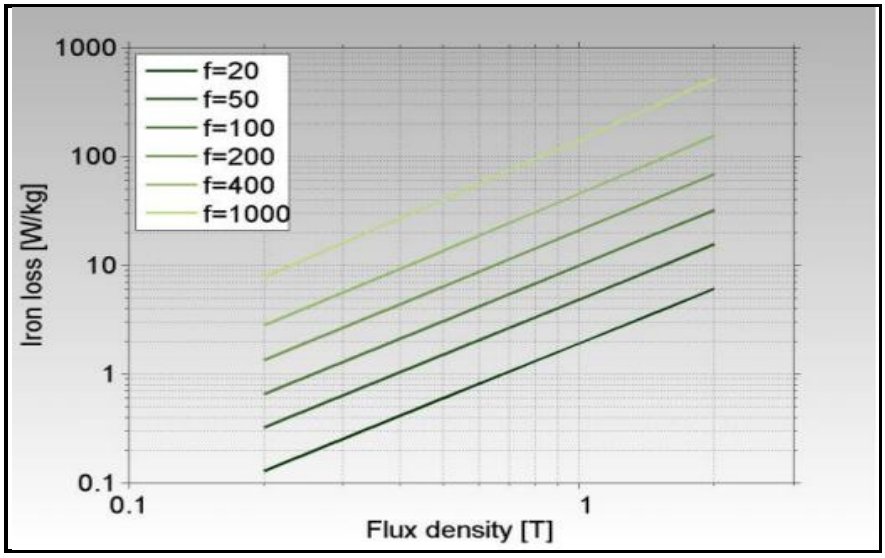

(a)

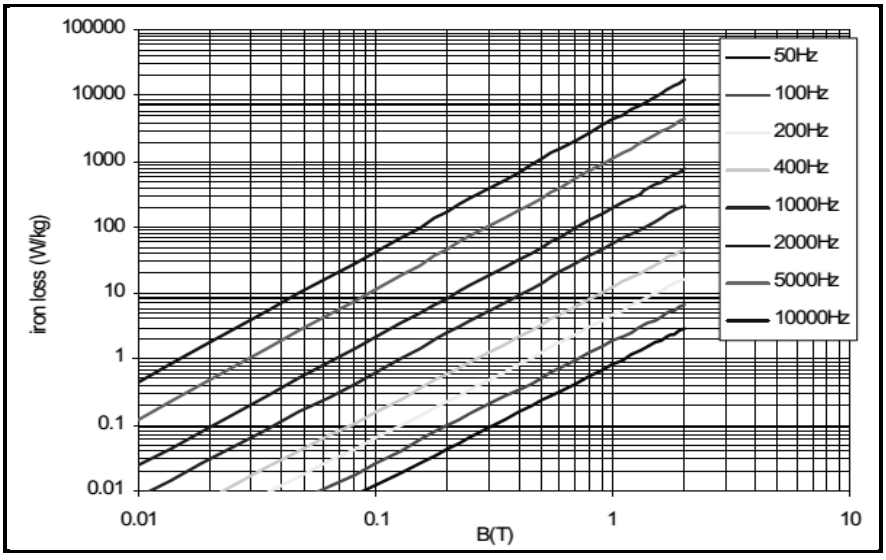

(b)

Fig.2.11: Iron loss as a function of flux density at different frequencies, (a) for SMC materiel at a mechanical density of 7390Kg/m^3 and (b) for Fe-Si 3% grain-oriented silicon steel materiel.

The eddy current losses can be calculated using the following classical formula [3].

$$P_{fe} = P_{efe} + P_{hfe} \tag{2.71}$$

$$P_{efe} = \frac{\pi^2}{6}\frac{\sigma_{sc}}{\rho_{sc}} f^2 d_{sc}^2 m_{sc} \left(B_{sx1}^2 + B_{sz1}^2\right)\eta_d^2 \tag{2.72}$$

Where σ_{sc} , d_{sc} , ρ_{sc} and m_{sc} are the electric conductivity, thickness, specific density and mass of laminations respectively, B_{sx1} and B_{sz1} are the harmonic components of the magnetic flux density in the x (tangential) and z (normal) directions, and η_d is the coefficient of distortion of the magnetic flux density (≤1).

In a similar way, the hysteresis losses can be expressed with the aid of Richter's formula [3].

$$P_{hfe} = \varepsilon \frac{f}{100} m_{sc} \left(B_{sx1}^2 + B_{sz1}^2\right)\eta_{sc}^2 \tag{2.73}$$

Where ε=1.2 to 2m⁴/(HKg)for anisotropic laminations with 4% *Si*, ε=3.8.m⁴/(HKg) for isotropic laminations with 2% *Si* and ε=4.4 to 4.8m⁴/(HKg) to for isotropic siliconless laminations.

If the specific core losses are known, the stator core losses can be calculated on the basis of the specific core losses of materiel are used in Fig.2.11, The power loss data of the materials, is used to fit the Bertotti equation that describes the specific loss in W/kg by using the Bertotti equation [4] [5] as

$$P_{fe} = P_{hfe} + P_{efe} + P_{exc} = k_h f\widehat{B}^2 + k_e \widehat{B}^2 f^2 + k_{ex}\left(\widehat{B}f\right)^{3/2} \tag{2.75}$$

Where k_h, k_e, and k_{ex} are constants determined by manufacturer's data. Due to the difficulty of using a laminated stator core made by thin silicon steel sheets, the SMC soft magnetic component is chosen for the prototype machine.

4.2 Copper Losses

The JOLL losses cover a large part of the total losses. They depend on the load as well as the temperature of the windings. It should be noted that in an electrical machine, the major part of the copper losses is generated in the end windings rather than in the slots (especially in disk shape). However, in order to increase the efficiency of our design A-TFPMS, the end winding doesn't exist.

The design of the windings and the dimensions of the slots were discussed in previous paragraph. The length of a turn is written by (2.46).

The phase resistance is

$$R_{ph} = \frac{\rho L_c}{\pi d_w^2} \tag{2.76}$$

Where ρ and d_w are the resistivity of the copper, and the wire diameter of the conductor respectively.

The resistance of the conductor is a function of the temperature as

$$R_{ph}(T_2) = R_{ph}(T_1)\left[1 + \alpha_{T_1}(T_2 + T_1)\right] \tag{2.77}$$

Where α_{T1} is the temperature coefficient at a particular temperature T_1.

4.3 Rotor Losses

The eddy currents are mainly induced in the PMs, which are highly conductive, and also in the rotor steel. The major causes of eddy currents can be categorized in [6] [7]:

- No-load rotor eddy current losses caused by the existence of stator slots. Due to slotting the flux density is stronger under the teeth and weaker under the slots. The frequency of the induced current is equal to the slot frequency of the machine.
- On-load rotor eddy current losses induced by the major MMF winding harmonics (by the time harmonics of the phase currents). The estimation of the rotor eddy current losses is particularly important in this case, Excessive heat may result in the demagnetization of the magnets and possibly rotor destruction.
- On load rotor eddy current losses induced by the time harmonics of the phase current.

Eddy current losses in the magnets and the rotor steel are calculated using FE methods, includes the use of MAXWELL FE software.

The eddy current loss problem in a magnet may be explained with the use of Fig. 2.12 considering the magnet cube with length l_{pm}, pole pitch τ, and thickness h_{pm}. The eddy current path (c) created by the existence of the time varying flux density B in z-direction is shown. The eddy current problem can be solved one-dimensionally by writing Maxwell Equations.

$$\Delta \times \vec{E} = \frac{\partial \vec{B}}{\partial t} \tag{2.79}$$

$$\Delta \times \vec{H} = \vec{J} \tag{2.80}$$

$$\vec{J} = \sigma \vec{H} \tag{2.81}$$

Integrating both sides of equation (2.79) and using Stokes theorem

$$\oint_c \vec{E}.\vec{dl} = \int_s \left(\nabla \times \vec{E}\right).\vec{ds} \tag{2.82}$$

Yields

$$\oint_c \vec{E}.\vec{dl} = \frac{\partial}{\partial t}\int_s \vec{B}.\vec{ds} \tag{2.83}$$

With the use of the electrical power equation

$$P = \int_V \sigma \vec{E^2} dV = \int_V \frac{\vec{J^2}}{\sigma} dV \tag{2.84}$$

And considering the time average (over a time period T) of the power, the power loss equation for the magnet cube shown in Fig.2.12 becomes

$$P = \frac{1}{T}\int_0^T \iiint \frac{\overrightarrow{J^2(x,t)}}{\sigma} dxdydzdt \tag{2.85}$$

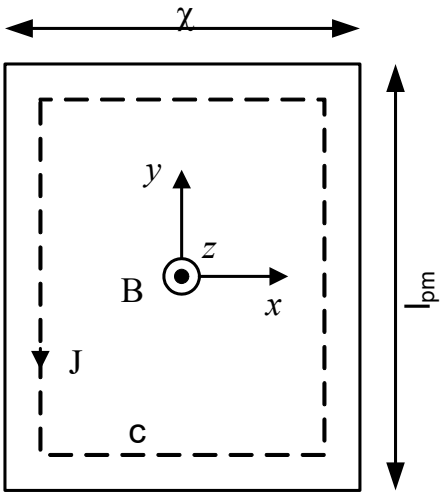

Fig. 2.12: Eddy courant in magnet cub.

Using Equations .2.81 and 2.83, and considering the integral path shown in Fig.2.12, the surface current density can be related to the time-varying flux density of the magnet as

$$J(x) = x\sigma \frac{dB(t)}{dt} \tag{2.86}$$

It should be noted that the end effects are doesn't exist in our machine A-TFPMs which means that the current density ***J*** has only y-axis component (where J(-x)=J(x)), and the flux density is one dimensional (z) and homogeneous. In this manner the eddy current loss can be calculated from the FE solutions.

The integral equation 2.85 can be simplified as

$$\begin{aligned} P &= \frac{1}{T}\int_0^T \iiint \sigma x^2 \left(\frac{dB(t)}{dt}\right)^2 dxdydzdt \\ &= \frac{1}{T}\int_0^T \iiint \sigma x^2 \left(-\frac{B}{\sqrt{2}}\omega \sin(\omega t)\right)^2 dxdydzdt \end{aligned} \tag{2.87}$$

Where ***ω*** is the angular frequency of the eddy currents. The integral equation results in

$$P = \frac{\sigma}{48} l_{pm} h_{pm} \tau^3 B^3 \omega^2 \tag{2.88}$$

For the power loss calculation explained above the skin depth in the magnet for the relevant harmonic frequency

$$\delta = \frac{1}{\sqrt{\pi f \mu \sigma}} \tag{2.89}$$

4.4 Mechanical Rotational Losses

The mechanical rotational losses considered are the friction loss in the bearing and the windage loss from the rotating rotor disc. According to the reference [8], the rotor windage losses can be estimated using Equation 2.90 for air cooling.

$$\begin{aligned} P_{mec} &= P_{win} + P_{fri} \\ P_{win} &= 0.5 c_f \rho_{air} n^3 \left(R_{out}^5 - R_{shaft}^5\right) \end{aligned} \tag{2.90}$$

Here c_f is the coefficient of drag for turbulent flow is given by

$$c_f = \frac{2.87}{\sqrt{R_e}}$$

In the above equation, R_e is the Reynolds number for a rotating disc given by

$$R_e = \frac{n \rho_{air} R_{out}^2}{\eta_{air}}$$

Where $\boldsymbol{\rho_{air}}$: air density at $1atm$ and $20°C$ ($1.2\ kg/m^3$), $\boldsymbol{\eta_{air}}$: dynamic viscosity of air a $1atm$ and $20°C$ ($1.8\text{x}10^{-5}Pas$), n: mechanical rotational speed in rad/s and $\boldsymbol{R_{shaft}}$ radius of the shaft.

The friction loss in a small bearing can be roughly estimated as given below [9].

$$P_{fri} = 0.03k_{fb}\left(RotorMass + ShaftMass\right)\frac{n}{\pi} \tag{2.91}$$

Where k_{fb}=1 to 3 m^2/s^2 for bearings and the masses are given in kg.

The bearing loss calculation tools from the bearing manufacturer can provide more accurate loss estimation. In addition, the bearing loss depends on the axial and radial loads on the bearing. The large axial force between the rotor and stator results in a large axial loading on the bearing and hence higher bearing loss. On the other hand, the radial component depends on the weight of the rotor. Therefore, the bearing should be chosen carefully in A-TFPMS machine design so that they will be able to withstand both the required axial and radial loading with acceptable bearing losses.

4.5 Efficiency

The total power losses of A-TFPMs machine are

$$\begin{aligned} P_{loss} &= P_{fe} + P_{cu} + P_{ro} + P_{mec} \\ &= P_{efe} + P_{hfe} + P_{exc} + P_{cu} + P_{ro} + P_{win} + P_{fri} \end{aligned} \tag{2.92}$$

The output power for generating mode is

$$P_{out} = P_{elm} - P_{loss} \tag{2.93}$$

The efficiency is

$$\eta = \frac{P_{elm} - P_{loss}}{P_{elm}} \tag{2.94}$$

5. Mechanical Design Features

In the mechanical design of an A-TFPMs synchronous machine, obtaining a uniform air gap between the rotor disc and the stator is important. Therefore, the methods of fixing the rotor discs onto the shaft and the stator onto the frame are very important. Improper methods of fixing, or misalignment in the assembling of the stator and rotor will cause a non uniform air gap, vibration, noise, torque pulsation and deterioration of electrical performance.

To summarize, attention should be paid to the following aspects of the mechanical design:

- ✓ **Shaft**.
  - The load torque, the first critical speed and the shaft dynamics should be taken into account in the shaft design.
- ✓ **Rotor**.
  - The deflection of the rotor disc due to the strong magnetic attraction force,
  - The means of mounting and securing the magnets on the rotor discs to counteract the strong centrifugal force,
  - The balancing of the rotor discs.
- ✓ **Stator**.
  - The strength and rigidity of the resin reinforced stator and frame,
  - The positioning and spacing of the stator core to ensure perfect symmetry.
- ✓ **Cooling**.
  - For air cooled A-TFPMs machines, the air inlet and air flow paths through the machine should be carefully designed in order to ensure a better mass flow rate and therefore better cooling.
- ✓ **Assembly**.
  - An effective tool to facilitate the assembling and dismantling of the machine for maintenance.

5.1 Mechanical Strength Analysis

The deflection of the rotor discs due to the strong magnetic pull may have the following undesirable effects on the operation and condition of A-TFPMs machines: closing the running clearance (air-gap) between the rotor disc and the stator; loose or broken PMs.

The attraction force between the PMs Rotor and the stator is

$$F_z = \frac{1}{2}\frac{B^2}{\mu_0} A_{PM} \tag{2.95}$$

The magnetic pressure is

$$p_Z = \frac{F_z}{A_{PM}} \tag{2.96}$$

Where the active area of PM is

$$A_{PM} = \alpha \frac{\pi}{4}\left(D_{out}^2 - D_{in}^2\right) \tag{2.97}$$

The backing steel disk thickness is

$$h_r = \frac{m_r}{2\rho_{Fe}\pi\left(D_{out}^2 - D_{in}^2\right)/4} \tag{2.98}$$

6. Conclusion

This chapter describes the design equations of an A-TFPMS. Thos equations development led us to dimension through a program developed in MATLAB, the geometric, electrical and magnetic parameters this allowed us to determine the total mass, the losses and the efficiency of the designed machines. The program developed of this dimensioning uses the design data (voltage, power, …) and use the demagnetization curve to calculate the operating point, and try to developed the model of this machine and calculating different machine parameters such leakage and armature reaction reactance to use them during the control of this machine.

Moreover, the program developed is a great tool. It automatically and quickly performs the calculations and generates variants of prototypes according to the adopted criteria and the constraints of the specifications.

The prediction of all losses in this machine is very imported; firstly we use Bertotti equation for calculating the core losses, this formula is easy for implementation in FEA program. Secondly the copper losses amount in this machine are smallest than another machines type because no end winding copper losses in A-TFPMS machine. Thirdly during the calculation of the rotor losses we take only the back iron and PM eddy current losses caused by the stator slots. the last one losses are calculated is mechanical rotational losses created by the friction bearing and the windage, those losses to validate their impact in our design we should use CFD simulation as next work. The mechanical design features it's the last point should be treated before building the first prototype start, the mechanical simulation is agreed.

Thus, all geometric dimensions, electrical parameters and magnetic characteristics are found in this chapter, we will try in the next chapter to introduce them in FEA simulation to validate our design procedure.

Bibliography -2-

[1] J. F. Gieras, M. Wing. "Permanent Magnet Motor Technology Design and Applications". Marcel Dekker, New York, 2002.

[2] W. Tsai, "A study on core losses of non oriented electrical steel lamination under sinusoidal, non-sinusoidal and PWM voltage supplies", TENCON 2007, IEEE.

[3] J. F. Gieras, R.-J. Wang, and M. J. Kamper. "Axial Flux Permanent Magnet Brushless Machines", Kluwer Academic Publishers, 2005.

[4] A. Krings, J. Soulard, "Overview and comparison of iron loss models for electrical machines", Journal of Electrical Engineering, vol. 1, no. 3, pp. 162–169, Sept. 2010.

[5] J.L.F. Van der Veen, L.J.J. Offringa, and J.A. Vandenput. "Minimizing Rotor Losses in High-Speed High-Power Permanent-Magnet Synchronous Generators with Rectifier Load". IEE Proc. Elec. Power Appl., 144(5):331-337, Sept. 1997.

[6] F. Sahin. "Design and development of a high-speed axial-flux permanent-magnet machine". Doctoral thesis. Eindhoven. 2001.

[7] J. Gynselinck, L. Vandevelde, and J. Melkebeek. "Calculation of eddy currents and associated losses in electrical steel laminations". IEEE Trans. on Magnetics, 35(3):1191—1195, May 1999.

[8] A. B. Nachouane; A. Abdelli; G. Friedrich; and S. Vivier. "Estimation of windage losses inside very narrow air gaps of high speed electrical machines without an internal ventilation using CFD methods". 2016 XXII International Conference on Electrical Machines (ICEM) IEEE Conf. Pub.. Pages: 2704-2710. 2016.

[9] http://www.skf.com. Bearing friction, power loss and starting torque.

Chapter Three

3D-FEA and Analytical Modeling

Chapter Three

3D-FEA and Analytical Modeling

1. Introduction

The finite element method (FEM) has proved to be particularly flexible, reliable and effective in the analysis and synthesis of power-frequency electromagnetic and electromechanical devices. Even in the hands of non specialists, modern FEM packages are user friendly and allow for calculating the electromagnetic field distribution and integral parameters without detailed knowledge of applied mathematics [1].

The FEM can analyze PM circuits of any shape and material. There is no need to calculate reluctances, leakage factors or the operating point on the recoil line. The PM demagnetization curve is input into the finite element program which can calculate the variation of the magnetic flux density throughout the PM system. An important advantage of finite element analysis over the analytical approach to PM motors is the inherent ability to calculate accurately armature reaction effects, inductances and the electromagnetic torque variation with rotor position (cogging torque).

This chapter deals with two, three dimensional static and dynamic finite element analyses of a transverse flux permanents magnets synchronous machine, at no-load and load conditions. At first, dimensions of the magnetic circuit are analytically computed and then inserted into FEA ANSYS MAXWELL software.

Machine employing two A-TFPMSM topologies are evaluated: the simple side topology (three phase for one side) and that utilizing multi side (one phase for one side). The calculations are reduced to a geometry containing one pole pair with a quasi U-shaped stator core and a slot. The flux linked to the winding obtained in the FEM simulations is compared with the flux calculated analytically. The pole-to-pole flux leakage in the topologies with the various pole length combinations is estimated.

For the design of fully 3-D machines, accurate models of the electromagnetic fields are required. The electromagnetic field expressions can be derived from Maxwell's equations.

2. Maxwell's Equations

Electric and magnetic fields are the foundation of the operation of electromagnetic systems. These fields and their interaction are described with a set of four Maxwell equations **[2]**. These equations are in differential form given by

Ampère's law: $$\nabla \times \vec{H} = \vec{J} + \frac{\partial \vec{D}}{\partial t} \quad (3.1)$$

Gauss' law for magnetism: $$\nabla \cdot \vec{B} = 0 \quad (3.2)$$

Faraday's law of induction: $$\nabla \times \vec{E} = -\frac{\partial \vec{B}}{\partial t} \quad (3.3)$$

Gauss' flux theorem: $$\nabla \cdot \vec{D} = \rho \quad (3.4)$$

The magnetic field strength is represented by the vector ***H*** [A/m], the electrical field strength by ***E*** [V/m], the magnetic flux density by ***B*** [T] and the electric flux density by ***D*** [C/mm^2]. These fields are dependent on time ***t*** [s] and space (*x*, *y*, *z*) [m]. The current density is given by ***J*** [A/m^2] and the electric charge density by ***ρ*** [C/m^3].

However, this set of field equations is not complete. In order to solve the equations, three additional equations, describing the material properties, should be considered.

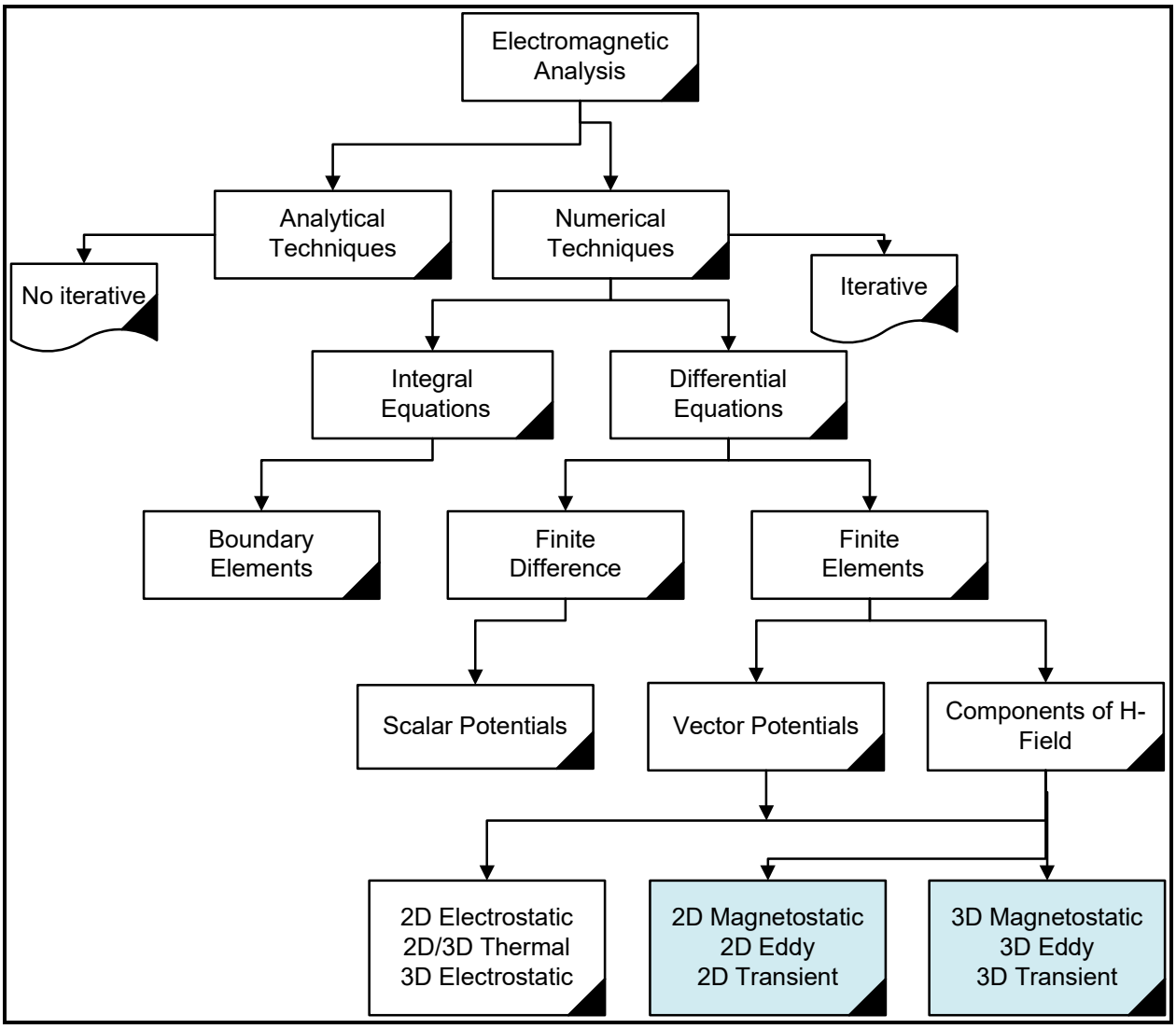

Fig.3.1: Different methods of electromagnetic analysis.

These provide constitutive relations which complete the set of equations.

$$\vec{B} = \mu_0 \left(\vec{H} + \vec{M} \right) \tag{3.5}$$

$$\vec{D} = \varepsilon_0 \vec{E} + \vec{P} \tag{3.6}$$

$$\vec{J} = \sigma \vec{E} \tag{3.7}$$

Here, $\boldsymbol{\mu_0}=4\pi\times10^{-7}$ [H/m] and $\boldsymbol{\varepsilon_0}=8.854\times10^{-12}$ [F/m] are the natural permeability and permittivity constant of free space, respectively. The magnetization of the material is given by $\boldsymbol{M}$ [A/m] representing the net magnetic dipole moment per unit volume, whereas the polarization is given by $\boldsymbol{P}$ [C/m^2] representing the

electric dipole moment per unit volume. Further, the electric conductivity of the material is given by $\boldsymbol{\sigma}$ [S/m].

3. Electromagnetic Analyses Methods

The Finite Element Method is one of many accepted methods of numerically solving complicated fields where analytically solutions are not sufficient. Below is a chart displaying different methods of electromagnetic analysis (Fig. 3.1), each method with its own strengths and weaknesses. Finite elements have proven to be very robust for general electromagnetic analysis. Finite element refers to the method from which the solution is numerically obtained from an arbitrary geometry. The arbitrary, complicated geometry is broken down into simple pieces called finite elements.

3.1 Magnetostatic 2D

To reduce the complexity of the electromagnetic field description, the magnetostatic set of Maxwell's equations may be considered. The justification of this approach is undertaken by estimating the error in the obtained magnetic field solution. The approximation is valid if the error in the obtained magnetic field solution is small compared to the original field solution. In order to consider the magnetostatic set of Maxwell's equations, the electric displacement current should be neglected.

$$\nabla \cdot \vec{J} = 0 \tag{3.8}$$

$$\nabla \times \vec{H} = \vec{J} \tag{3.9}$$

$$\nabla \cdot \mu_0 \vec{H} = 0 \tag{3.10}$$

in Maxwell 2D The magnetostatic field simulator solves for the magnetic vector potential, $A_x(y,z)$ in equation (3.11), Given $J_x(y,z)$ as an excitation, The magnetostatic field simulator computes the magnetic vector potential at all points in space.

$$J_x(y,z) = \nabla \times \left(\frac{1}{\mu_0 \mu_r} \left(\nabla \times A_x(y,z) \right) \right) \tag{3.11}$$

Where:

$A_x(y,z)$ is the **z** component of the magnetic vector potential.

$J_z(x,y)$ is the DC current density field flowing in the direction of transmission.

μ_0 *and* μ_r are the relative and free space permeability respectively.

In general, both ***J*** and ***A*** are vectors. However, ***J*** is assumed to only have an x-component. A consequence of this is that ***A*** only has a x-component as well. Both quantities can therefore be treated as scalars.

The equation that the magnetostatic field solver computes is derived from Ampere's law equation (3.9), and from Gauss's equation (3.2).

Since $H = \frac{B}{\mu_0 \mu_r}$ then $$\nabla \times \left(\frac{B}{\mu_0 \mu_r} \right) = J \qquad (3.12)$$

We put the potential term $B = \nabla \times A$ in the equation (3.12) we found

$$\nabla \times \left(\frac{1}{\mu_0 \mu_r} B \times A \right) = J \qquad (3.13)$$

The magnetostatic field simulator solves this equation using the finite element method, after $A_x(y,z)$ is computed, the magnetic flux density, ***B***, and the magnetic field, ***H***, can then be computed.

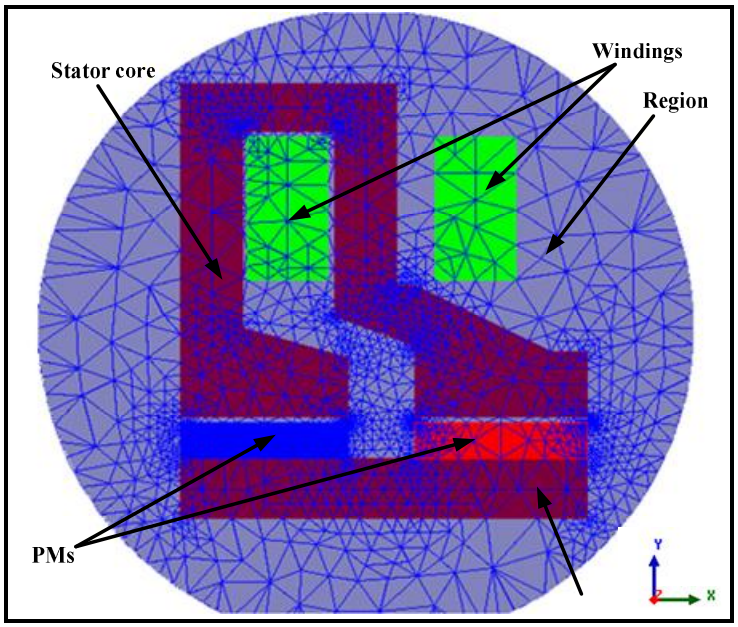

Fig.3.2: Mesh operation using in 2D magnetostatic simulation.

A transverse flux (A-TFPMSM) topology has basically considered a single side structure. Therefore several single side units could be stacked together in such a way that a desirable multistage machine is produced. The performance of one unit determines the performance of the entire machine; simulate one pole-pair model sufficient for finite element analysis.

The model obtained is given in Fig. 3.2 where the different materials are represented: air, ferromagnetic materials, windings and permanent magnets.

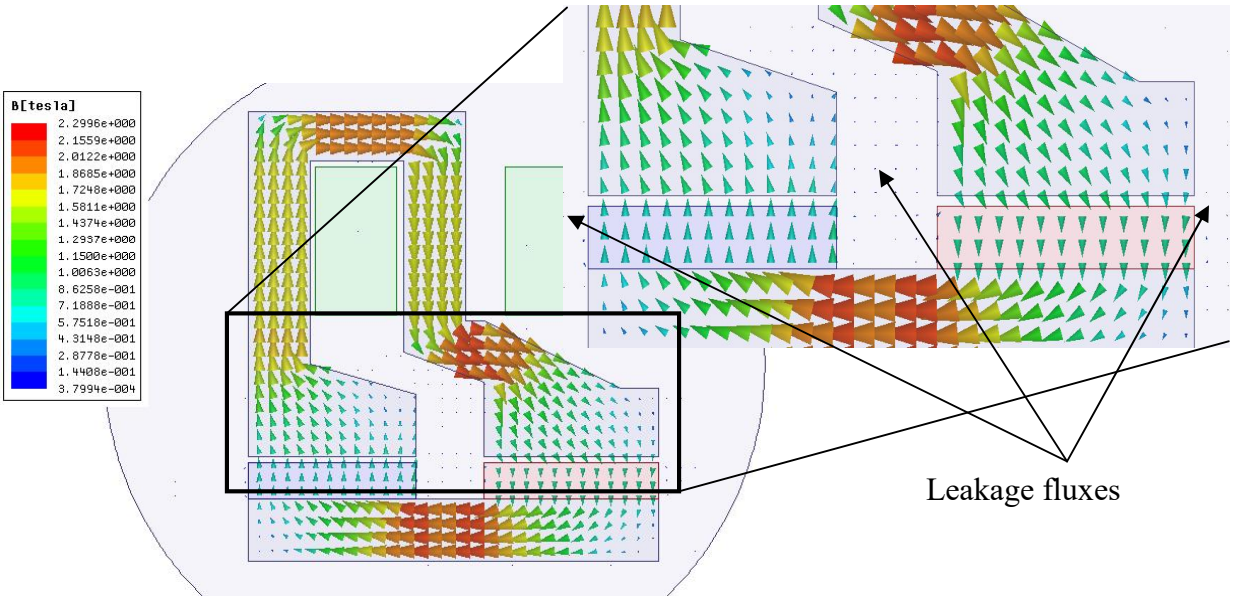

Fig. 3.3: Simulation 2D of one stator core by using ANSYS MAXWELL software.

The dimensions of the magnetic circuit are at first estimated analytically as described in previous chapter. Assuming certain input (machine rating power, rotor speed, etc.) and deciding on the desired performance, the dimensions can be calculated. The assumptions outlined below are made while estimating the dimensions:

• $\boldsymbol{B_{sFe}}$ is limited to 1.6T. The same maximum flux density is allocated in the stator core and rotor yokes, i.e. $B_{sFe} = B_{rFe}$.

• A maximum air-gap flux density created by the magnets $\boldsymbol{B_{av}}$=0.9T is assumed based on the magnetic properties of iron and the magnet material.

The initial dimensions of the basic geometry corresponded to Fig. 3.3 are tabulated in Table 2.1. The dimensions with no particular topology specified are valid for both topologies.

The goal of the static FEM analysis at no-load condition is to analyze the flux and the flux leakage for the given geometry. Thus as shown in Fig. 3.3 there is some area are is saturation case, especially the parts are near of winding, also we have few leakage flux , firstly between the PMs in the same pole, secondly between own core parts and thirdly between the PMs and stator core shoes.

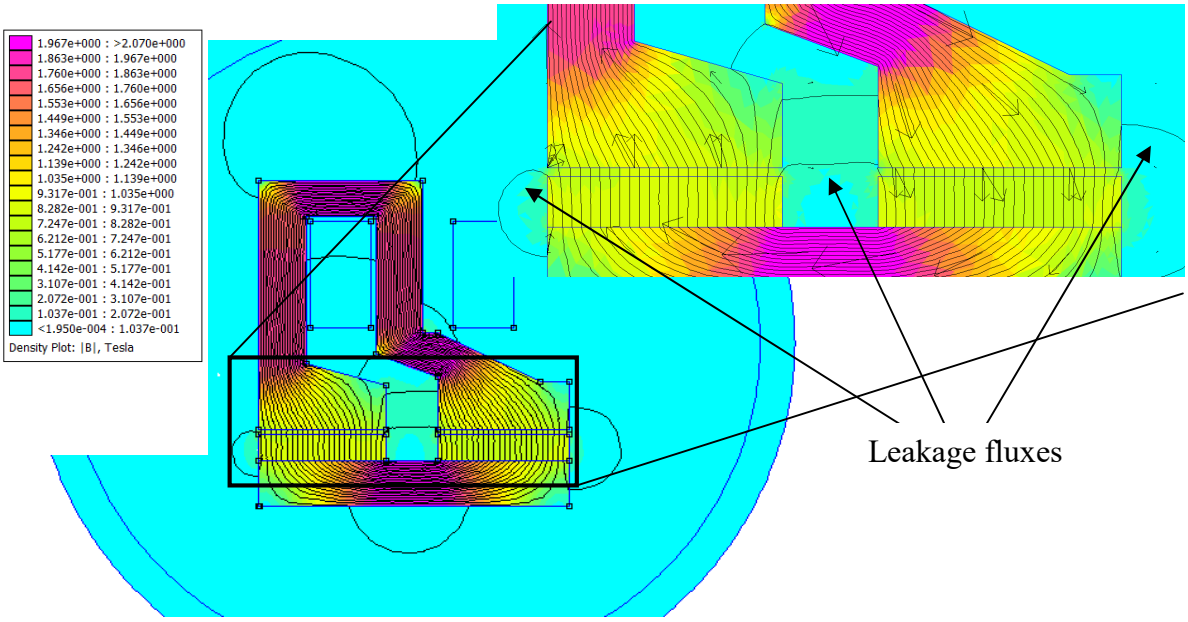

Fig. 3.4: 2D Field distribution of one stator core by using FEMM software.

To validate a 2D-FEM model of ANSYS MAXWELL simulation for the A-TFPM as the complimentary tool in respect to the analytical models the software FEMM 3.0 (Finite Elements Method Magnetics) **[3]** is used. It allows the distribution of the vector potential and the post-processor submits the processing of the data and calculation of interesting physical values, such as flux density

In Fig. 3.4 presented the 2D field distribution of stator core in FEMM environment, it results compared with ANSYS MAXWELL 2D simulation are agreed.

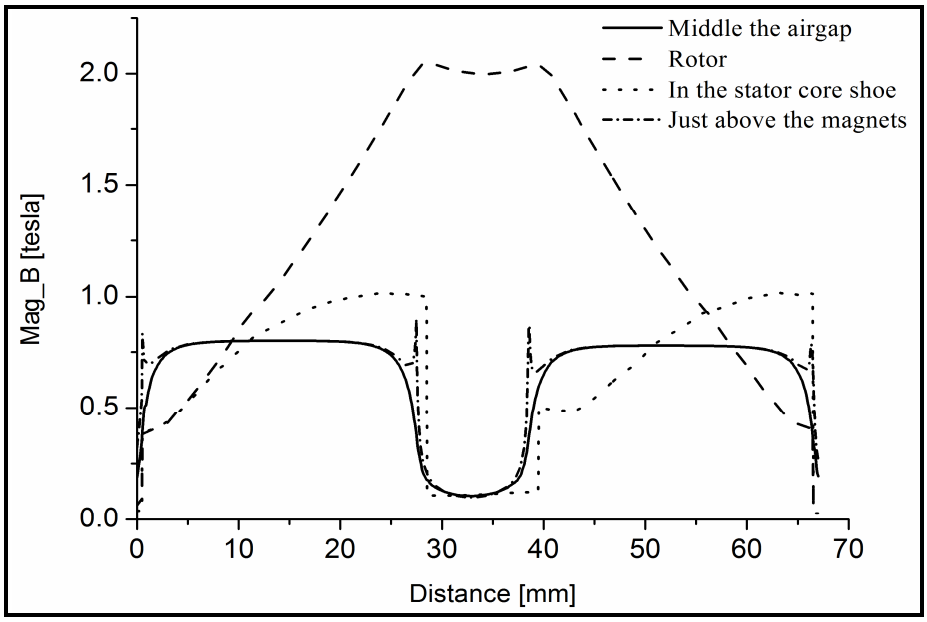

Fig.3.5: Magnetic flux density module in machine parts (ANSYS).

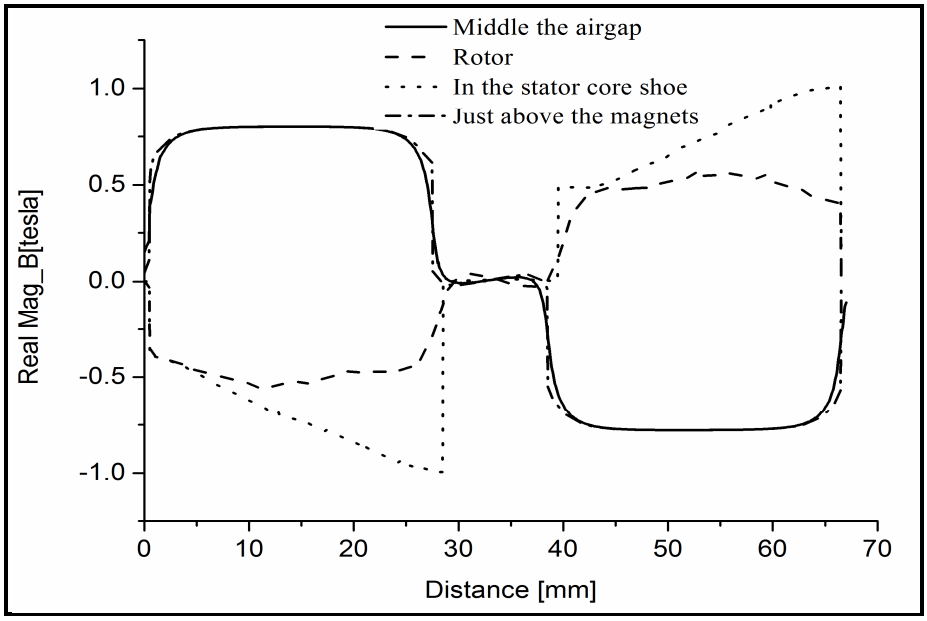

Fig.3.6: Real magnetic flux density in machine parts (ANSYS).

in Fig. 3.5 and Fig. 3.6 are presented the magnetic flux density in many parts of our machine, the first presented the module of flux density and the second presented only the flux density in ***Y*** axis, thus as shown only the rotor flux density has two direction ***X*** and ***Y***.

3.2 Magnetostatic 3D

In a Magnetostatic 3D solution, the magnetic field is produced by DC currents flowing in coils and by permanent magnets. Thus, as far as magnetic material properties are concerned, the distribution of the magnetic field is influenced by the spatial distribution of the permeability. There is no time variation effect, and objects are considered to be stationary.

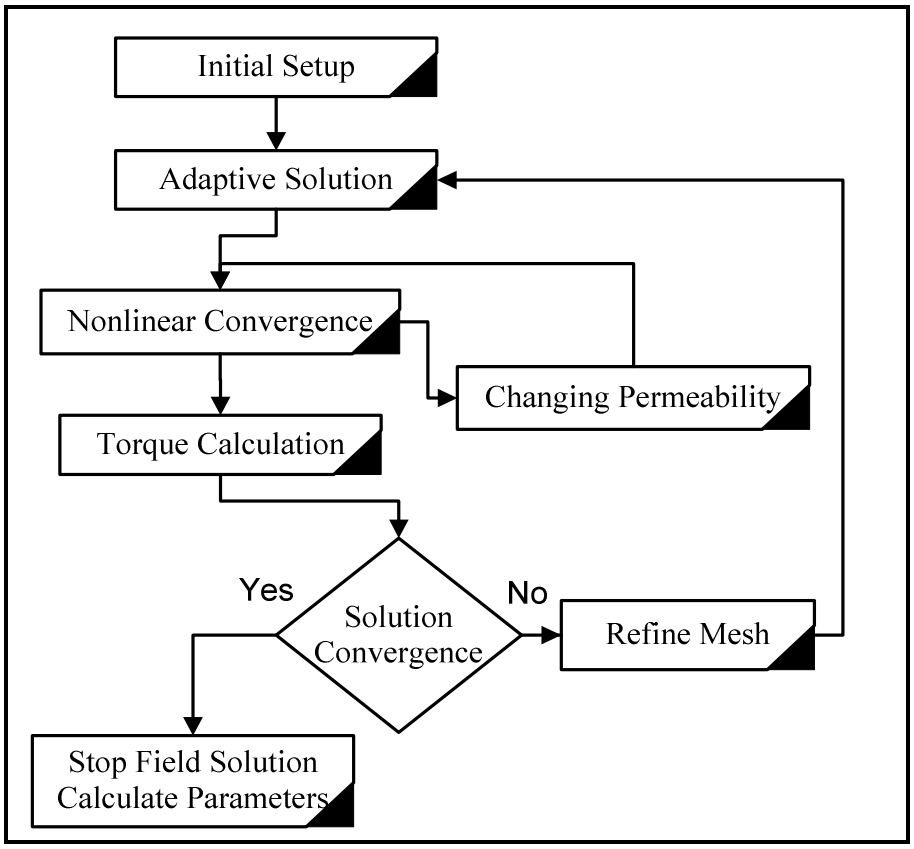

Fig. 3.7: Magnetostatic Solution Process [4].

The principle of operation of the A-TFPMS machine is presented in the previous chapter, demonstrates the existence of two-dimensional flux paths (main flux path of permanent magnets in same pole, plane (*yoz*) (***z*** axis of the machine)) and (second (tangential) flux paths nearby pole). Since the tangential component of the flux is not a secondary phenomenon, a 2D FE modeling of the structure will be incomplete and the implementation of a 3D finite element model is necessary. We propose to present the different steps necessary for the establishment of these models by ANSYS MAXWELL software. The process

solution Maxwell steps through several stages of solution process as shown in diagram Fig. 3.7, we can use in this solution type the nonlinear materials (μ_r varies according to BH curves) in this case the energy is less than the co-energy .

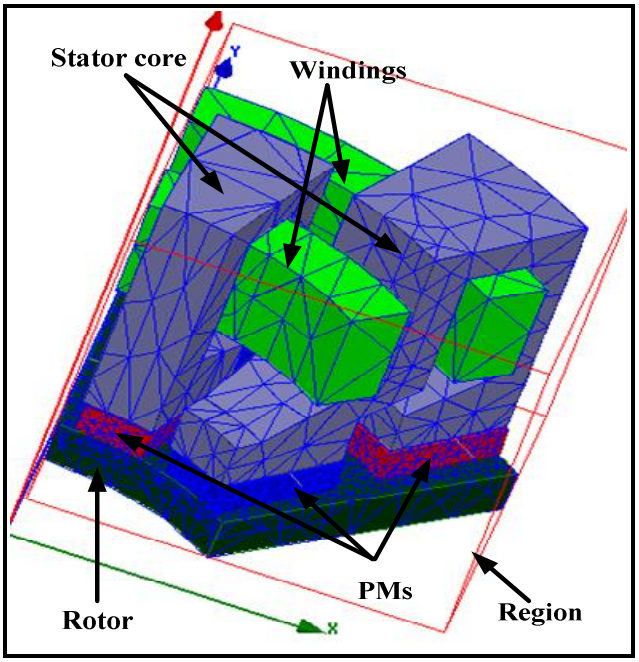

Fig.3.8: Mesh operation using in 3D magneto-static simulation.

Table 3.1: Mesh statistics of transverse-axial flux machine in 3D magnetostatic simulation.

Parts	Num. of triangles	Min edge length	Max edge length	Min Tr. Vol.	Max Tr. Vol.
Rotorin	10339	1.56463	7.35894	0.20275	18.2648
Region	43504	1.38429	36.75	0.04214	1928.11
StatorC_3	11011	2.41807	10.0158	0.50243	47.3968
PMin_5	1948	1.61153	5.64424	0.21833	7.57952
PMin_6	1868	1.75	3.95815	0.24328	6.49844
PMout_5	2975	1.75	5.33639	0.32694	6.43328
PMout_6	2992	1.44377	5.12312	0.17436	7.12386
StatorC_2	15879	1.84362	8.99549	0.25276	46.725
PhaseC	3526	3.02666	10.0467	1.11332	35.2763
PhaseC_1	2587	2.85752	9.69555	0.85566	33.9567
Total mesh elements	96629				

The meshing operation in magnetostatic 3D simulation is adaptive, that mean the number of triangles and his edge length are regenerate for all new solution at the energy of error is converged or number of passes is true, thus the finale mesh are presented in Fig. 3.8 and its statistic in Table 3.1. The variation of stop criterion is represented in Fig. 3.9.

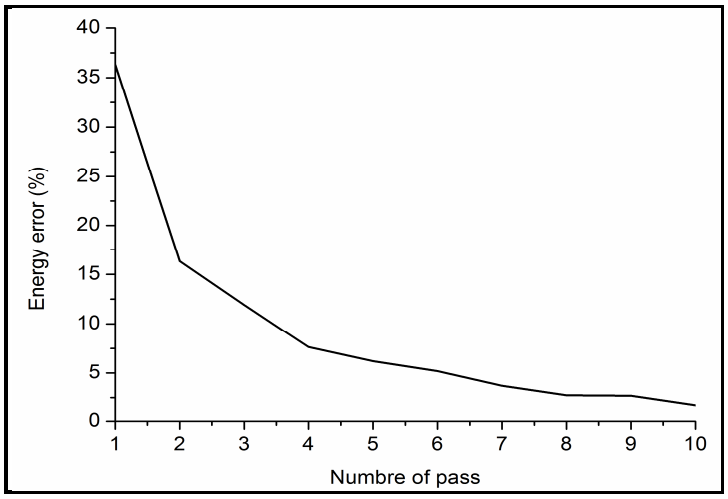

Fig. 3.9: Variation of energy error during the FE simulation.

The Fig. 3.10, Fig.3.11 and Fig.3.12 are represented the distribution of magnetic flux at no-load condition. The Fig.3.10 shown the streamline path of the magnetic induction, there is flux lines in tangential and normal directions, no areas saturations neither in core stator nor in rotor.

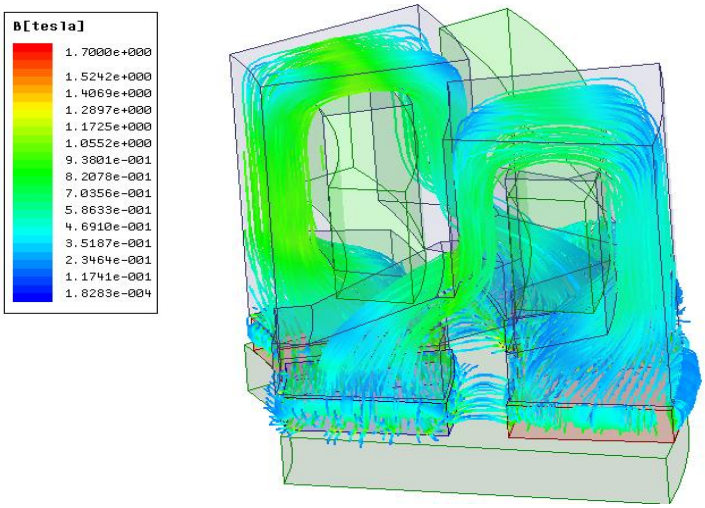

Fig. 3.10: Streamline FE simulation at no-load condition.

The Fig.3.11 give us an clearly image about flux density in different machine parts, as shown the maximum flux density in core stator is 1.05T and 1.17T in rotor. To detect the path of flux density and its orientation, the Fig.3.12 shown the vector of flux density of one pole, the orientation of flux lines are homogeneous.

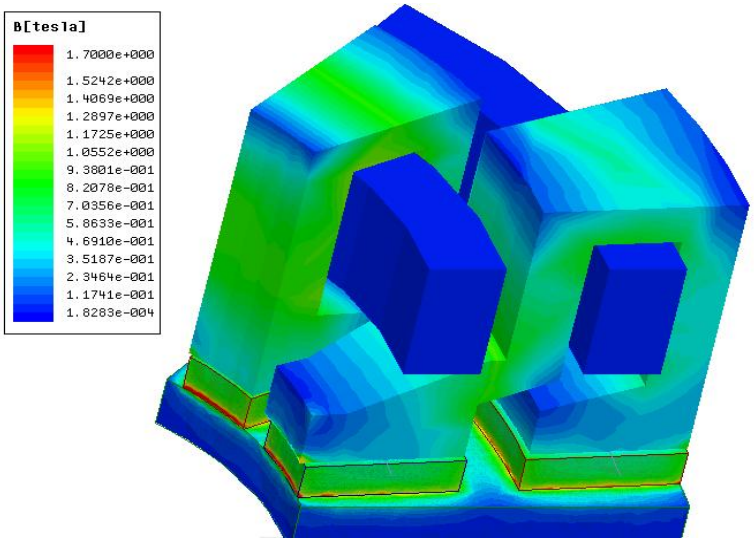

Fig.3.11: Magnetostatic flux density of the transverse-axial flux machine at no-load.

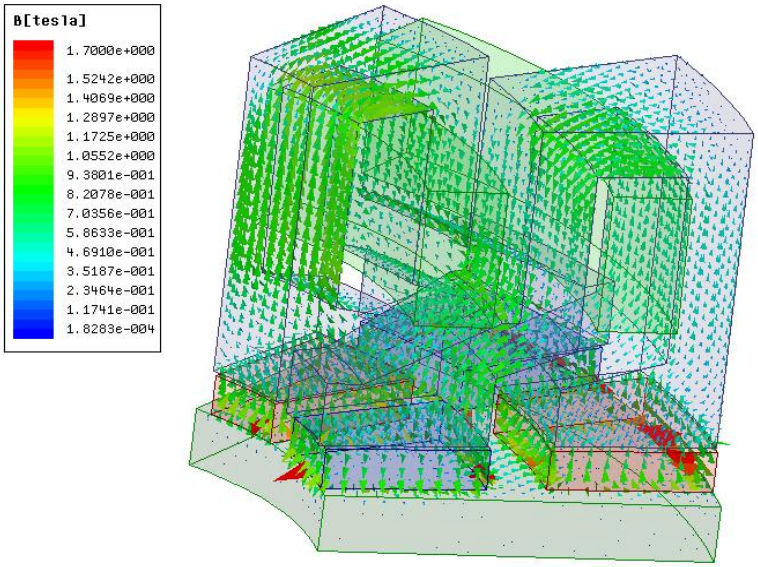

Fig.3.12: Magnetostatic 3D of the transverse-axial flux machine at no-load.

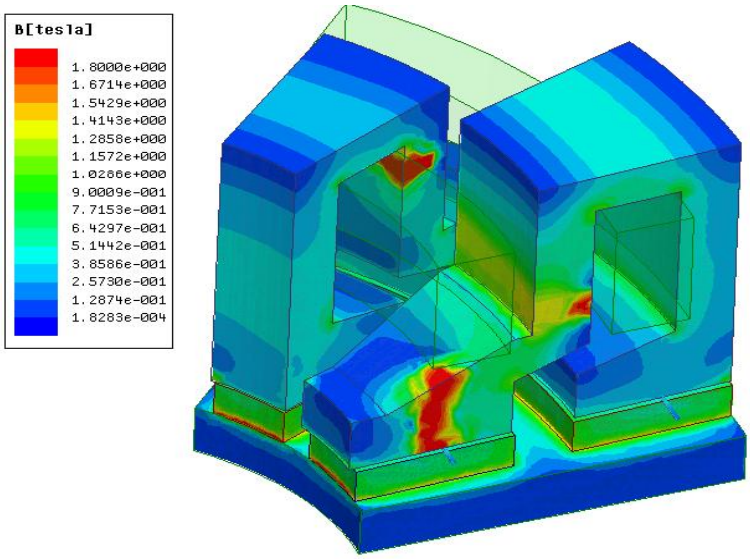

Fig.3.13: Magnetostatic flux density of the transverse-axial flux machine at full-load.

The flux distribution of A-TFPMS machine at load condition is represented in Fig.3.13, Fig.3.14 and Fig.3.15. The flux density is represented in Fig.3.13, the core stator has some area in saturation, and the maximum induction is nearly 1.9T, no saturation in back iron rotor.

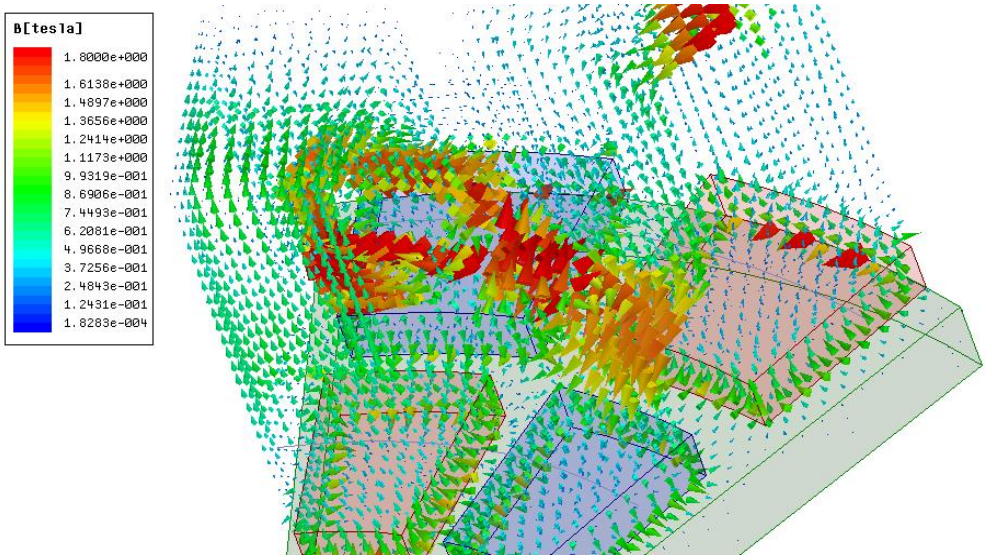

Fig.3.14: Magnetostatic flux density of the transverse-axial flux machine at full-load.

In Fig. 3.14 the flux density is represented as vector, as shown the path of flux lines nearby of winding aren't homogenous, to discover what happen in this area we use streamline function, as shown we have three area in saturation case caused by interaction between the winding flux lines and PMs flux lines, maybe to avoid this problem we can use iron bridge or modified the core stator dimensions.

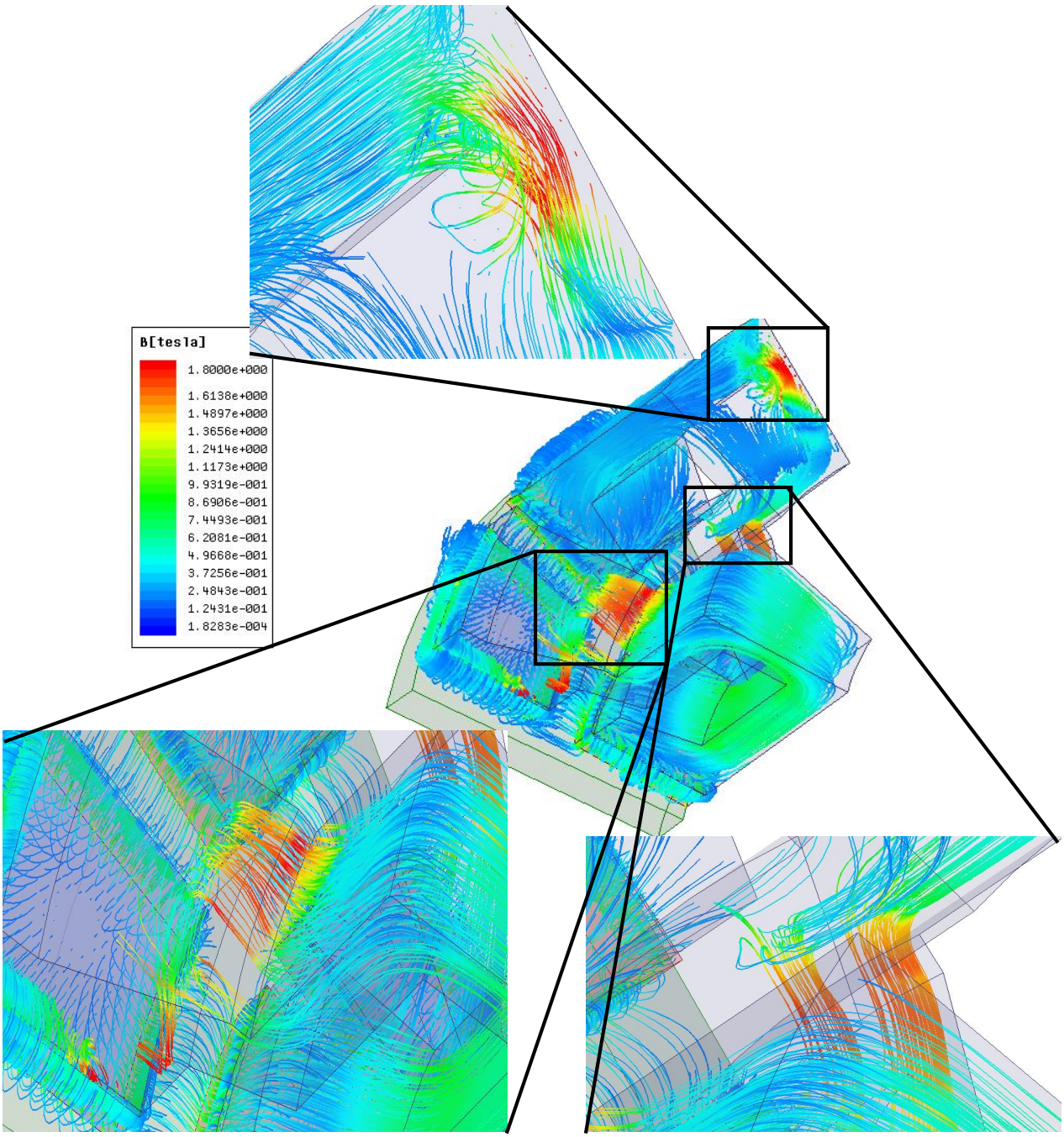

Fig.3.15: Streamline FE simulation at full-load.

The airgap flux density in inner and outer radius are represented in Figs.3.16 (a) and (b) respectively, as shown in first curve the maximum airgap flux density at load and no-load conditions are same value in both positions, in the inner and outer radius airgap flux density curves.

The distance at inner and outer pole in our A-TFPMS machine design aren't equals, thus 3D airgap glux density curve is represented in Fig.3.18.

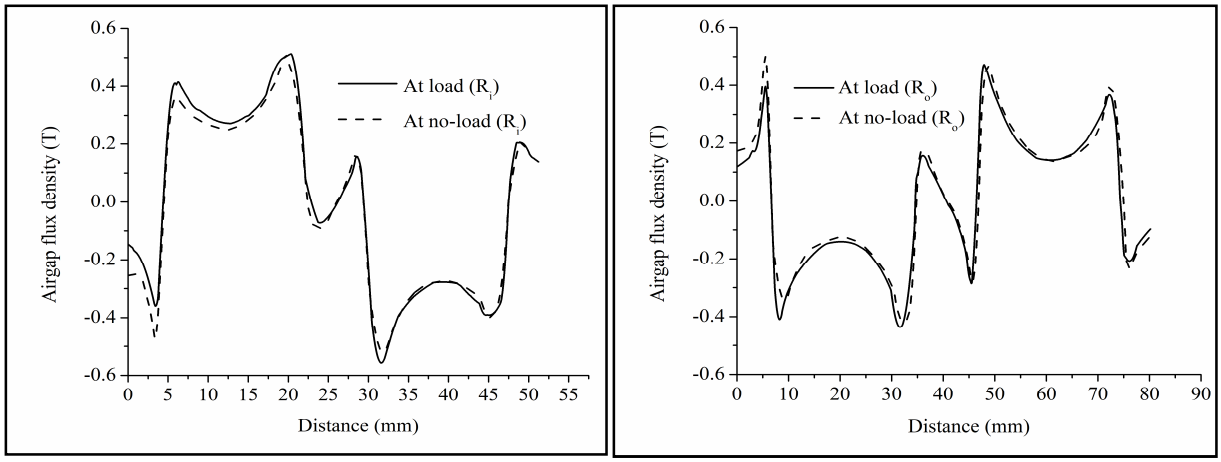

(a) (b)

Fig.3.16: Air-gap flux density at full-load and no-load conditions, (a) inner radius and (b) outer radius.

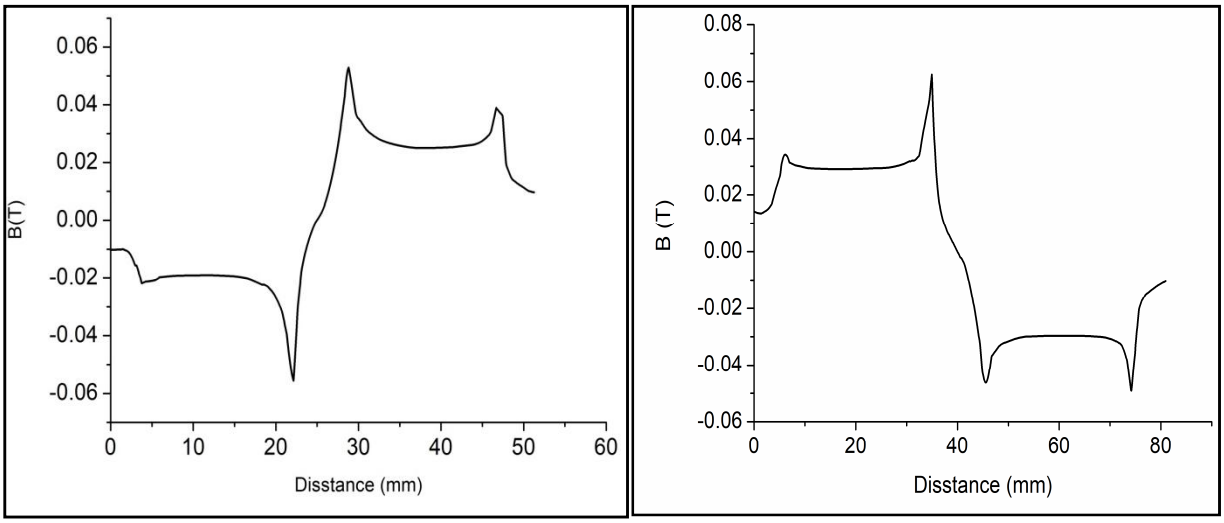

(a) (b)

Fig.3.17: Armature reaction flux density distributions at full-load condition, (a) inner airgap and (b) outer airgap.

The airgap flux density is directly related to the produced torque. The machine is continuously exposed to the magnet flux, where the armature reaction flux is dependent on the amount of stator current. The effect of the armature reaction may be clearly seen. The armature reaction flux plot over the machine and the armature reaction flux density distribution in the inner airgap and outer airgap are shown in Figs. 3.17 (a) and (b) respectively.

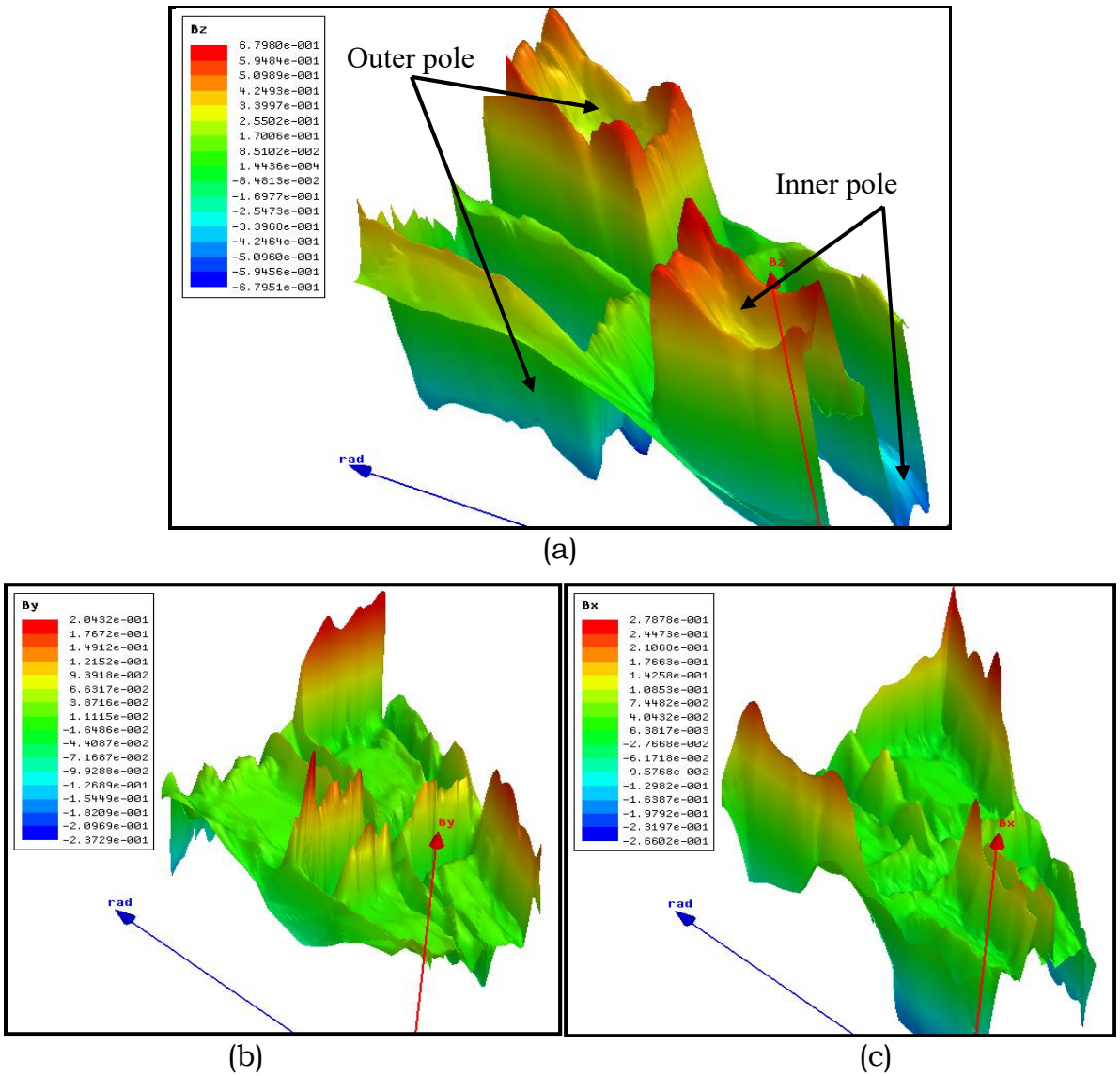

Fig. 3.18: 3D plot of air gap flux induction of one pole. (a) z component, (b) y component and (c) x component.

3.2.1 Magnetostatic Material Properties

In a Magnetostatic simulation, the following parameters may be defined for a material

- **Magnetic Coercivity:** Used to define permanent magnetization of magnetic materials, magnitude and direction specification, the direction specified is ***z***-axis in our machine design.
- **Composition:** can be solid or lamination setting composition to lamination creates an anisotropic magnetization effect.

In magnetostatic simulation the material are used in the machines parts are non lamination steel 1008 and NdFeB permanents magnet

With the following constitutive (material) relationship being also applicable:

$$\vec{B} = \mu_0 \left(\vec{H} + \vec{M} \right) = \mu_0 \mu_r . \vec{H} + \mu_0 . \vec{M} \qquad (3.14)$$

where: $\vec{H}(x,y,z)$, $\vec{B}(x,y,z)$, $\vec{J}(x,y,z)$ and $\vec{M}(x,y,z)$ are the magnetic field strength, the magnetic flux density, the conduction current density and the permanent magnetization respectively.

3.2.2 Boundary Conditions

Natural boundaries very rarely exist in electromagnetic field problems. In most types of applications the electromagnetic field is an infinitely extending space. In this application boundaries are used to simplify the FE model and approximate the magnetic vector potential at node points. Rotary electrical machines have identical pole pitches or sometimes half-pole pitches. Boundaries due to symmetry greatly reduce the size of the FE model; boundary conditions can be classified into three types **[5]**.

3.2.2.1 Dirichlet Boundary Conditions

Dirichlet boundaries force the flux lines to be parallel to the boundary's edge. By using the boundary condition $\vec{A} = 0$, flux lines are constrained to follow the boundary. The outer edge of the stator yoke, for example, could have a Dirichlet boundary of $\vec{A} = 0$. This is a simplification since any leakage flux which would extend beyond the stator's yoke is now neglected. The high relative

permeability of the ferromagnetic yoke would ensure that most of the flux remains inside the yoke and in most motor designs this boundary condition is a reasonable simplification to make.

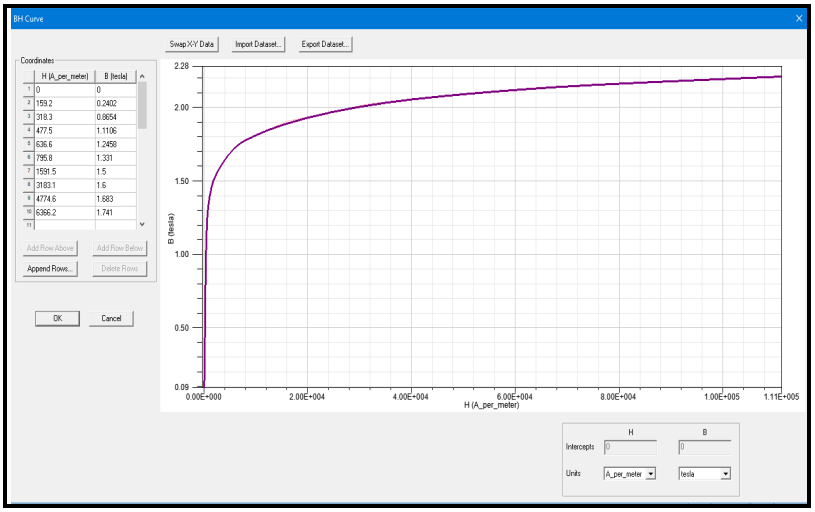

(a)

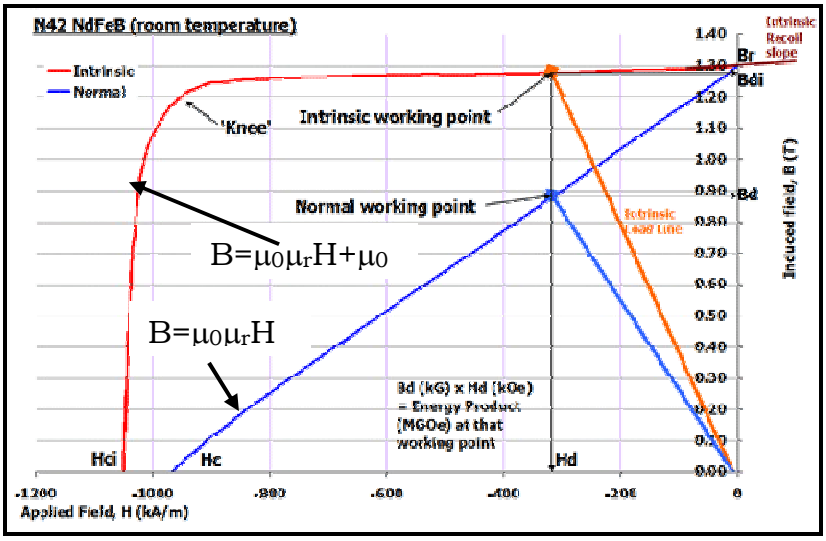

(b)

Fig.3.19: (a) BH curve of stator and rotor material (steel 1008) and (b) demagnetization curve of NdFeB magnet.

3.2.2.2 Neumann Boundary Conditions

Neumann boundary conditions require the normal derivative of the magnetic vector potential be zero. Neumann boundaries are natural boundaries in the

FEM since they do not have to be specified explicitly. Flux lines cross a Neumann boundary orthogonally.

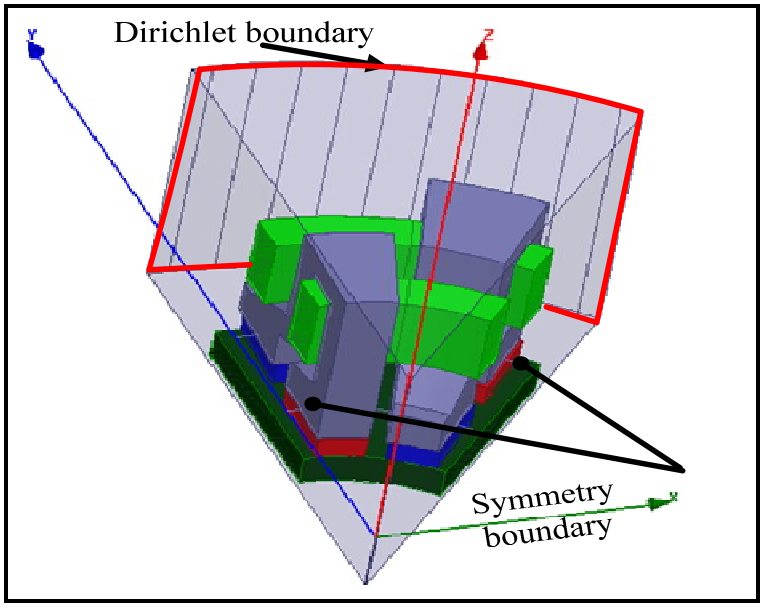

Fig. 3.20: Boundary conditions in 3D magnetostatic simulation.

3.2.2.3 Symmetry Boundary Conditions

In our simulation of one pole of the A-TFPMS machine the field behaves as follows: Odd symmetry (flux tangential) the ***H*** is tangential to the boundary and its normal components are zero. Even Symmetry (flux normal) the ***H*** is normal to the boundary and its tangential components are zero as shown in Fig.3.20.

3.2.3 Mashing Operation in Finite Element Method

The fundamental unit of the FE is a tetrahedron. These elements are constructed together in what is known as the FE mesh. Equilateral tetrahedra work best for the 2nd order quadratic interpolation that is used between nodes. It is good to keep in mind that a relatively uniform, equilateral mesh is often desired. The desired field in each element is approximated with a 2nd order quadratic polynomial:

$$H(x,y,z) = a_0 + a_1 x + a_2 y + a_3 z + a_4 xy + a_5 yz + a_6 xz + a_7 x^2 + a_8 y^2 + a_9 z^2 \qquad (3.15)$$

In order to obtain the basis functions, field quantities are calculated for 10 points in a 3D simulation (nodal values at vertices and on the edges) Fig.3.21.

All other quantities are determined from the field solution in part or in all of the solution space.

The accuracy of the FE solution is dependent on the mesh topology. The mesh is thus an important part of any FE model and attention should be placed on creating it. Essentially, there are two types of mesh generators. The first being an analytical mesh generator that define the problem geometry using large global elements. These global elements are subsequently refined according to the user, usually automatically; this mesh type is used in our 3D magnetostatic analyses. The other type of mesh generator is a synthetic generator where the user designs a mesh region at a node-by-node level and the model is the union of a number of different meshes, this second type we used it in our case only in first A-TFPMS machine simulation to avoid non-convergence the solution.

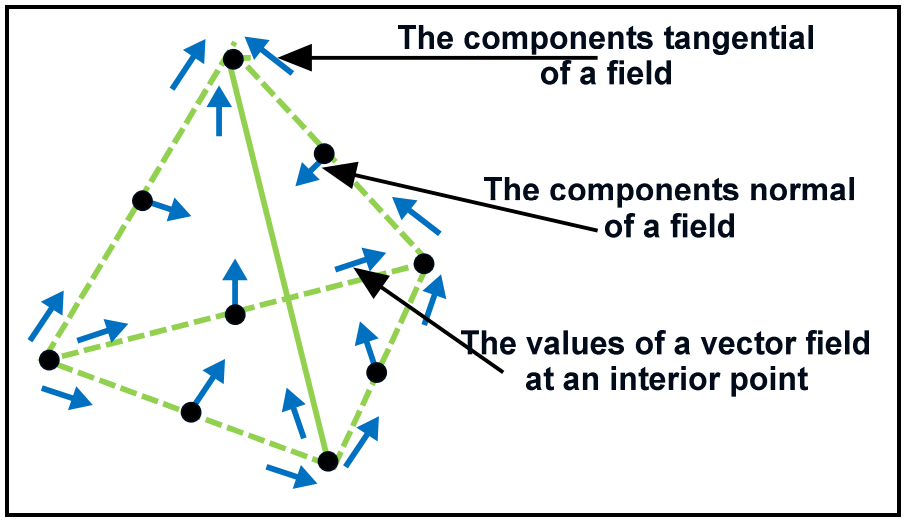

Fig. 3.21: The fundamental unit of the finite element in 3D analysis.

Fully automated mesh generation can only be achieved if the errors which arise from the mesh discretization are taken into account. This is called self-adaptive meshing, and relies on an accurate and reliable method of estimating the discretization errors in the mesh. Modern FE packages that use self-adaptive meshing normally calculate the discretization error estimates from a FE solution. These packages usually create a crude mesh which is solved. Error

estimates are made from this solution and the mesh is refined in the approximate places. This process is repeated until the required level of accuracy is obtained for the model. The error estimates used in the program depend generally on the application, but general FE programs usually calculate their error estimates from the change in flux density across element edges.

There is some fundamental defining equation that provides an error evaluation for the solved fields. In the case of the magnetostatic simulation, this defining equation is the no-monopoles equation, which says:

$$\nabla.\vec{B} = 0 \tag{3.17}$$

When the field solution is returned to this equation, we get an error term:

$$\nabla.\vec{B}_{solution} = err \tag{3.18}$$

The energy produced by these error terms is computed in the entire solution volume. This is then compared with the total energy calculated to produce the percent error energy number.

$$\%.error.energy = \frac{error.energy}{total.energy} \times 100\% \tag{3.19}$$

This number is returned for each adaptive pass along with the total energy, and these two numbers provide some measure of the convergence of the solution. The error energy is presented in Fig. 3.9.

The first simulation was magneto-static finite element analyses, in this type of simulation the calculations of losses, cogging torque and EMF aren't possible, for this reasons the transient simulation is very useful in A-TFPM machine.

3.3 Transient Magnetic Analysis

The quantities for which the transient field simulator solves are the magnetic field, ***H***, and the current distribution, ***J***; the magnetic flux density, ***B***, is automatically calculated from the H-field. Derived quantities such as forces, torques, speed, position, winding flux linkage, and winding induced voltage may be calculated from these basic field quantities.

In the magnetic transient, motion is allowed and nonlinear BH material dependencies are also allowed. The support of voltage excitations for the windings has as consequence the fact that the winding currents are unknown and thus the formulation has to be modified slightly to allow Maxwell to account for source fields due to unknown currents in voltage-driven solid conductors. The rotational type of motion a simpler formulation is obtained by using a cylindrical coordinate system with the z axis aligned with the actual rotation axis.

3.3.1. Rotational Movement Simulation in FEA

In transient simulations, taking into account rotor motion is an essential aspect of dynamic machine modeling. If the mesh of the rotor and the stator are homogeneous, a distortion of the mesh of the gap appears. When the distortion becomes too large, convergence problems are noted. Moreover, the ANSYS MAXWELL software does not allow the movement of one part of a homogeneous mesh compared to another (Fig. 3.23).

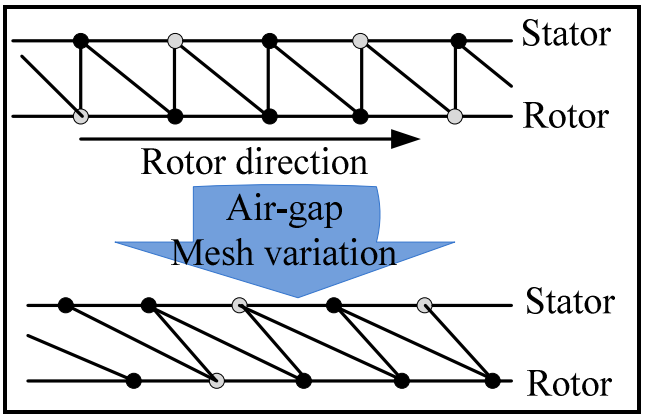

Fig. 3.23: Air-gap mesh variation during stator/rotor movement.

This involves the preparation of two distinct meshes: one for the rotor and its gap; the other for the stator and its gap. The two domains are then combined at their common border. There are two approaches to achieving this goal: (i) the non-meshed gap method, (ii) the mesh gap method. In this work, the mesh gap method has been adopted.

We find two main techniques using the method of the mesh air-gap: the technique of the sliding surface and the technique of the motion band, in our case the domain of the rotor, and the stator having distinct coordinate systems and one of which is in motion and the other static (Fig.3.24). The technique are used by the author of this thesis in ANSYS MAXWELL is the technique of the sliding band, the meshes of the rotor and the stator are generating separately.

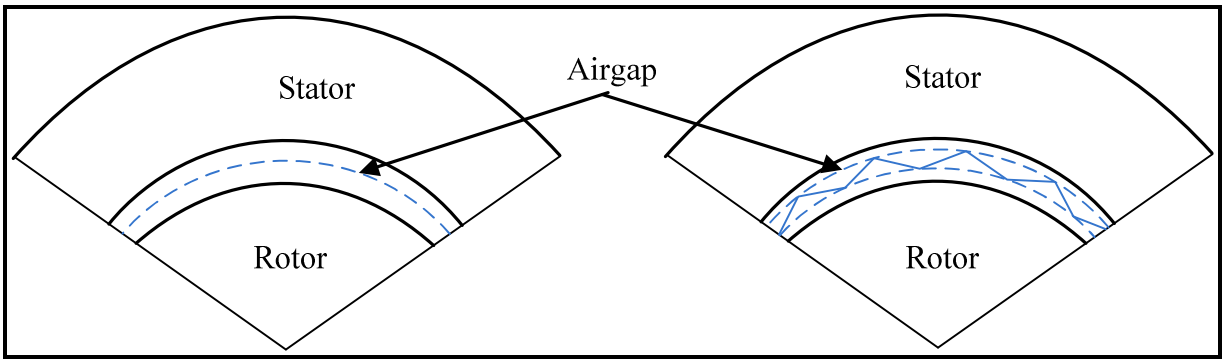

Fig. 3.24: The mesh air-gap techniques, (a) sliding surface (b) motion band.

All types of motion applications require a *band* object that must contain the moving parts. If there are multiple moving objects, all of the moving parts must be included in one all-inclusive object; this is because they all must be moving as one rigid body, with single force acting on the assembly.

For problems involving rotational type of motion a "sliding band" type of approach is followed and thus no re-meshing is done during the simulation.

The following equations (3.1), (3.2) and (3.3) are relevant for transient (low frequency) applications; by arranging them we find the next equation:

$$\nabla \times \frac{1}{\sigma} \nabla \times H + \frac{\partial B}{\partial t} = 0 \qquad (3.23)$$

The final result is a formulation where vector fields are represented by first order edge elements and scalar fields are represented by second order nodal unknowns.

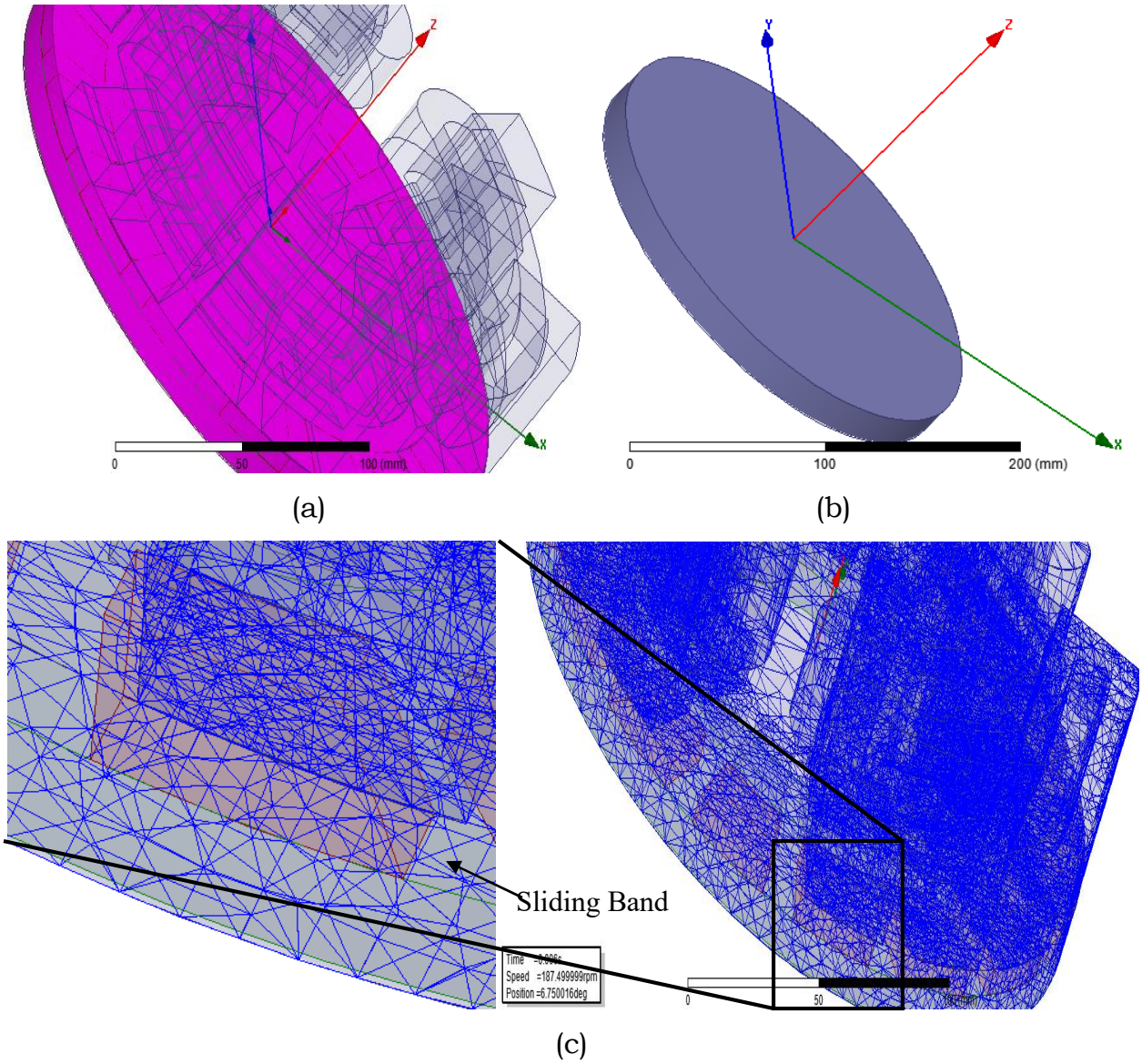

Fig. 3.25: (a) Rotor and stator assembly with band object in between, (b) Band object and (c). Sliding Band mesh.

Field equations are coupled with circuit equations for both solid and stranded conductors because, in the case of applied voltage supplies, the currents are unknown.

3.3.2. Calculating the Torques in FEA

The calculation of torques using the FEM is one of the most important functions of this method. In electrical machine problems four methods of

calculating forces or torques are used: the *Maxwell stress tensor,* the *co-energy method,* the *Lorentz force equation* ($\vec{J}\times\vec{B}$**)**, and the *rate of change of field energy method* (**(**$\vec{B}\partial B/\partial x$ *).T*he most frequently used methods are the Maxwell stress tensor and co-energy methods.

In this case the electromagnetic force/torque is calculated using the virtual work approach (*co-energy method*).

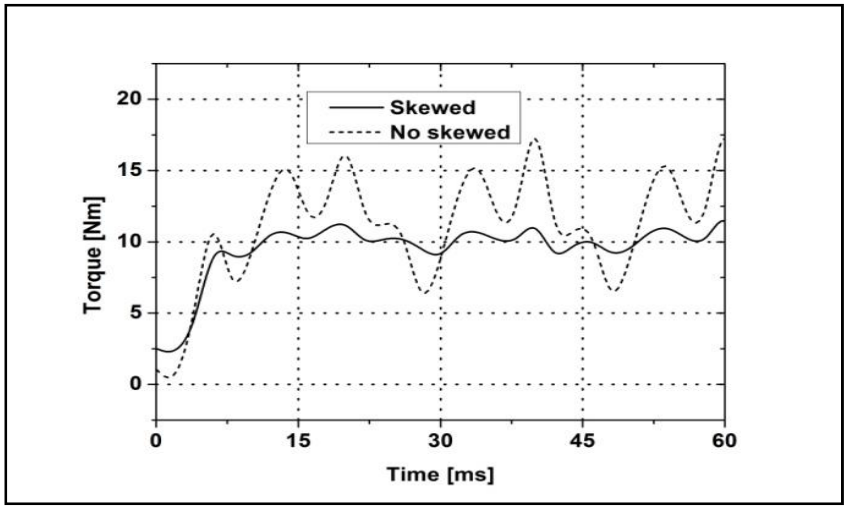

Fig. 3.26: Torque generated from FEA transient simulation.

The force or torque is calculated as the derivative of the stored magnetic co-energy ***W'*** with respect to a small displacement. The finite difference approximation approximates the derivative of co-energy by the change in co-energy for a displacement ***x***, the component of instantaneous force ***F***, in the direction of the displacement ***x*** is **[6]**.

$$F_x = \frac{dW'}{dx} \approx \frac{\Delta W'}{\Delta x} \tag{3.24}$$

For an instantaneous torque ***T*** with a small angular rotation displacement ***θ*** (mechanical angle)

$$T = \frac{dW'}{d\theta} \approx \frac{\Delta W'}{\Delta \theta} \tag{3.25}$$

The instantaneous torque can also be expressed in the following form

$$T = \left.\frac{\partial W'(i,\theta)}{\partial \theta}\right|_{i=cinst} \approx -\left.\frac{\Delta W(\Phi,\theta)}{\Delta \theta}\right|_{\Phi=const} \quad (3.26)$$

Where $\boldsymbol{W}$, $\boldsymbol{\phi}$ and $\boldsymbol{i}$ are the magnetic energy, flux linkage vector and current vector, respectively.

The torque equation developed in the previous section is used to perform the analysis of the machine torque. The validation of the model is made on the basis of the results obtained from the 3-D transient FEM simulation. The waveform of the generator torque is shown in Fig. 3.26. This waveform has significant oscillations. The cause is the cogging torque generated by the air-gap reluctance variation, to reduce the cogging torque we use PM skewing method, the torque generated after a skewing of PM is show in Fig.3.26, the amplitude of cogging is significantly reduced. Skewed torque is less than the no skewing torque generated**.**

A- Pulsating Torque Components

In **[7]** torque ripple components of PMs machine are categorized very clearly. Hence, the same terminology for de fining torque ripple components according to their origin will be used here as well. Four types of torque ripple are described:

- ✓ Pulsating torque: torque ripple component produced by the space harmonic components of the windings and PMs.
- ✓ Fluctuating torque: torque ripple component produced by the time harmonic components of the input current (non-sinusoidal current).
- ✓ Cogging torque: torque ripple component due to the reluctance variations in the airgap, mainly because of slotting. This component also exists when there is no current, so it can be determined easily with the FEM by calculating the torque for several positions of the rotor
- ✓ Inertia and mechanical system torque

The fluctuating and the mechanical system torques can't be improved during the design stage. The pulsating and the cogging torque components should be studied. Cogging torque can be removed by skewing the magnet by one slot pitch **[7]**. Also odd numbers of slots are known to reduce the cogging torque to an acceptable level **[7]**.

B- Minimizing Cogging Torque

The cogging torque components are show in Fig. 3.27. Cogging torque is one of the most important sources of torque oscillation [8], [9]. Pole shifting and skewing are the main methods to reduce the cogging torque [9], [10]. The simplest method is skewing the magnets. To find the optimum skew angle of A-TFPMSM, a 3-D FEM analysis for seven different skew angles is used.

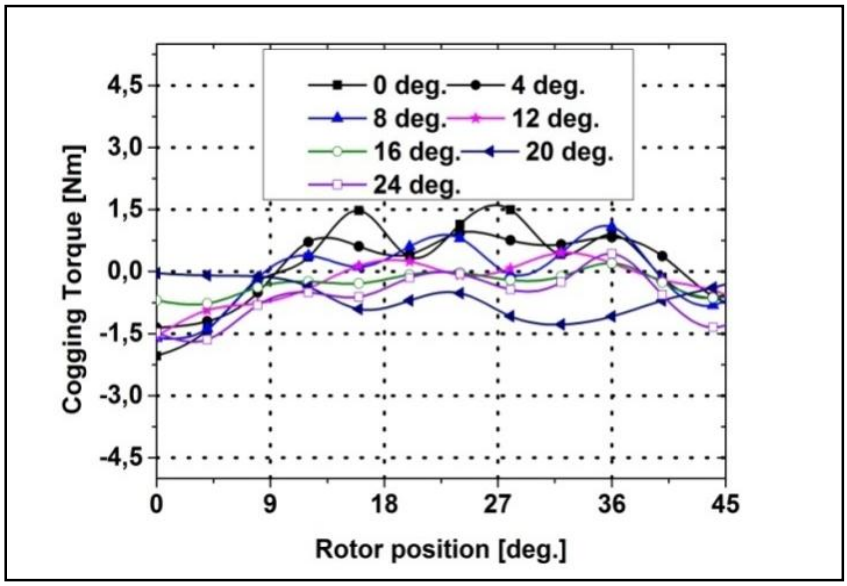

Fig. 3.27: Cogging torque for various skews angles.

The back-EMF waveforms of skewed PM rotor are shown in Fig. 3.28 When the PM core is skewed too deeply, the amplitude of back-EMF declines sharply. The FEM simulation is run for the skew magnet angles 0, 4, 8, 12, 16, 20, and 24 degrees. The results of the simulation are in Fig. 3.27. The peak to peak values of the cogging torque are shown in Fig. 3.29. The no-skew cogging torque is

1.55Nm while at 16 deg. skew the minimum cogging torque of 0.8Nm is achieved. Further increasing the skew angle, the cogging torque starts to increase.

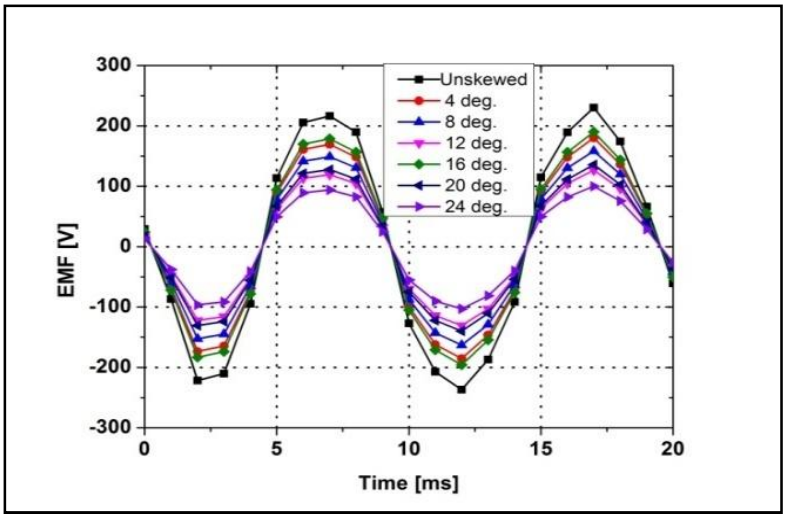

Fig. 3.28: Back-EMF waveforms.

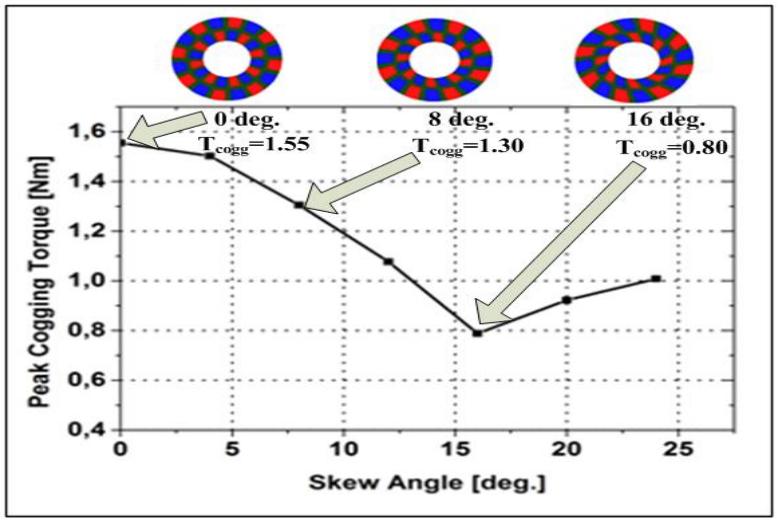

Fig. 3.29: Peak cogging torque against skew angles.

3.3.3. Solving Nonlinear Equations in FEA

The materials in an electric machine have non-linear magnetic characteristics Fig.3.30. The permeability of the materials constituting the magnetic circuit changes with the variation of the magnetic field within the machine. So the permeability is a function of the flux density. The ANSYS software uses in its calculation algorithm, the method of Newton Rhapson.

The ferromagnetic parts of the first machine consist of two different materials: one solid (steel 1008) for the stator parts and the other laminate consisting of a stack of 3% silicon-iron plates for back disk rotor (PMs). Due to the difficulty of manufacturing the laminated parts of the stator, we try to manufacture the latter by the iron powder composition (SMC).

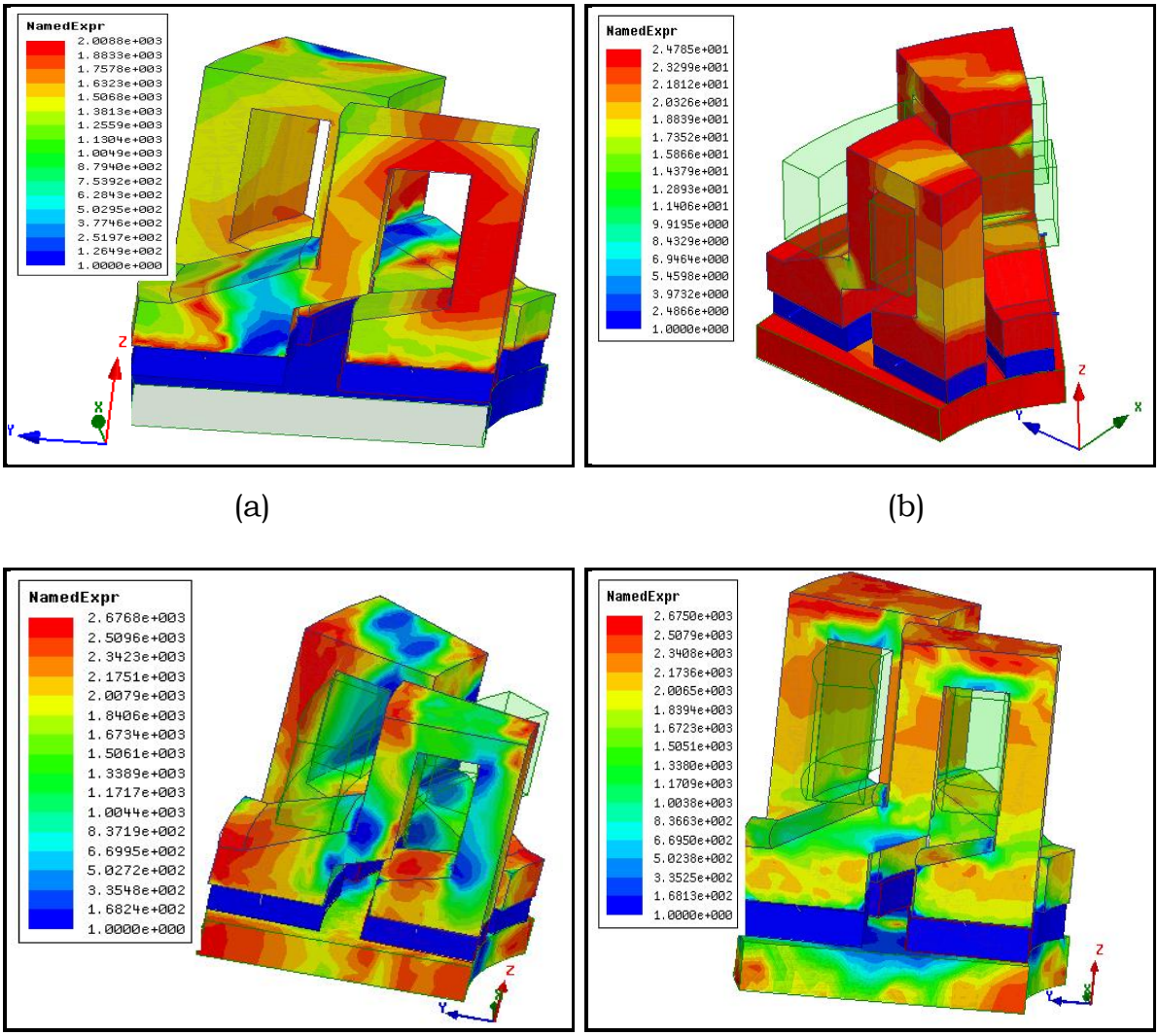

Fig. 3.30: Variation of relative permeability (non linear). (a) Solid materiel, (b) x direction, (c) y direction and (d) z direction (K_f=0.96).

We give in Fig. 3.31 the BH characteristics of these ferromagnetic materials in the direction of easy magnetization. 3% Silicon Iron is characterized by lower

saturation induction but relative permeability in its larger linear operating range than SMC, soft magnetic composites (SMC) generally have good magnetic properties such as good relative permeability and high magnetic saturation combined with high electrical resistance. In addition, they have quite unique possibilities for conducting flux in all three dimensions.

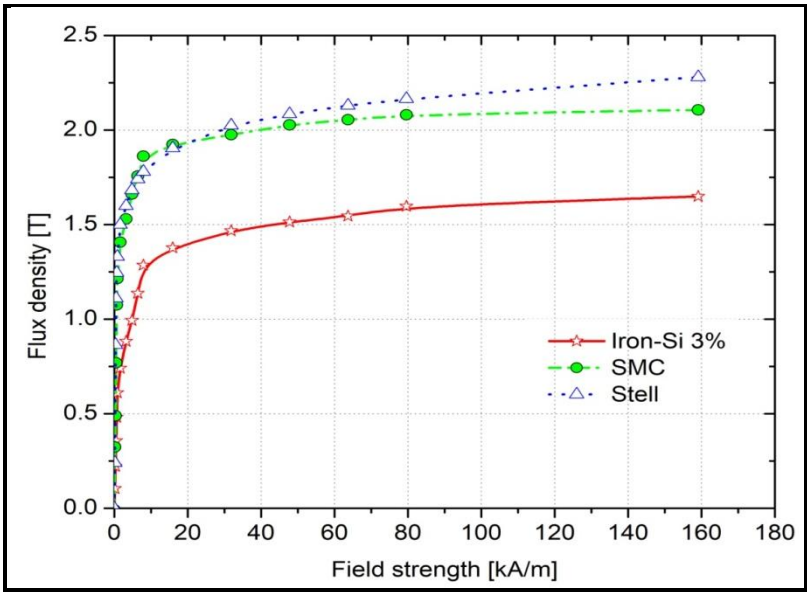

Fig. 3.31: BH curves of A-TFPMS machine parts materials.

The laminated parts are defined by two characteristics: the constitutive law is given according to the plane of the sheet (plane <xoy>) and an equivalent relative permeability μ_{req} modeling the lamination along the z axis. This permeability is calculated according to the expansion coefficient according to equation 3.27 [11]. This gives the relation between the relative permeability of the sheets as a function of the relative permeability of the material in the linear case and the stacking coefficient of the lamination sheets.

$$\mu_{req} = \left(\frac{1}{\mu_{r.\inf}} k_f + 1 - k_f \right)^{-1} \tag{3.27}$$

With $k_f = \dfrac{thikness.of.plate}{thikness.of.plate + insulation.thikness}$

The variation of the relative permeability equivalent, as a function of the stacking coefficient and the initial permeability (μ_r=2000), is given in Fig. 3.32,

as shown, the change from a solid material to a laminated material characterized by an expansion coefficient which decreases by 10 times the value of the equivalent permeability.

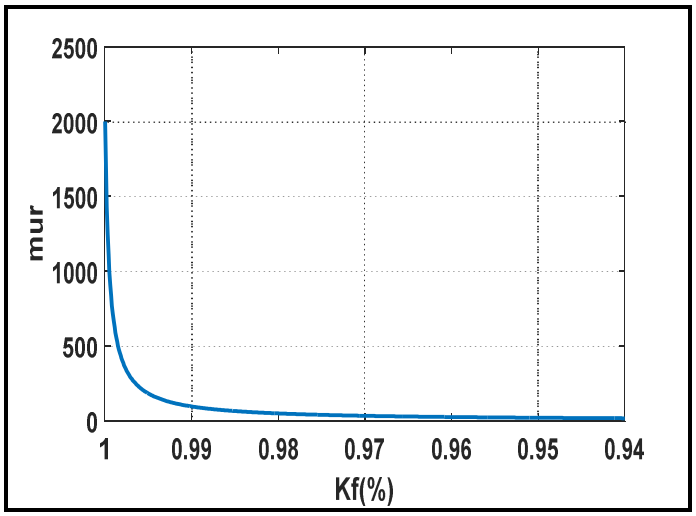

Fig.3.32: Relative permeability variation as a function of stacking coefficient.

3.3.4. Losses Calculated in FEA

In this section the author wishes to compute the coreloss of the A-TFPMS machine. In the FEA Transient solver, we are able to compute coreloss, hysteresis loss, stranded loss and eddy current loss. We need to enter the coreloss data values of the all materials are using.

3.3.4.1. Core Loss Formulation in 2D Transient Simulation

According to simplistic physic concept of core losses in ferrous materials the losses can be divided into hysteresis, classical eddy current and anomalous or excess losses. The specific core loss energy over a magnetization cycle can be expressed as a sum of the loss components.

This formulation (Eq. 3.28) is applicable when the magnetizing field waveform over the magnetization cycle is assumed to be sinusoidal. For a proper core loss evaluation it is necessary to consider the instantaneous flux density 3D waveform at different parts of the core (Eqs. 3.32, 3.33 and 3.34).

Core loss is normally computed in the frequency domain with Steinmetz equation with Bertotti modification.

Losses separation approaches for ferro-magnetic materials are summarized as shown.

$$P_{CL} = P_{hy} + P_{ec} + P_{ex} \tag{3.28}$$

Hysteresis loss $\boldsymbol{P_{hy}}$

$$P_{hy} = K_{hy} f B_m^{\beta} \tag{3.29}$$

Classic eddy current loss $\boldsymbol{P_{ec}}$

$$P_{ec} = K_{ec} \left(f B_m \right)^2 \tag{3.30}$$

Excess loss $\boldsymbol{P_e}$

$$P_e = K_e \left(f B_m \right)^{1.5} \tag{3.31}$$

Where $\boldsymbol{K_{hy}}$, $\boldsymbol{K_{ec}}$ and $\boldsymbol{K_e}$ are the coefficients of core losses versus frequency curve to each material are using in this analyzes, to calculate them the author used the interpolation technique of core losses curves.

Table 3.2: Manufactory data losses materials are used [W/kg].

B [T]	P. losses
0	0
0.166	0.746
0.267	1.19
0.372	1.79
0.473	2.54
0.563	3.28
0.664	4.63
0.785	6.12
0.896	7.61
0.991	8.81
1.18	11.9
1.45	18.2
1.71	24.2
1.86	26.1
1.92	27.8

(a) SMC data losses

B [T]	P. losses
0	0
0.1	0.1
0.2	0.2
0.3	0.4
0.5	0.6
1	5
1.2	8
1.4	10
1.6	13
1.8	16

(b) Iron-Si3 data losses

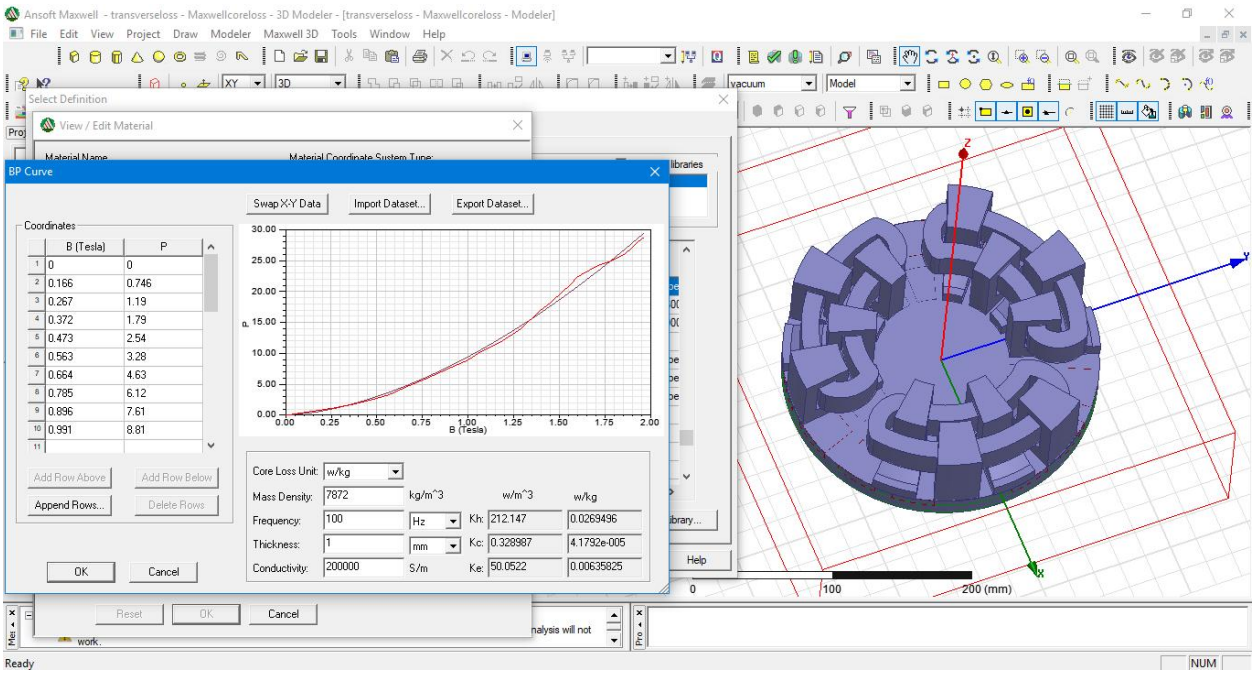

(a)

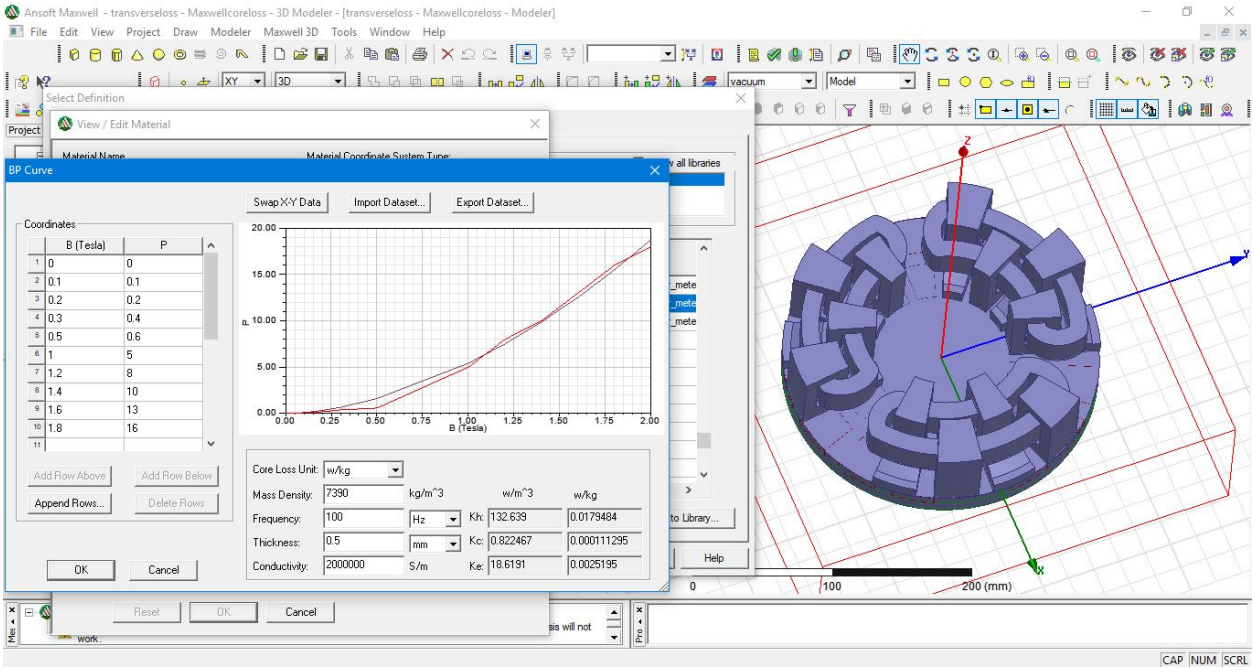

(b)

Fig. 3.33: core losses data and fitting curve for (a) SMC powder and (b) iron-Si3 material.

By using two different data from manufacturer data sheet in Table 3-1(a) and (b), at 200 Hz coefficients are calculated as K_{hy}=0.017984, K_{ec}=11.3*10^{-5} , and K_e=2.52x10^{-3} for iron-Si3. Also for SMC coefficients are calculated as K_{hy}=0.026496, K_{ec}=4.179*10^{-5} , and K_e=6.35x10^{-3}. Resulting approximated core loss curves and actual data from the core loss curves are shown in Fig.3.33 for different maximum magnetic flux density. The Maxwell solver requires the coefficients $\boldsymbol{K_{hy}}$, $\boldsymbol{K_{ec}}$ and $\boldsymbol{K_e}$. A special menu allows the coefficients to be derived from manufacturer core loss data (Core Loss versus Frequency curve).

6. Conclusion

In this chapter, we began by introduce the geometric and physical bases of the field problem. The equations present the electromagnetic field have been formulated for the different components of the machine. Subsequently, the boundary conditions to be imposed in the field problem were discussed. The co-energy method is put forward to calculate the electromagnetic torque from the result of the field problem. A formula for computation of the magnetomotrice force has been presented based on the integration of the magnetic vector potential on the surface of a conductor. To complete the definition of the field problem, the coupling equations for the field and the external electric circuit have been described for the no-load and load conditions. Taking into account the dynamics of the movement, through the sliding surface, and the non-linearity of the materials, through the method of Newton-Rhapson, are also integrated in the finite element model of the machine. The calculation of core losses in the different parts of this machine is also integrated in FE method by using of Bertotti modification and calculated their coefficients.

The 3-D finite element analysis of the axial transverse flux machine provides the magnetic flux density values in the different sections of machine at no-load. The flux density values are within normalized design intervals, the magnetic flux density distributions are shown. The optimization of the cogging torque has been studied, and the magnet skew method is used.

Bibliography -3-

[1] D. Oleksandr. “Study on permanent magnet transverse flux machine”. Louisiana State Universit. USA . 2012.

[2] S. K. Mukerji, A. S. Khan and Y. Singh. “Electromagnetics for Electrical Machines”. Taylor & Francis Group. 2015.

[3] http://www.femm.info/wiki/HomePage.

[4] http://www.ansys.com. “user’s guide. Maxwell 3D”. ANSYS Inc. Southpointe. 2015.

[5] J. P. A. BASTOS, N. Sadowski. “Electromagnetic Modeling by Finite Element Methods”. Universidade Federal de Santa Catarina Florianopolis, Brazil. Marcel Dekker. 2010.

[6] . P. C. San. “Principale of Electrical Machines and Power Electronics”. John wehly and Sones. Canada, 1997.

[7] D.C. Hanselman. Effect of skew, pole count, slot count on brushless motor radial force, cogging torque and back emf. IEE Proc. on Elec. Power Appl., 144(5):325-330, September 1997.

[8] Bianchi, N. and Bolognani, S., “Design techniques for reducing the cogging torque in surface-mounted PM motors,” IEEE Trans. Ind. Appl., Vol. 38, No. 5, pp. 1259–1265, September/October 2002.

[9] Aydin, M., “Effects of magnet skew in cogging torque minimization ofaxial gap permanent magnet motors,” in Proc. 18th ICEM, Villamoura, Portugal, 2008.

[10] Aydin, M., Huang, S., and Lipo, T. A., “Design, analysis, and control of a hybridfield-controlled axial-flux permanentmagnet motor” IEEE Trans. Iind. Elec., Vol. 57, No. 1, January 2010.

Chapter Four

MEC Study of Axial-Transverse Flux Permanent Magnet Machine

Chapter Four

MEC Study of Axial-Transverse Flux Permanent Magnet Machine

1. Introduction

The using of the MEC (magnetic equivalent circuit) is: approach, surfaces of equal magnetic potential within the machine are chosen using engineering judgment. Volumetric tubes are then created to model the paths of magnetic flux between each surface. The ratio of the endpoint potentials to the flux enclosed by the volume represents a magnetic reluctance, which is similar conceptually to the resistance of an electric conductor. The value of the tube reluctance can be obtained from the flux tube geometry and material characteristics. By connecting points of equal magnetic potential, the magnetic characteristics of a machine can be modeled using a network of standard dc circuit elements (resistances, voltage sources. current sources). The MEC: approach represents a compromise between the FEM models and ILPM (inductive lumped parameter magnetic). In the review

of PM machines in Chapter one, it was discussed that surface-mounted permanent magnet machines have been mostly used for direct-drive applications.

The aim of this chapter is to create a generalized analytical model (MEC) for this topology of permanent magnet (PM) machine. Therefore, a generalized MEC model for this topology of A-TFPM machines is discussed in this chapter with the following outline. Firstly, an introduction about MEC method theory. Secondly, generalized electromagnetic circuit analysis models of our design machine are developed in the second chapter. The models include nonlinear B-H curve characteristics of materials are using. Next, the proposed analysis model is verified through a comparison with finite element analysis of the previous chapter.

2. Machine Structure and Principal of Operation

2.1. Machine Topologies

Fig. 4.1 shows the proposed structure of the A-TFPMSM, which consists of a rotor core, a stator core, winding, and permanent magnets. The rotor of this machine is totally passive and the permanent magnets are glued of it, the stator cores it can be lamination with iron or with solid parts with base of iron or SMC (Soft Materiel Composite) and the winding of armature (Fig. 4.1). The stator coils are powered by alternating currents and allow generating the torque at the machine.

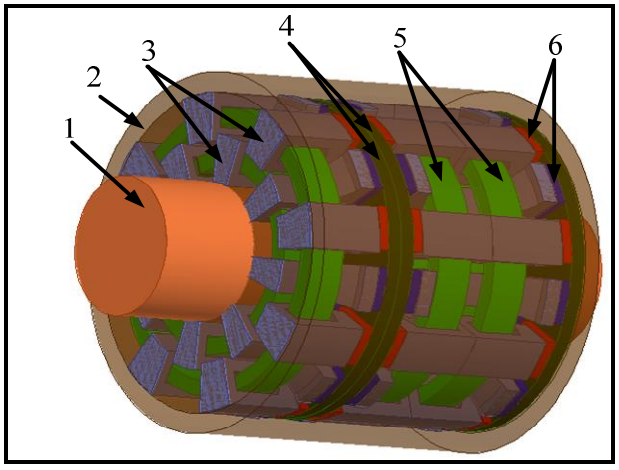

Fig.4.1: Structure of A-TFPMSM. (1) Shaft. (2) Housing. (3) Stator cores. (4) Rotor. (5) Coils. (6).Permanent magnets.

The stator winding of A-TFPMSM features a modular structure and can be arranged as needed. The stator winding can be arranged into three phases both for the one-side machine Fig. 4.2 (b), and for the double-side machine Fig. 4.2 (a); or one phase for one side machine Fig. 4.2 (d), and for multi-sided machine Fig. 4.2(c).

In Fig. 4.2b, the stator winding form is ring portion, in this design has two disadvantages, the one is the end rings and the second is the poles pitch of the stator and the rotor aren't equals. And in the anther side the main advantage of this design is, can be use it as simple face or multi face.

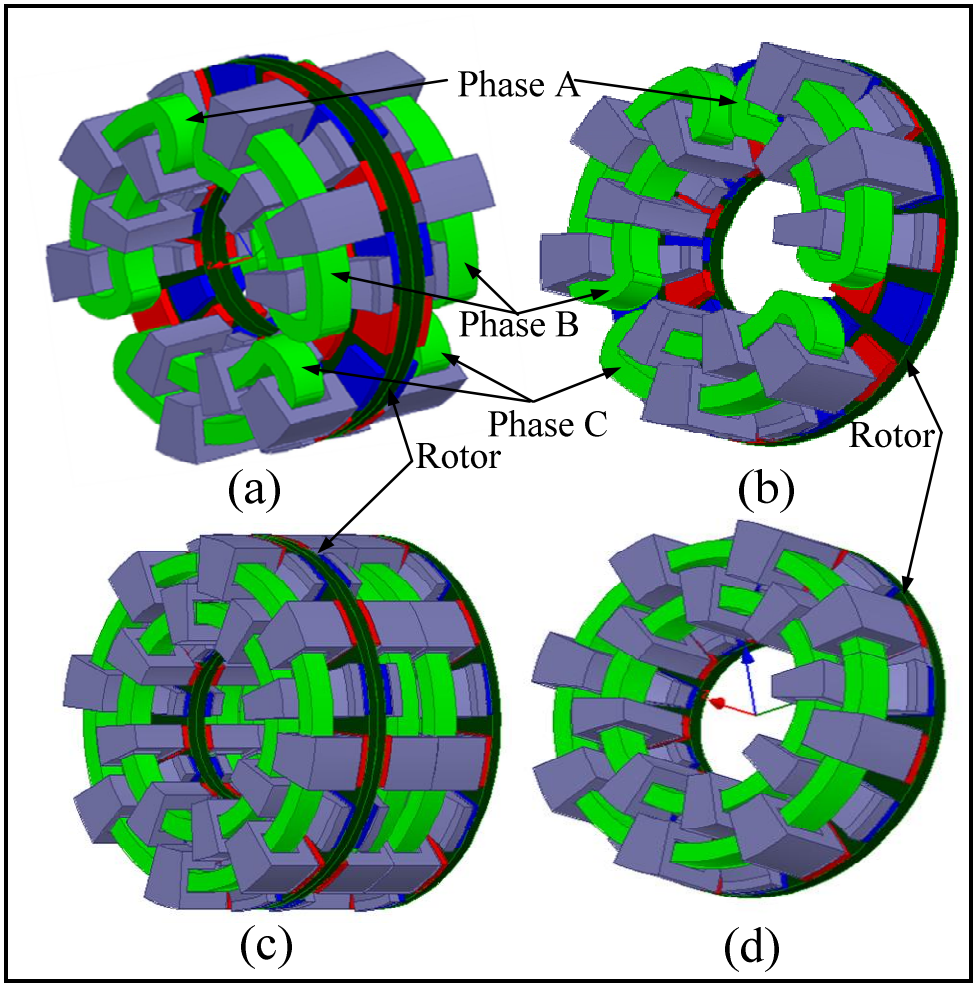

Fig.4.2: Configuration of A-TFPMSM.

In Fig. 4.2d, the main two disadvantages of the first design (Fig. 4.2b) are solved; by using the ring form winding, there no end windings and the pole pitch of the stator and the rotor are the same. But it has one problem, the

simple face construction is impossible, will be deal us to the final configuration (Fig. 4.2c).

Fig. 4.2 (c) and (d) show that the structure of A-TFPMSM has a three-phase ring winding, each phase occupies one side of the stator. The machine can be built with multi-sided stator also. This configuration, which is shown in Fig. 4.2(c), is even more advantageous and will be dealt with in this thesis.

2.2. A-TFPMS Machine Principle

The cross-sectional view of the machine in Fig. 4.3 shows the magnetic flux path. Two quasi U cores are traversed by fluxes going in opposite directions. The proposed position of the stator core is very important, because the change of the direction of magnetic flux path is necessary to keep the torque orientation. Two permanent magnets are in the inner and outer radiuses, and magnetized in opposite direction, generating the flux in opposite directions for two consecutive poles.

The windings are supplied by an alternating power, creating the magnetic flux in the stator. The stator flux interacts with the rotor permanent magnet field, which produces the force that rotates the machine.

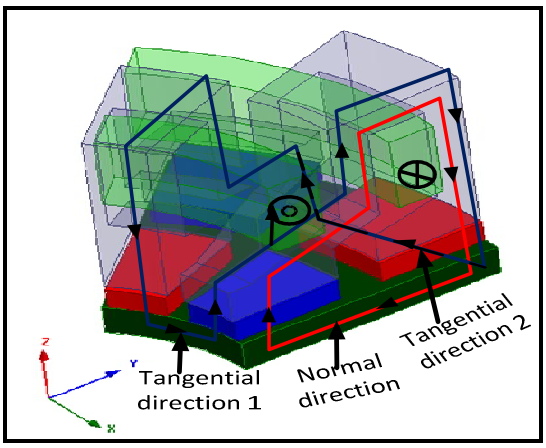

Fig.4.3:.Flux path in two poles pairs of A-TFPMSM for single sided and one phase.

3. Models are Using in Design Procedures

These models can be classified into two main families [1]:

- Numerical models.
- Analytical models.

3.1 Numerical Models

They are based on methods of numerical resolution of the mathematical equations describing the functioning of the system studied. The finite element method and finite difference represent the most widely used numerical methods.

Once the digital model has been developed and validated, it can be applied to several electrical machine structures without having to adapt it. In the commercial world, these codes are paired with one or more graphical modelers and relevant interfacing, and the time required solving basic problems decreased to the time needed to draw the structure studied. We also note the progress of computing capabilities, the computing time for solving 3D problems remains high [1].

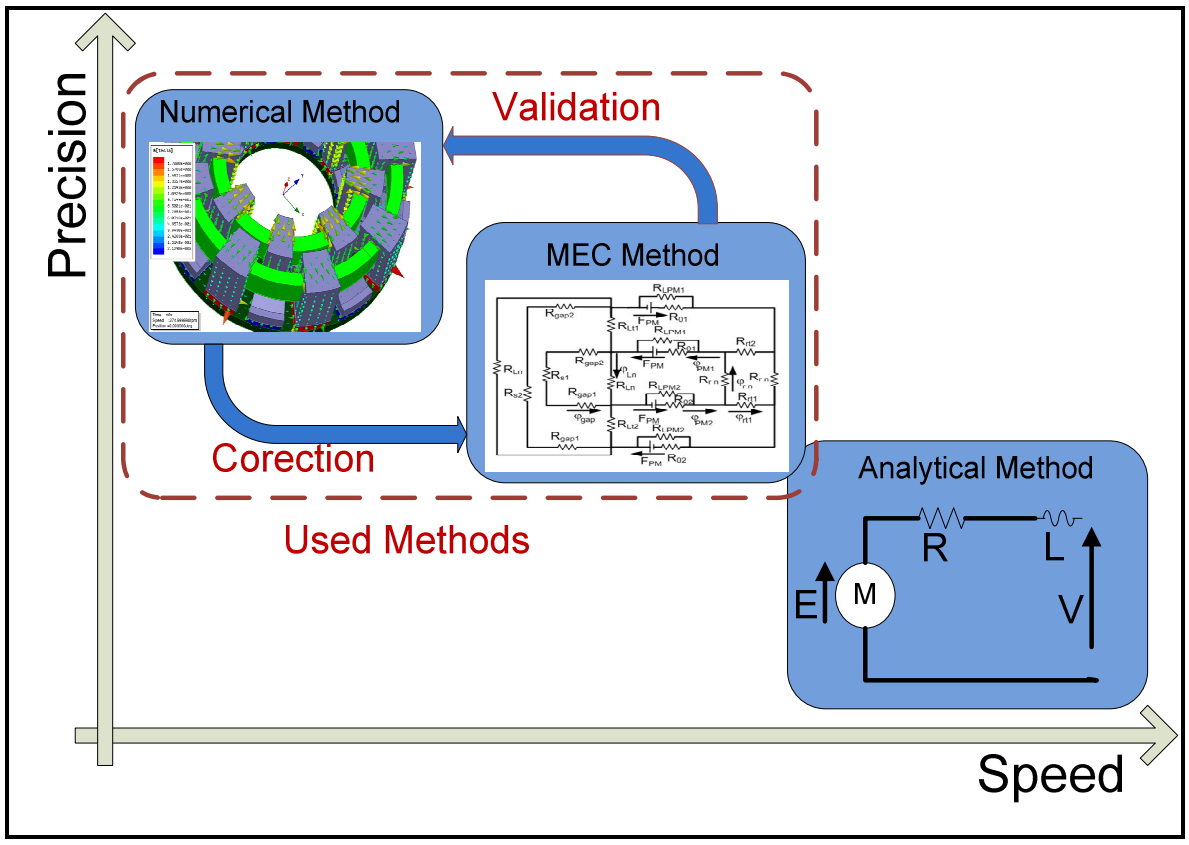

Fig.4.4: Classification of modeling methods in a precision-speed calculation.

Fig. 4.4 gives a good overview of the classification of modeling methods in a precision-speed calculation. In order to have a fast and accurate model, we chose a combination of analytical methods and equivalent circuit methods.

However, comeback to numerical methods is necessary to validate and correct the MEC model thus established.

3.2 Analytical Models.

3.2.1 Method Based on the Analytical Resolution of Maxwell Equations

Unlike numerical models, these methods are based on a formal resolution of Maxwell's equations to determine the exact expression of the vector potential in the air gap of the machine studied [2]. Two hypotheses are nevertheless necessary to carry out this modeling [3] [4]:

- Ferromagnetic parts have infinite permeability.
- Axial flux paths are neglected.

Once the vector potential has been calculated, all electromagnetic quantities (torque, forces, etc.) can be determined

Among the advantages of this family of models are:

- Speed of calculation.
- The explicit link between the input parameters (geometric dimensions, physical characteristics) and the output parameters. A better understanding of the interaction between the different parameters is therefore possible.

Nevertheless, these models have a certain number of disadvantages:

- They aren't adapted to calculations of non-linear phenomena such as magnetic saturation and are not generic.
- The change of machine structure requires a complete development of all equations.

3.2.2. Reluctance Method MEC

3.2.2.1 Reluctances Calculations

The reluctance being given by a flux tube (Fig. 4.5) in a quasi-stationary magnetic field of section ***S (x)*** and of total length ***l***, the magnetic reluctance is defined as the following quantity:

$$\Re = \int_0^l \frac{dx}{\mu(x)S(x)} = \frac{1}{P} \tag{4.1}$$

With ***μ (x)*** is the permeability of the material and ***P*** the magnetic permeance.

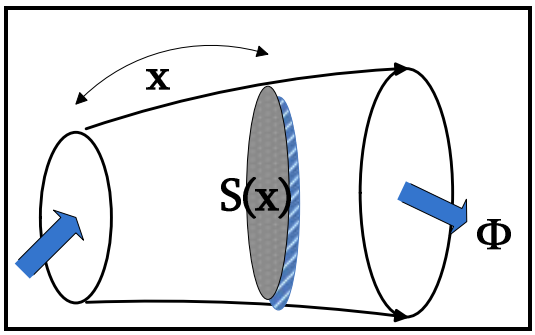

Fig.4.5: Magnetic flux tube.

Reluctances can be classified into three categories [5]:

- Reluctances invariants: these are reluctances which have fixed geometries and fixed magnetic characteristics.
- The saturable reluctances: it is the reluctances that have a permeability that depends on the magnetic excitation H.
- Reluctances with variable geometry: these are reluctances whose geometric parameters (Length of the flux tube or section of the flux tube) are variable as the reluctances modeling the air gap of an electrical machine.

Thanks to a large number of works that allowed to model electromagnetic structures using this method, different reluctance geometries have been calculated and their integrated expressions can be directly exploited. We present below some expressions of constant reluctances that one can meet in the literature [5] [6]:

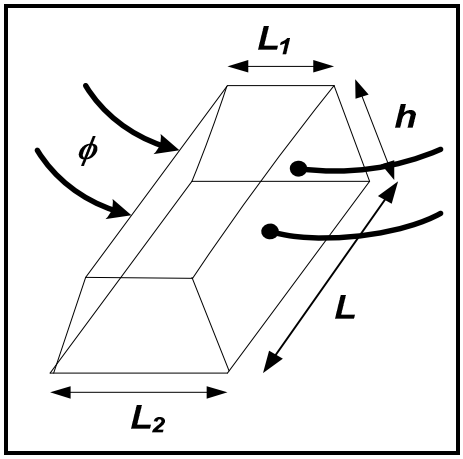

Fig. 4.6: Reluctance example.

$$\Re = \frac{L}{\mu_0 \mu_r} \frac{L_2 - L_1}{h.\ln\left(\frac{L_2}{L_1}\right)} \tag{4.2}$$

As shown in Fig. 4.7, the flux paths cutting the airgap of this machine have two loops, the first one loop is the flux line crossing the rotor permanent magnets (cross the outer and inner permanent magnets) this loop contain the normal direction flux, the second one loop is the flux line crossing the rotor adjacent permanent magnets poles (four permanent magnets), this loop has two tangential flux lines.

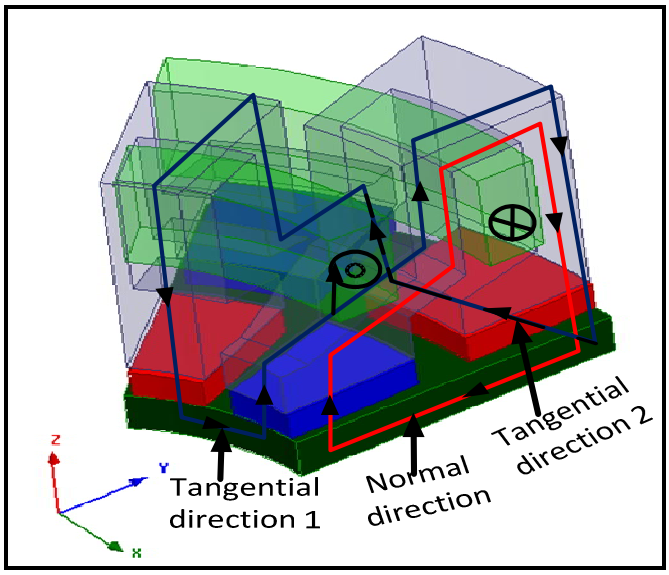

Fig.4.7:.Flux path in two poles pairs of A-TFPMSM for single sided and one phase.

In the A-TFPMS machine the development of the different reluctances parts are very hard; the flux path in this machine type has two directions, radial component (in this case the surface of reluctance is varied) and component (in this case the length of reluctance is varied). Examples of reluctances calculations are done in Fig.4.6 and Fig.4.8.

In the case of a tangential flux tube, the reluctance can be expressed as follows

$$\Re = \frac{l}{\mu S} = \frac{l}{\mu L h} \tag{4.3}$$

With ***S=Lh*** is the section perpendicular to the flux, ***l*** is the length of the flux

tube, μ is the permeability of the materiel.

In the case of a radial flux tube, can approximate the reluctance by:

$$\Re = \frac{l}{\mu S} = \frac{h}{\mu L\left(L_1 + L_2\right)/2} \tag{4.4}$$

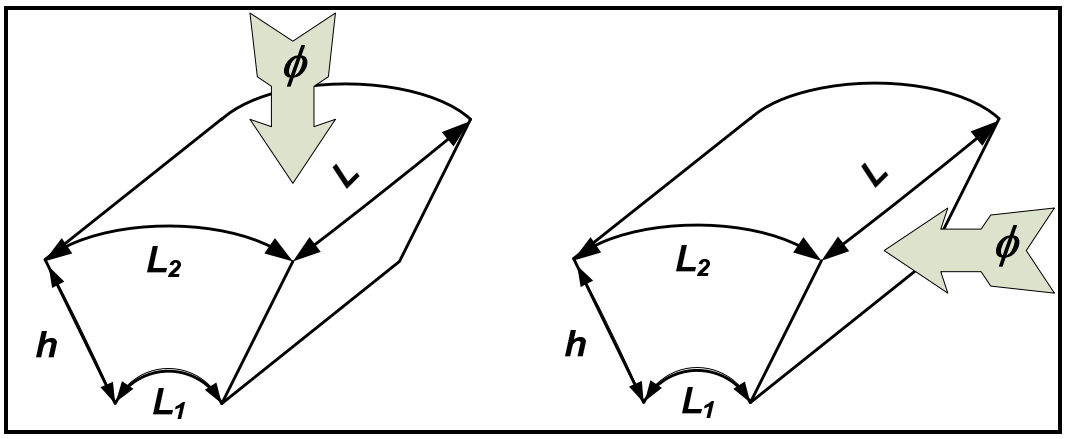

(a) (b)

Fig.4.8: Common flux tubes. (a) Radial flux tube. (b) Tangential flux tube.

The reluctance of the radial flux tube can be expressed by a more precise relation than (4.4):

$$\Re = \int_{L_2}^{L_1} \frac{dl}{\mu S(l)} = \frac{h}{\mu L} \frac{\ln\left(L_2/L_1\right)}{\left(L_2 - L_1\right)} \tag{4.5}$$

In electrical machines, two modeling approaches using reluctant techniques have already been adopted:

Modelization in plane abc [5] [7] [8]: they take into account the relative movement of the rotor with respect to the stator. We then obtain the evolution of the different parameters as a function of the rotation angle of the rotor. Harmonic studies are therefore possible. Modeling under the assumption of the first harmonic [6] [9]: the model is summed up in one position. These models do not allow harmonic analyzes but are faster.

3.2.2.2 Magneto Motive Force Source

An MMF is used to present the effect of electrical conductors in a magnetic system. The MMF source is similar to a voltage source in an electrical circuit. The value of MMF source is determined using Ampere's current law.

In particular, Ampere's law can be expressed in integral form as [10]

$$\oint \vec{H} \bullet \vec{dl} = i_{enc} \tag{4.6}$$

Where $\boldsymbol{H}$ is the magnetic vector potential and $\boldsymbol{i_{enc}}$ is the current enclosed by the line of integration. For multiple conductor winding, Equ. (4.6) is often written in the form

$$\vec{H} \bullet \vec{l} = Hl = Ni \tag{4.7}$$

Where N is the number of turns and Ni is defined as the MMF.

$$F = Ni \tag{4.8}$$

4. Magnetic Circuit Calculation

4.1 Identification of the Different Flux Tubes of the A-TFPMS Machine

The realization of a reluctance network should be firstly starting by the identification of the different flux tubes to be taken into account. This step is necessary because it makes it possible to define the geometrical characteristics for the calculation of the reluctances of the equivalent network. To observe the distribution of those flux tube by a finite element analyses of the machine is therefore necessary. Fig. 4.9 shows the different flow paths in the machine under study.

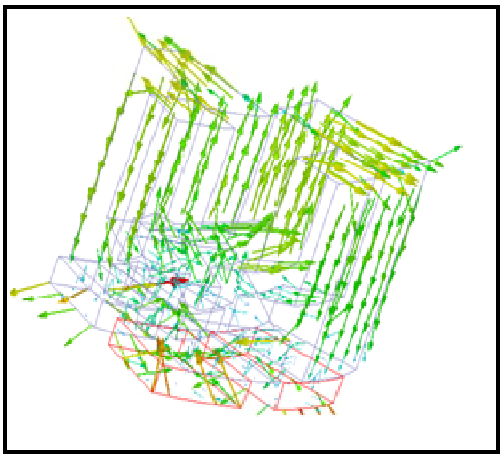

Fig. 4.9: Flux lines in the machine.

The large part of the flux is exchanged between the stator cores and the rotor PM. However, a weaker part is exchanged between the back rotor and PM poles. This section shows leakage fluxes in the same core stator legs, which

increase with the current of the machine. Thus the precise calculation of these leakage fluxes is necessary.

4.2. Linear Model without Leakage

The model presented below is based on strong assumptions, i.e the ferromagnetic parts have infinite permeability and magnetic leakage are not taken into account. Only the sources of MMF and the air-gaps reluctances are modeled. Figure 4.10 show the structure that will be modeled.

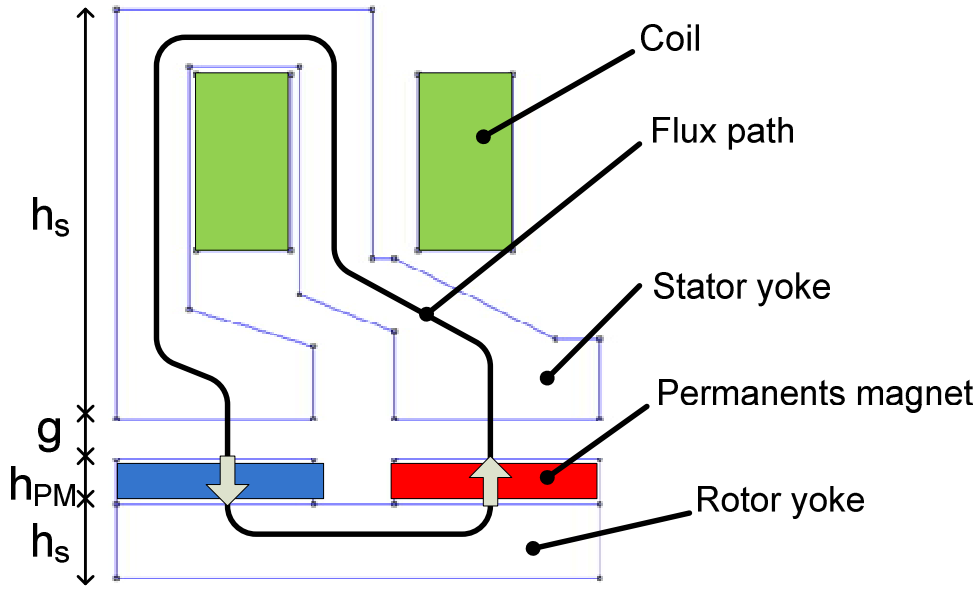

Fig. 4.10: Cross-section of a simplified magnetic circuit of A-TFPMS machine.

Using Ampere's circuit law, the contour in figure 4.10 is expressed as

$$H_s l_s + H_r l_r + 2H_g g + 2H_{pm} h_{pm} = 0 \tag{4.9}$$

Where $\boldsymbol{l}$ is the magnetic field length.

At low values of the magnetic field intensity, the flux density in iron cores increases almost linearly. The permeability of iron cores with low magnetic intensity is much larger than the permeability of the air and the magnets. Therefore, equation (4.9) can be simplified by neglecting terms of the magnetic field intensity of iron cores for the range of low magnetic field intensity as.

$$2H_{pm} h_{pm} + 2H_g g = 0 \tag{4.10}$$

From the continuity of flux, the flux $\boldsymbol{\varphi}$ is same in all machine parts $\boldsymbol{\varphi = B.A}$

Where $\boldsymbol{A}$ is the area (we assume that have a same area in 2D representation)

An equation for the B(H) characteristic of the magnets in the second quadrant

is given as

$$B_{pm} = \mu_0 \mu_{rm} H_{pm} + B_r \tag{4.11}$$

In order to calculate the flux density in the air gap, equation (4.10) is reformulated as equation (4.12) using equation (4.10) and equation of flux.

$$2\frac{B_g}{\mu_0} g + 2\frac{B_g \dfrac{A_g}{A_{pm}} - B_r}{\mu_0 \mu_{rm}} h_{pm} = 0 \tag{4.12}$$

Therefore, the air gap flux density is determined as

$$B_g = 2\frac{B_r h_{pm}}{\mu_0 \mu_{rm}} \times \frac{1}{\dfrac{2g}{\mu_0} + \dfrac{2A_g h_{pm}}{\mu_0 \mu_{rm} A_{pm}}} \tag{4.13}$$

The results obtained by this model were compared to those obtained by 3D linear FE simulations (Table 4.1). Despite the simplicity of the model developed. The relative difference between the two models exceeding 35%, shows the existence of quite significant leaks in the structure. At this point the leakages fluxes are neglects them in the MEC model presented here.

Table 4.1: Comparison of linear MEC model and FEA simulation.

	Air-gap flux induction
FEA simulation	0.7T
MEC method	1T

4.3 Nonlinear Model without Leakage Reluctance

When the magnetic field intensity ***H*** in iron cores is increased, their flux density increases nonlinearly, which lead to a decrease in the permeability of the iron cores. Further increasing the magnetic field's intensity results in the iron cores being saturated and an increase in the reluctances of the magnetic path. Therefore, it is necessary to consider the nonlinear characteristic of the flux density of the iron cores when designing electric machines meant to operate in the region of higher flux density.

- **How taking account the saturation level at the reluctance**?

The study of saturation level of reluctant circuit has been the subject of several studies [11] [12]. The method adopted consists in varying the relative permeability of the ferromagnetic parts of the machine according to a nonlinear expression. Several analytical expressions of characteristic B (H) found in the literature [13]. Four analytical expressions of this characteristic have been investigated, in order to select the one that best corresponds to the experimental B (H) curve available [14].

The first expression is based on an arc-tangent formulation:

$$\begin{cases} \mu_r(H) = 1 + \dfrac{2B_{sat}}{\mu_0 H \pi} \arctan\left[\dfrac{\pi}{2}\left(\mu_{r\max} - 1\right)\dfrac{\mu_0 H}{B_{sat}}\right] \\ B = \mu_0 \mu_r(H) H \end{cases} \tag{4.14}$$

Where:

$\boldsymbol{\mu_{rmax}}$ Slope of the linear part of the B (H) curve and $\boldsymbol{B_{sat}}$ Induction at saturation.

The second analytic expression of characteristic B (H) is based on a square root formulation:

$$\begin{cases} B(H) = \mu_0 H + J_s \dfrac{H_g + 1 - \sqrt{\left(1 + H_g\right)^2 - 4H_g\left(1 - \alpha\right)}}{2\left(1 - \alpha\right)} \\ H_g = \left(\mu_{r0} - 1\right)\dfrac{\mu_0 H}{J_s} \end{cases} \tag{4.15}$$

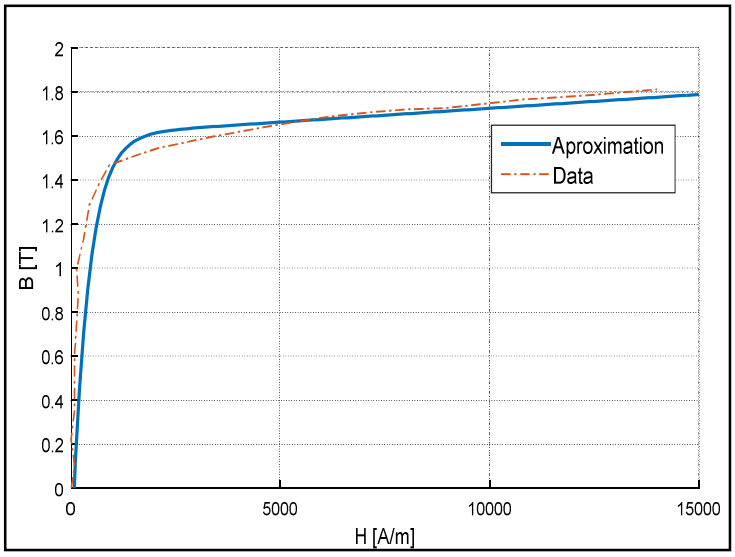

(a)

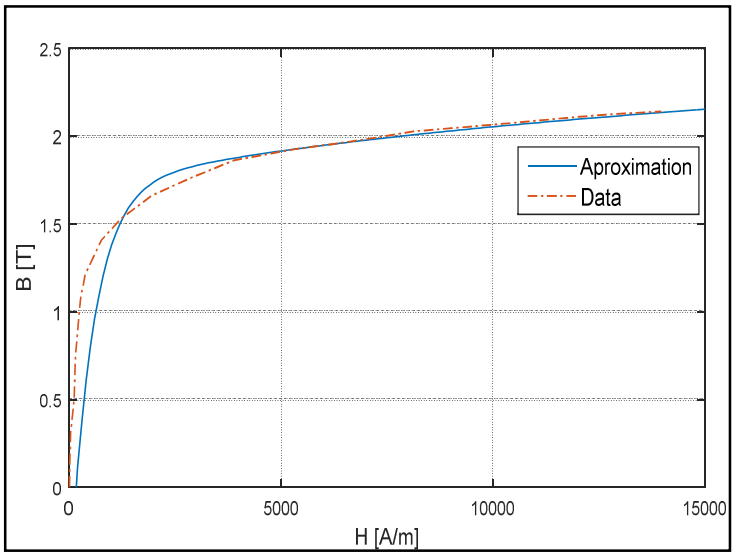

(b)

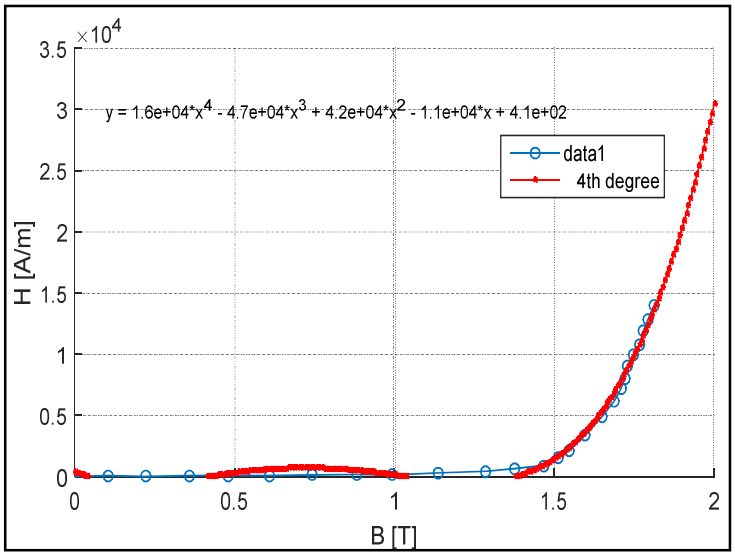

(C)

Fig. 4.11: B (H) curves comparison of different analytical expressions. (a) and (b) double exponential an approximate, (a) Iron 3%Si and (b) soft material (SMC), (c) polynomial function of Iron 3%Si.

The third is a double exponential an approximate expression point has therefore been obtained is formalized by the following equation [15]:

$$B = J_{sat} - A_1 e^{-\frac{H}{H_1}} - \left(J_{sat} + A_1\right) e^{-\frac{H}{H_2}} + \mu_0 H \tag{4.16}$$

With J_{sat}=1.6, A_1=0.3, H_2=400 and H_1=10.for Iron3% material. And J_{sat}=2, A_1=0.3, H_2=550 and H_1=7000 for SMC material.

The various coefficients of the above-mentioned expression were determined by the least squares method in order to minimize the differences between the analytical expression and the real curve (Figure 4.11).

In some paper [16] the researchers are trying to use a simple equation, in order to obtain the analytical MEC model, the relationship H(B) in saturated region is approximated with a polynomial function by fitting.

$$H(B) = p_1 B^4 + p_2 B^3 + p_3 B^2 + p_4 B + p_5 \tag{4.17}$$

Because the relative permeability is get by dividing flux density by magnetic field strength, it is deduced that :

Coefficients: p1=16397, p2=-47098, p3=41809, p4=-11382 and p5=409.29.

$$\mu_r(B) = \frac{B}{p_1 B^4 + p_2 B^3 + p_3 B^2 + p_4 B + p_5} \tag{4.18}$$

The equivalent circuit of the magnetic reluctance of the model is shown in Fig. 4.12 (a). In the figure, the white rectangles with bold lines represent the iron core reluctances; the gray rectangles represent the air gap reluctances. The black rectangles represent the magnet reluctances.

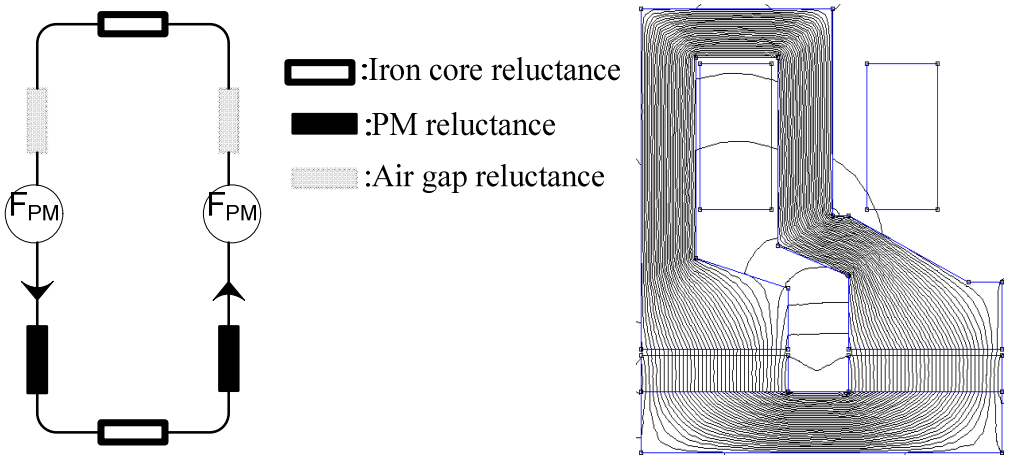

Fig. 4.12: A simplified equivalent reluctance model**.** (a) and (b).

The total magnetic reluctance of the magnetic circuit of the model is given by

$$R_t = R_{gap} + R_{PM} + R_S + R_r \tag{4.19}$$

Where R_{gap} is the reluctance of the air gap, R_{PM} is the reluctance of the magnets, R_r is the reluctance of the yoke of the moving part and R_s is the reluctance of the tooth of the stationary part.

General expressions of the magnetic reluctances are given as a function of the magnetic field length, its permeability and area.

The *MMF* of the permanent magnet is defined as:

$$F_{PM} = \frac{B_r h_{PM}}{\mu_{rm}\mu_0} \tag{4.20}$$

Where μ_0, μ_{rm}, B_r, and h_{PM} are the air permeability, the recoil permeability, the remanence and the length of the permanent magnet in *z*-axis direction, respectively.

The reluctance of the permanent magnets R_{PM} is defined as:

$$R_{PM} = \frac{h_{PM}}{\mu_{rm}\mu_0 S_{PM}} \tag{4.21}$$

Where S_{PM} is the sections of the permanent magnet.

The reluctances modeling the air-gap, depend on the active air gap of the machine, the width of the stator shoe core and the radial length of the machine. In this stage of simulation the author assumed, the air-gap inner and air-gap outer are same. It expression is given by equation 4.22.

$$R_{gap} = \frac{g}{\mu_0 S_{gap}} \tag{4.22}$$

Where $S_{gap} = \frac{2\pi}{p}\alpha\left(\left(R_i + W_{st}\right)^2 - R_i^2\right)$

The flux caused by the magnets was calculated as equation (4.23) from the continuity of flux. The flux caused by the magnets is also calculated as a function of the magnetic field intensity of the magnets H_{pm}, the magnetic field length of the magnets h_{pm} and the total reluctance in the equivalent circuit R_t as equation (4.19).

$$\phi = \frac{H_{PM} h_{pm}}{R_t} \tag{4.23}$$

By using the expression obtained from the characteristic B (H), the values of the different reluctances can be calculated taking into account the saturation phenomenon.

The calculations are as follows, from the continuity of flux, it is possible to calculate the flux density in the deferent parts of machine. After determining the flux density in the air gap, the procedure and the expressions to calculate the flux ***φ***, the flux linkage ***λ*** and the no-load voltage ***EMF*** are the next step.

The procedure to determine the flux density, the flux, the flux linkage and the no-load induced voltage of a magnetic circuit including nonlinear characteristic is made as the following steps

1) Input predefined parameters of A-TFPMS machine.

2) Determine the initial values of the flux densities of all machine parts using a FEA.

3) Assume the initial value of the permeability. In this work we assume μ_r=300 as an initial value.

4) Calculate the magnetic field intensity of the stator core part H_s by

$$H_{PM} = \frac{B_s h_{pm}(2)}{\mu_{rs}\mu_0(3)}$$

5) Re-calculate the flux density of the stator core part B_s with the B-H curve of the iron core (using equation 4.16). A same work for auther machine parts.

6) Re-calculate the permeability of the stator core part μ_{rs} by $\mu_{rs} = \frac{B_s(2)}{H_s\mu_0(3)}$,

$$\mu_{rs} = \frac{B_s(5)}{H_s\mu_0(4)}$$

Calculate the permeability of the rotor yoke of the moving part μ_{rr}.

7) Calculate the total reluctance of the magnetic circuit R_t by equation (4.19).

8) Calculate the flux ***φ*** by equation (4.22)

9) Re-calculate the flux density of the stator core part B_s by $B_s = \frac{\varphi}{S_s}$ using ***φ*** calculated in *(8)*.

10) Re-calculate the magnetic field intensity of the stator core part H_s by

$$H_s = \frac{B_s(9)}{\mu_{rs}\mu_0(6)}$$

11) Re-calculate the flux density of the stator core part B_s with the B-H curve of the iron core (using equation 4.16) H_s of (10).

12) Compare $\boldsymbol{B_s}$ calculated in *(9)* with $\boldsymbol{B_s}$ calculated in *(11)*. If $|B_s(11) - B_s(9)| \leq \varepsilon$, then proceed to the next step. If not, go back to *(6)*.

13) Re-calculate the flux densities of the air gap $\boldsymbol{B_g}$, the magnets $\boldsymbol{B_m}$ and the rotor yoke of the moving part $\boldsymbol{B_{ro}}$ using the continuity of flux.

14) Re-calculate the flux $\boldsymbol{\varphi}$, and calculate the flux linkage $\boldsymbol{\lambda}$ and the no-load induced voltage ***EMF***.

4.4 Nonlinear Model with Leakage Reluctances

Until this step of modeling, the problem of leakage magnetic in the structure isn't take account. For non saturation model, these leaks exist in a restricted way, but when the magnetic saturation phenomenon is integrated, the reluctances of the ferromagnetic parts increase. As a result, leakage paths become important. We propose to model of these leakage paths and integrate them into in the saturation reluctance model presented in the previous paragraph.

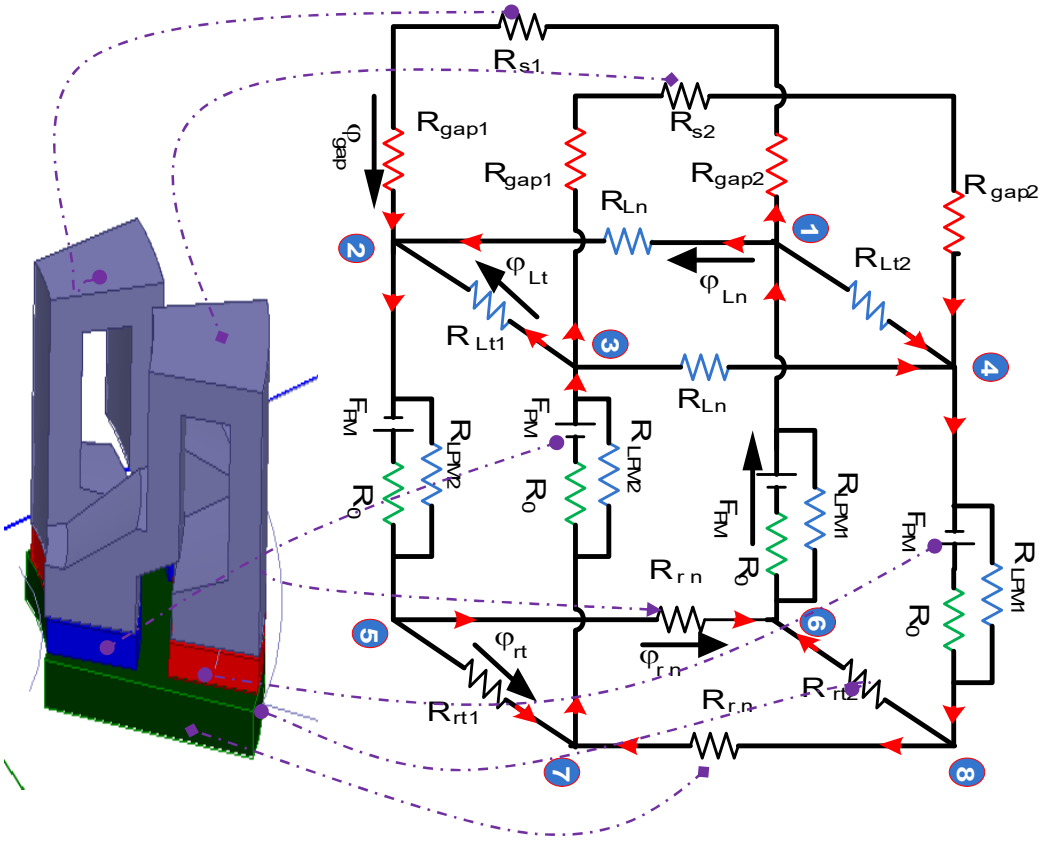

Fig. 4.15: A-TFPMSM simplifies equivalent 3D magnetic circuit.

The electromagnetic characteristics of the A-TFPMS machines are the same and repetitive in every one pole pair. Therefore, the electromagnetic equivalent

circuit of one pole pair is considered for the analytical model. The equivalent circuit including the leakage fluxes is illustrated in Fig. 4.15. The black resistances are the iron core reluctances, the red resistances are the air gap reluctances and the green resistances are the PM reluctances. The bleu resistances are the leakage flux reluctances.

Fig. 4.15 presents MEC of two neighbor poles, the geometry of stator cores are different we should us two reluctances R_{s1} and R_{s2}, the machine air gap also has two sections first one outer and second one is inner outer for this raison the machine has two air-gap reluctances R_{gap1} and R_{gap2}, PMs dimensions aren't equals (outer section greater than inner section) this implicate to $R_{01}$and R_{02} are different reluctances, the rotor has four reluctances; normal reluctances R_{rn} are equals and tangential reluctances R_{rt1} and R_{rt2} aren't equals.

After the found the MEC equivalent circuit the next step is calculates the reluctances expression for all machine parts and also the leakage reluctance wish is the hard step. Firstly, in Figures (4.16) (a) and (b) the geometry of stator cores are varied, each portion it has self section, these are involved the derivations of the equivalente section S and length l.

4.4.1 Stator Cores Reluctances

The total reluctance of the first stator is the sum of all stator portions as fellow:

$$R_{S1} = R_{S11} + R_{S12} + R_{S13} + R_{S14} + R_{S15} + R_{S16} \tag{4.24}$$

The reluctance RS_{11}

$$R_{S11} = \frac{h_{st}}{\mu_0 \mu_{r11}(B) \frac{2\pi}{P} \alpha \left(R_o^2 - \left(R_o - w_{st} \right)^2 \right)} \tag{4.25}$$

The reluctance RS_{12}

$$R_{S12} = \frac{h_s - h_{st} - h_{sy/2}}{\mu_0 \mu_{r11}(B) \frac{2\pi}{p} \alpha \left(R_o^2 - \left(R_o - B_{st} \right)^2 \right)} \tag{4.26}$$

The reluctance RS_{13}

$$R_{S13}=\frac{l_{s12}}{\mu_0\mu_{r11}(B)\frac{2\pi}{p}\alpha h_{sy}\int_{R_o-R_s-b_{st}}^{R_o}\frac{x}{dx}(b_s+b_{st})}=\frac{b_s+b_{st}}{\mu_0\mu_{r11}(B)\frac{2\pi}{p}\alpha\frac{h_{sy}(b_s+b_{st})}{\ln\left(\frac{R_o}{R_o-R_s-b_{st}}\right)}} \quad (4.27)$$

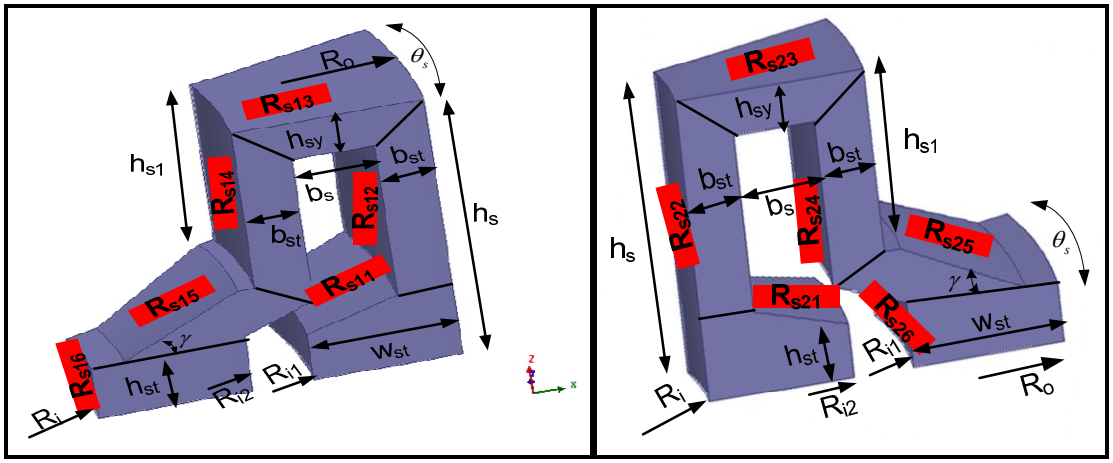

(a) (b)

Fig.4.16: Stator reluctances, (a) first core and (b) second core.

- The reluctance *RS14*

$$R_{S14}=\frac{h_{s1}+h_{sy}}{\mu_0\mu_{r11}(B)\frac{2\pi}{p}\alpha\left((R_o-b_s-b_{st})^2-(R_o-b_s-2b_{st})^2\right)} \quad (4.28)$$

- The reluctance *RS15*

$$R_{S15}=\frac{\left(\left(R_o-\frac{3}{2}b_{st}-b_s\right)-\left(R_i+\frac{w_{st}}{2}\right)\right)\cos\gamma}{\mu_0\mu_{r11}(B)\frac{2\pi}{p}\alpha\left(R_o-b_s-\frac{3}{2}b_{st}\right)b_{st}} \quad (4.29)$$

- The reluctance *RS16*

$$R_{S16}=\frac{h_{st}}{\mu_0\mu_{r11}(B)\frac{2\pi}{p}\alpha\left((R_i+w_{st})^2-R_i^2\right)} \quad (4.30)$$

In the same way, the total reluctance of the second stator is the sum of all stator portions as fellow:

$$R_{S2}=R_{S21}+R_{S22}+R_{S23}+R_{S24}+R_{S25}+R_{S26} \quad (4.31)$$

- The reluctance *RS21*

$$R_{S21}=\frac{h_{st}}{\mu_0\mu_{r21}(B)\frac{2\pi}{p}\alpha\left(R_o^2-(R_o-w_{st})^2\right)} \quad (4.32)$$

- The reluctance RS_{22}

$$R_{S22} = \frac{h_S - \frac{1}{2}h_{sy} - h_{st}}{\mu_0 \mu_{r21}(B)\frac{2\pi}{p}\alpha\left(R_i + \frac{b_{st}}{2}\right)b_{st}} \tag{4.33}$$

- The reluctance RS_{23}

$$R_{S23} = \frac{b_{st} + b_s}{\mu_0 \mu_{r21}(B)\frac{2\pi}{p}\alpha h_{sy}\dfrac{b_{st} + b_s}{\ln\left(\dfrac{R_i + b_s + b_{st}}{R_i + \dfrac{b_{st}}{2}}\right)}} \tag{4.34}$$

- The reluctance RS_{24}

$$R_{S24} = \frac{h_s + \frac{1}{2}h_{sy}}{\mu_0 \mu_{r21}(B)\frac{2\pi}{p}\alpha b_{st}\left(R_i + b_s + \frac{3}{2}b_{st}\right)} \tag{4.35}$$

- The reluctance RS_{25}

$$R_{S25} = \frac{h_s - h_{st} - \frac{1}{2}h_{sy}}{\mu_0 \mu_{r21}(B)\frac{2\pi}{p}\alpha\left(\left(R_i + b_{st}\right)^2 - R_i^2\right)} \tag{4.36}$$

- The reluctance RS_{26}

$$R_{S26} = \frac{h_{st}}{\mu_0 \mu_{r21}(B)\frac{2\pi}{p}\alpha\left(\left(R_i + w_{st}\right)^2 - R_i^2\right)} \tag{4.37}$$

4.4.2 Rotor Yoke Reluctances

Rotor reluctances consist of normal and tangential components.

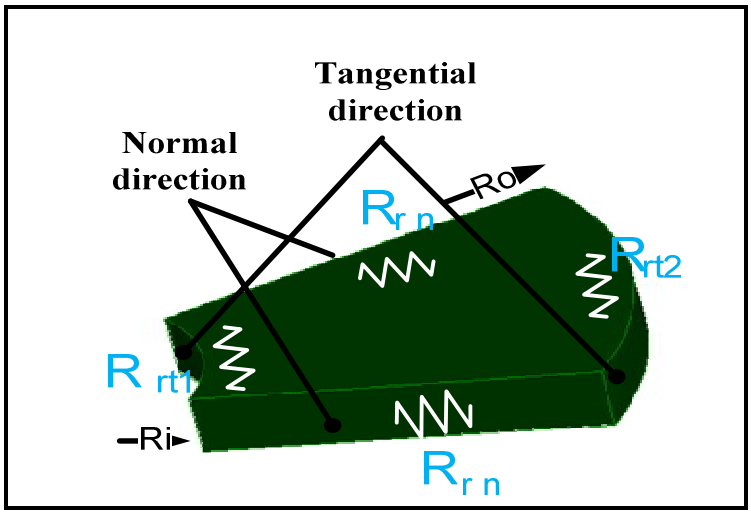

Fig.4.17: Rotor Reluctances.

- In the normal direction

$$R_{rn}=\frac{l_{rn}}{\mu_0\mu_{rr}(B)\frac{2\pi}{p}\int_{R_i}^{R_o}\frac{x}{dx}R_o-R_i-l_m}=\frac{R_o-R_i-l_m}{\mu_0\mu_{rr}(B)\frac{2\pi}{p}\frac{h_r(R_o-R_i-l_m)}{\ln\left(\frac{R_o}{R_i}\right)}} \quad (4.38)$$

- In the tangential direction
  - Reluctance rotor for outer diameter

$$R_{rt1}=\frac{\frac{(R_i+l_m/2)}{2}\frac{2\pi}{p}}{\mu_0\mu_{rr}(B)h_r\left(\frac{R_o-R_i}{2}\right)} \quad (4.39)$$

  - Reluctance rotor for inner diameter

$$R_{rt2}=\frac{\frac{(R_o-l_m/2)}{2}\frac{2\pi}{p}}{\mu_0\mu_{rr}(B)h_r\left(\frac{R_o-R_i}{2}\right)} \quad (4.40)$$

4.4.3 Permanents Magnets Reluctances

The permanents magnets of A-TFPMSM have two PM groups, first outer and second inner. The sections of them aren't equal as shown in Fig.4.18.

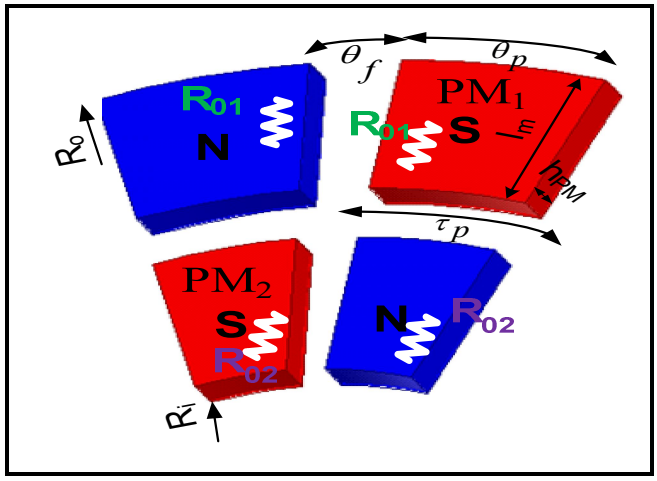

Fig.4.18: Permanents magnets reluctances.

- Reluctance of PM_1

$$R_{01}=\frac{h_{PM}}{\mu_0\mu_{rPM}\tau_p\left(R_o^2-(R_o-l_m)^2\right)-\theta_f\left(R_o^2-(R_o-l_m)^2\right)} \quad (4.41)$$

- *Reluctance of PM2*

$$R_{02} = \frac{h_{PM}}{\mu_0 \mu_{rPM} \alpha \left(\left(R_i + l_m \right)^2 - R_i^2 \right)} \tag{4.42}$$

4.4.4 Leakage Reluctances

Similarly of the rotor yoke reluctances, the leakage reluctances have two components:

1) The total leakage in the tangential direction (outer diameter) in done by:

$$R_{Lt1} = R_{mmt1} + R_{mgt1} + R_{cct1} \tag{4.43}$$

Where: R_{mmt1}, R_{mgt1} and R_{cct1} are the magnet to magnet neighbor, magnet to core and core to core, respectively.

- The magnet to magnet leakage reluctance R_{mmt1}

$$R_{mmt1} = \frac{\pi}{\mu_0 l_m \ln\left(1 + \frac{\pi g}{\tau_1}\right)} \tag{4.44}$$

Where $\tau_1 = \theta_f \left(R_o - \frac{l_m}{2} \right)$

- The magnet to stator core leakage reluctance R_{mgt1}

$$R_{mgt1} = \frac{4 l_{mgt1}}{\mu_0 S_{mgt1}} = \frac{4\pi \frac{h_{PM}}{2}}{\mu_0 \alpha \frac{2\pi}{2} \left(R_o - \frac{l_m}{2} \right) h_{PM}} \tag{4.45}$$

- The magnet to stator core leakage reluctance R_{cct1}

$$R_{cct1} = \frac{l_{cct1}}{\mu_0 S_{cct1}} = \frac{\theta_f \left(R_i - \frac{l_m}{2} \right)}{\mu_0 w_{st} h_{st} + b_{st} h} \tag{4.46}$$

2). The total leakage in the tangential direction (inner diameter) in done by:

$$R_{Lt2} = R_{mmt2} + R_{mgt2} + R_{cct2} \tag{4.47}$$

- The magnet to magnet leakage reluctance R_{mmt2}

$$R_{mmt2} = \frac{\pi}{\mu_0 l_m \ln\left(1 + \frac{\pi g}{\tau_2}\right)} \tag{4.48}$$

Where $\tau_2 = \theta_f \left(R_i + \frac{l_m}{2} \right)$

- The magnet to stator core leakage reluctance R_{mgt1}

$$R_{mgt1} = \frac{4l_{mgt1}}{\mu_0 S_{mgt1}} = \frac{4\pi \frac{h_{PM}}{2}}{\mu_0 \alpha \frac{2\pi}{2}\left(R_i + \frac{l_m}{2} \right) h_{PM}} \tag{4.49}$$

- The magnet to stator core leakage reluctance R_{cct1}

$$R_{cct2} = \frac{l_{cct2}}{\mu_0 S_{cct2}} = \frac{\theta_f \left(R_i + \frac{l_m}{2} \right)}{\mu_0 w_{st} h_{st}} \tag{4.50}$$

3) The leakage of permanent magnet

- Leakage magnet*:* R_{LPM1}

$$R_{LPM1} = \frac{h_m}{\mu_o \theta_f \left(R_o - \frac{l_m}{2} \right) l_m} \tag{4.51}$$

- Leakage magnet*:* R_{LPM2}

$$R_{LPM2} = \frac{h_m}{\mu_0 \theta_f \left(R_i + \frac{l_m}{2} \right) l_m} \tag{4.52}$$

4.4.5 Air-gap Reluctances

$$R_{gap1} = \frac{l_{gap}}{\mu_0 S_{gap1}} \tag{4.53}$$

$$R_{gap2} = \frac{l_{gap}}{\mu_0 S_{gap2}} \tag{4.54}$$

$$R_{gap} = \frac{\left(R_{gap1} + R_{gap2} \right)}{2} \tag{4.55}$$

l_{gap}: The air-gap reluctance of each divided elements.

S_{gap}:Air-gap areas that perpendicular to the air-gap flux path of every divided elements.

4.5 Solving Method

In Fig. 4.19 we are trying to convert 3D MEC to another 2D development MEC to simplified Kirchhoff loops equations.

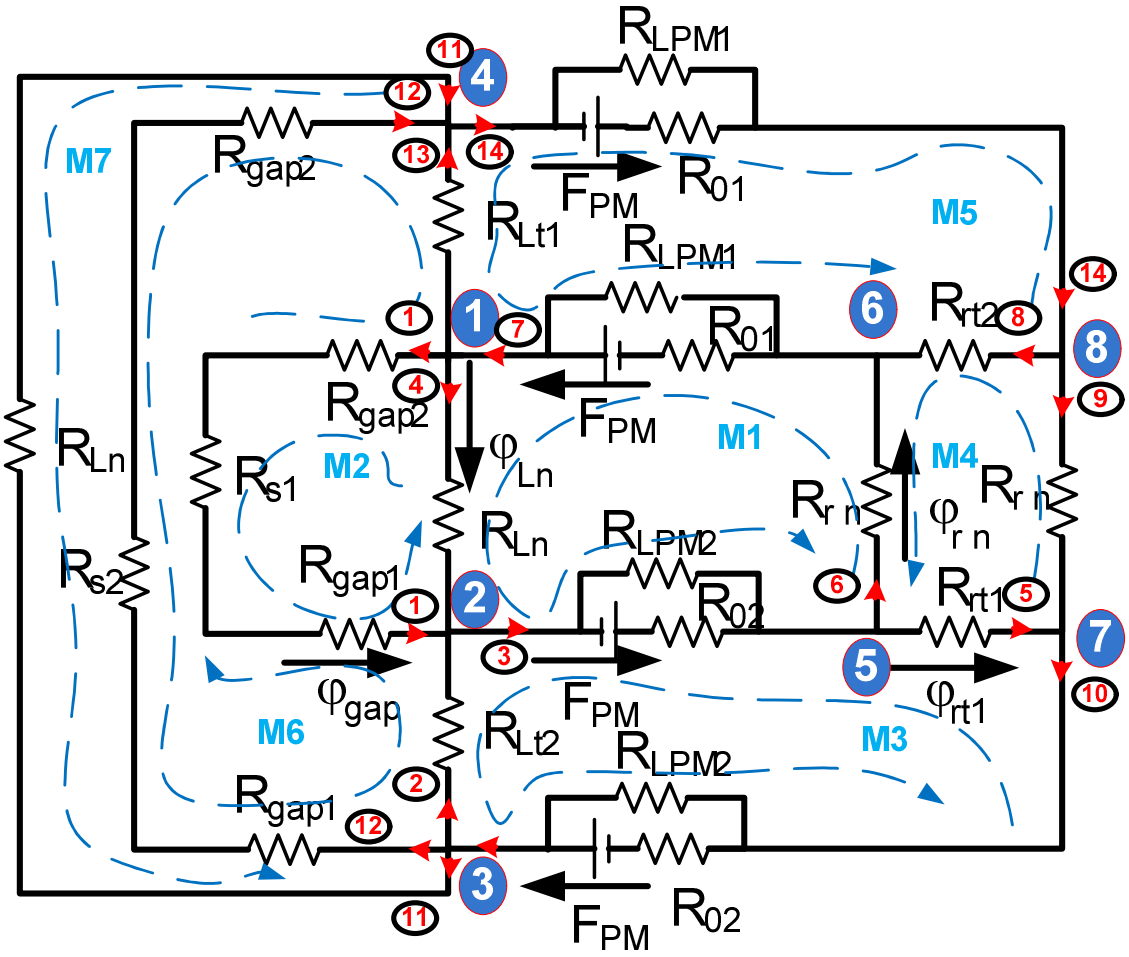

Fig. 4.19: MEC model with it branches and loops.

The basic equations for each element of the equivalent magnetic circuit loop in Fig. 4.19 are as follows:

1- By using Kirchhoff's law the flux equations in the different parts of the machine is:

$$\begin{cases} \Phi_{gap} = \Phi_{PM2} - \Phi_{Ln} - \Phi_{Lt2} \\ \Phi_{PM1} = \Phi_{rt2} + \Phi_{rn} \\ \Phi_{PM2} = \Phi_{rt1} + \Phi_{rn} \end{cases} \tag{4.56}$$

Where $\boldsymbol{\Phi_{gap}}$ is the main magnetic flux, $\boldsymbol{\Phi_{PM1}}, \boldsymbol{\Phi_{PM2}}$ are the permanent magnet flux, $\boldsymbol{\Phi_{Lt2}}$, $\boldsymbol{\Phi_{Ln}}$ are the air-gap flux leakage in the tangential and normal directions respectively, $\boldsymbol{\Phi_{rt1}}$, $\boldsymbol{\Phi_{rt2}}$ and $\boldsymbol{\Phi_{rn}}$ are the flux in the rotor in the tangential and in the normal directions respectively.

2- The *MMF* equations achieved by using Ohm's law for magnetic circuits yields:

$$\begin{cases} 0 = 2\Phi_{Ln}R_{Ln} - \Phi_{Lt1}R_{Lt1} - \Phi_{Lt2}R_{Lt2} \\ 0 = 2\Phi_{rn}R_{rn} - \Phi_{rt1}R_{rt1} - \Phi_{rt2}R_{rt2} \\ 0 = \Phi_{Ln}R_{Ln} - \Phi_{gap}\left(R_{s1} + R_{gap}\right) \end{cases} \quad (4.57)$$

Where the reluctances, $\boldsymbol{R_{Ln}}$, $\boldsymbol{R_{Lt1}}$ and $\boldsymbol{R_{Lt2}}$, are the air-gap leakage reluctance in the normal and in the tangential direction, respectively. $\boldsymbol{R_{rn}}$, $\boldsymbol{R_{rt1}}$ and $\boldsymbol{R_{rt2}}$ are the rotor core reluctances in the normal and in the tangential direction, respectively. And R_{s1} and R_{s2} is the all stator core unit reluctance. $\boldsymbol{R_{gap}}$ is the air-gap reluctance.

Where $$R_{gap} = \left(R_{gap1} + R_{gap2}\right) \Big/ 2$$

The *MMF* of the permanent magnet is defined in equation (4.20)

$$\begin{cases} F_{PM} = \left(2\Phi_{PM2}R_{eq2} + \Phi_{Lt2}R_{Lt2} + \Phi_{rt1}R_{rt1}\right)/2 \\ F_{PM} = \left(2\Phi_{PM1}R_{eq1} + \Phi_{Lt1}R_{Lt1} + \Phi_{rt2}R_{rt2}\right)/2 \\ 2F_{PM} = \left(\Phi_{PM1}R_{eq1} + \Phi_{PM2}R_{eq2} + \Phi_{Ln}R_{Ln} + \Phi_{rn}R_{rn}\right) \\ 2F_{PM} = \left(\Phi_{PM1}R_{eq1} + \Phi_{PM2}R_{eq2} + \Phi_{gap}(R_{gap} + R_{s2}) + \Phi_{rn}R_{rn}\right) \end{cases} \quad (4.58)$$

Where $\boldsymbol{R_{eq1}}$ and $\boldsymbol{R_{eq1}}$ are the permanent magnet leakages equivalents reluctances.

The permanent magnet leakage equivalent reluctance can be written as:

$$\begin{cases} R_{eq1} = R_{LPM1} // R_{01} = R_{LPM1}R_{01}/\left(R_{LPM1} + R_{01}\right) \\ R_{eq2} = R_{LPM2} // R_{02} = R_{LPM2}R_{02}/\left(R_{LPM2} + R_{02}\right) \end{cases} \quad (4.59)$$

Where $\boldsymbol{R_{01}}$ and $\boldsymbol{R_{02}}$ are the permanent magnet reluctance, $\boldsymbol{R_{LPM1}}$ and $\boldsymbol{R_{LPM2}}$ are the permanent magnet leakages reluctances.

By arranging of above equations, the main flux in the air-gap is achieved as:

$$\Phi_{gap} = \frac{2F_{PM}\left(R_{10}R_{12} - R_{13}R_{11}\right)}{R_{10}R_{14} - R_{13}R_{9}} \quad (4.60)$$

Where R_9, R_{10}, R_{11}, R_{12}, R_{13} and R_{14} are provided in Appendix I.

The variation of the air-gap reluctance $\boldsymbol{R_{gap}}$ is a function of the rotor position, which can be obtained as:

$$R_{gap} = \frac{1}{\mu_0 h_{PM}} \int_0^{h_{PM}} \frac{g(z)}{dz} \tag{4.61}$$

Where *g(z)* is the function of air-gap length.

In order to validate the concept method, a MEC has been established, the resulting circuit is shown in Fig.4.19 where the main and leakage flux paths are shown by arrows.

The determination of each flux is achieved through the Hopkinson law which is expressed as follows

$$F = R\Phi \tag{4.62}$$

Where $\boldsymbol{R}$, $\boldsymbol{F}$ and $\boldsymbol{\Phi}$ are matrix reluctance, MMF and flux, respectively.

$$R = \begin{bmatrix}
R_1 & 0 & 0 & 0 & 0 & 0 & 0 & 0 & 0 & 0 & 0 & 0 & 0 & 0 \\
0 & R_2 & 0 & & & & & & & & & & & 0 \\
0 & 0 & R_3 & 0 & & & & & & & & & & 0 \\
0 & & 0 & R_4 & 0 & & & & & & & & & 0 \\
0 & & & 0 & R_5 & 0 & & & & & & & & 0 \\
0 & & & & 0 & R_6 & 0 & & & & & & & 0 \\
0 & & & & & 0 & R_7 & 0 & & & & & & 0 \\
0 & & & & & & 0 & R_8 & 0 & & & & & 0 \\
0 & & & & & & & 0 & R_9 & 0 & & & & 0 \\
0 & & & & & & & & 0 & R_{10} & 0 & & & 0 \\
0 & & & & & & & & & 0 & R_{11} & 0 & & 0 \\
0 & & & & & & & & & & 0 & R_{12} & 0 & 0 \\
0 & & & & & & & & & & & 0 & R_{13} & 0 \\
0 & 0 & 0 & 0 & 0 & 0 & 0 & 0 & 0 & 0 & 0 & 0 & 0 & R_{14}
\end{bmatrix} \tag{4.63}$$

Knowing the number of the nodes and of the loops of the circuit in Fig.4.19, we will determine the numbers of independent loops that are set up in matrix form.

The reluctance matrix is a diagonal square matrix composed by the reluctances of different branches of the circuit with dimensions of 14*14. The matrix of the MMF is a matrix ***m*1*** such that ***m=7*** is the number of independent loops of the

circuit. The matrix of flux is matrix of ***n*1*** dimension with ***n=14*** is number of legs.

Where

$$\begin{cases} R_1 = R_{s1} + R_{gap1} + R_{gap2} \\ R_2 = R_{Lt1} \\ R_3 = R_{PM2} \\ R_4 = R_{Ln} \\ R_5 = R_{rt1} \\ R_6 = R_{rn} \\ R_7 = R_{PM1} \end{cases} \quad \text{And} \quad \begin{cases} R_8 = R_{rt2} \\ R_9 = R_{rn} \\ R_{10} = R_{PM2} \\ R_{11} = R_{Ln} \\ R_{12} = R_{s2} + R_{gap1} + R_{gap2} \\ R_{13} = R_{Lt2} \\ R_{14} = R_{PM1} \end{cases} \tag{4.64}$$

The MMF flux law can be derived as follows and the magnetomotric matrix F is written as:

$$F = \begin{bmatrix} -F_{PM1} + F_{PM2} \\ 0 \\ -F_{PM2} - F_{PM2} \\ 0 \\ -F_{PM1} - F_{PM1} \\ 0 \\ 0 \end{bmatrix} \tag{4.65}$$

And the branch matrix flux $\boldsymbol{\phi}$ is written as:

$$\Phi^T = \begin{bmatrix} \phi_1 & \phi_2 & \phi_3 & \phi_4 & \phi_5 & \phi_6 & \phi_7 & \phi_8 & \phi_9 & \phi_{10} & \phi_{11} & \phi_{12} & \phi_{13} & \phi_{14} \end{bmatrix} \tag{4.66}$$

Where

$$\begin{cases} \phi_1 = \phi_{gap} \\ \phi_2 = \phi_{Lt1} \\ \phi_3 = \phi_{PM2} \\ \phi_4 = \phi_{Ln} \\ \phi_5 = \phi_{rt1} \\ \phi_6 = \phi_{rn} \\ \phi_7 = \phi_{PM1} \end{cases} \quad \text{and} \quad \begin{cases} \phi_8 = \phi_{rt2} \\ \phi_9 = \phi_{rn} \\ \phi_{10} = \phi_{PM2} \\ \phi_{11} = \phi_{Ln} \\ \phi_{12} = \phi_{gap} \\ \phi_{13} = \phi_{gap} \\ \phi_{14} = \phi_{PM1} \end{cases} \tag{4.67}$$

To solve above equation we use this matrix form

$$\Phi = S^T \left(SRS^T \right)^{-1} F \tag{4.68}$$

Where **S** is the connectivity matrix, enabling a matrix representation of Kirchhoff's laws. This matrix has ***m*** rows and ***n*** columns.

$$S=\begin{bmatrix} 0 & 0 & 1 & 1 & 0 & 1 & 1 & 0 & 0 & 0 & 0 & 0 & 0 & 0 \\ 1 & 0 & 0 & -1 & 0 & 0 & 0 & 0 & 0 & 0 & 0 & 0 & 0 & 0 \\ 0 & -1 & -1 & 0 & -1 & 0 & 0 & 0 & 0 & -1 & 0 & 0 & 0 & 0 \\ 0 & 0 & 0 & 0 & 1 & -1 & 0 & 1 & -1 & 0 & 0 & 0 & 0 & 0 \\ 0 & 0 & 0 & 0 & 0 & 0 & -1 & -1 & 0 & 0 & 0 & 0 & -1 & -1 \\ -1 & 1 & 0 & 0 & 0 & 0 & 0 & 0 & 0 & 0 & 0 & -1 & 1 & 0 \\ 0 & 0 & 0 & 0 & 0 & 0 & 0 & 0 & 0 & 0 & 0 & -1 & 1 & 0 \end{bmatrix} \quad (4.69)$$

To solve MEC model, a numerical procedure is developed. Both the position and the reluctance are varying, as in the flowchart in Fig.4.20.

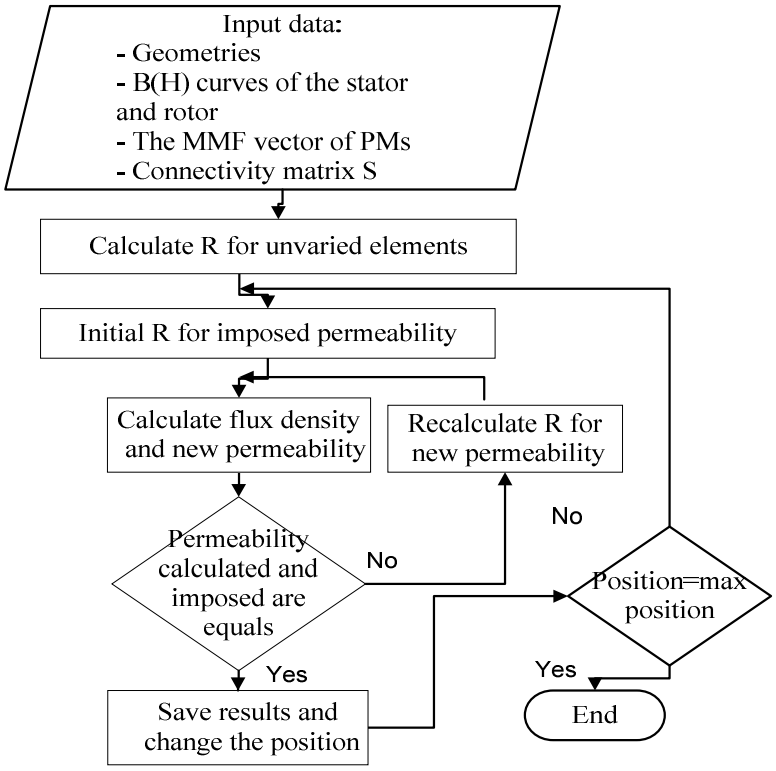

Fig.4.20: Flowchart of procedure used for solving the MEC model.

In Fig.4.20 the numerical solution of the MEC procedure is started by geometrical and material data insertion, including the relative permeability, next the calculation of initial reluctances is made. By using equation (4.68) the flux is achieved. Then the relative permeability is computed again by using the

B (H) curves. The Φ_{gap} results in the previous process are used in the next steps to computed both the EMF and the torque.

4.6 MEC and 3D Finite Elements Results

The computations of the air gap flux density by using FEA and MEC are represented in Fig. 4.21, where a good agreement is achieved for both results.

In Fig.4.21, the torque generated by FEA and MEC at different current values and in the position where the stator core are fully aligned to the rotor pole, calculated by using Equation (20), are shown; the results of the proposed method are in good accordance with the FEA simulation.

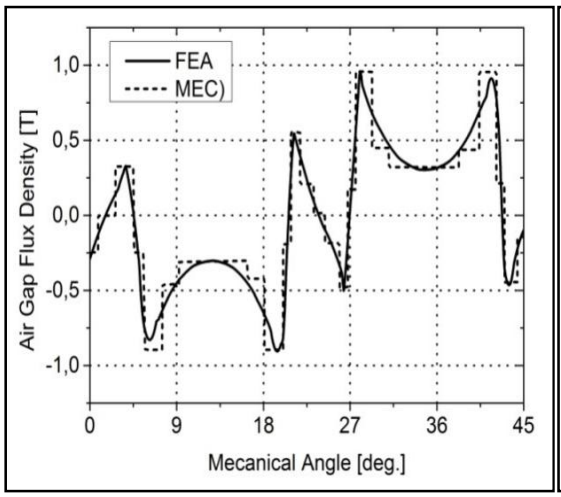

Fig.4.21: Air-gap flux density distribution.

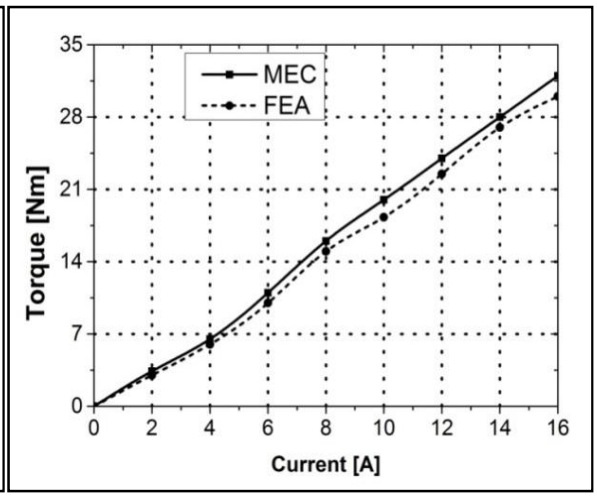

Fig.4.22: Average torque with stator current of A-TFPMSM.

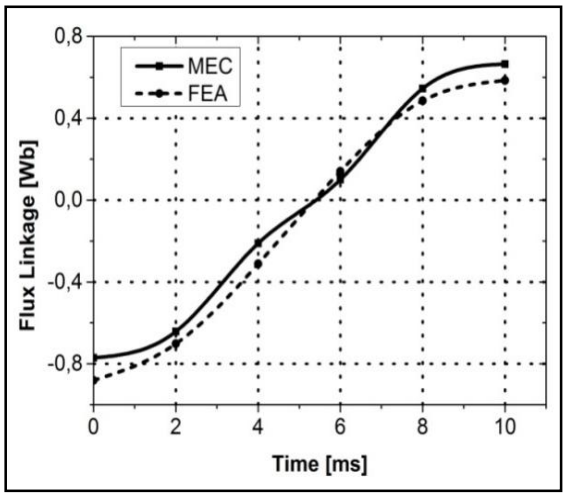

Fig.4.23: Flux linkage at no-load by FEA and MEC.

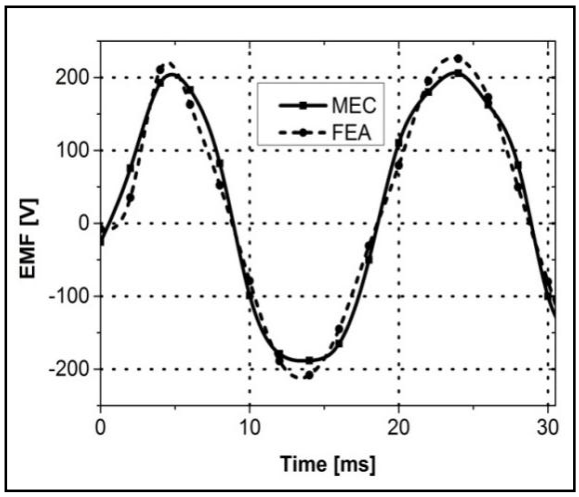

Fig.4.24: No-load back EMF of A-TFPMSM. For FEA and MEC.

The no-load back EMF of the machine at 375 r/min rotation speed for both analyses are shown in Fig.4.24.By using equation (2.10), the EMF rms is E=200V.The waveform of FEA is lower than the waveform of MEC, as the MEC analysis inevitably neglects some of the leakage flux lines The flux linkage at no-load for different position achieved from both MEC and FEA analyses are shown in Fig. (4.23), the flux linkage is larger at 0 ms when the stator core and permanent magnet pole are fully opposite; the flux linkage is smallest at 6 ms when the stator core unit located between two poles.

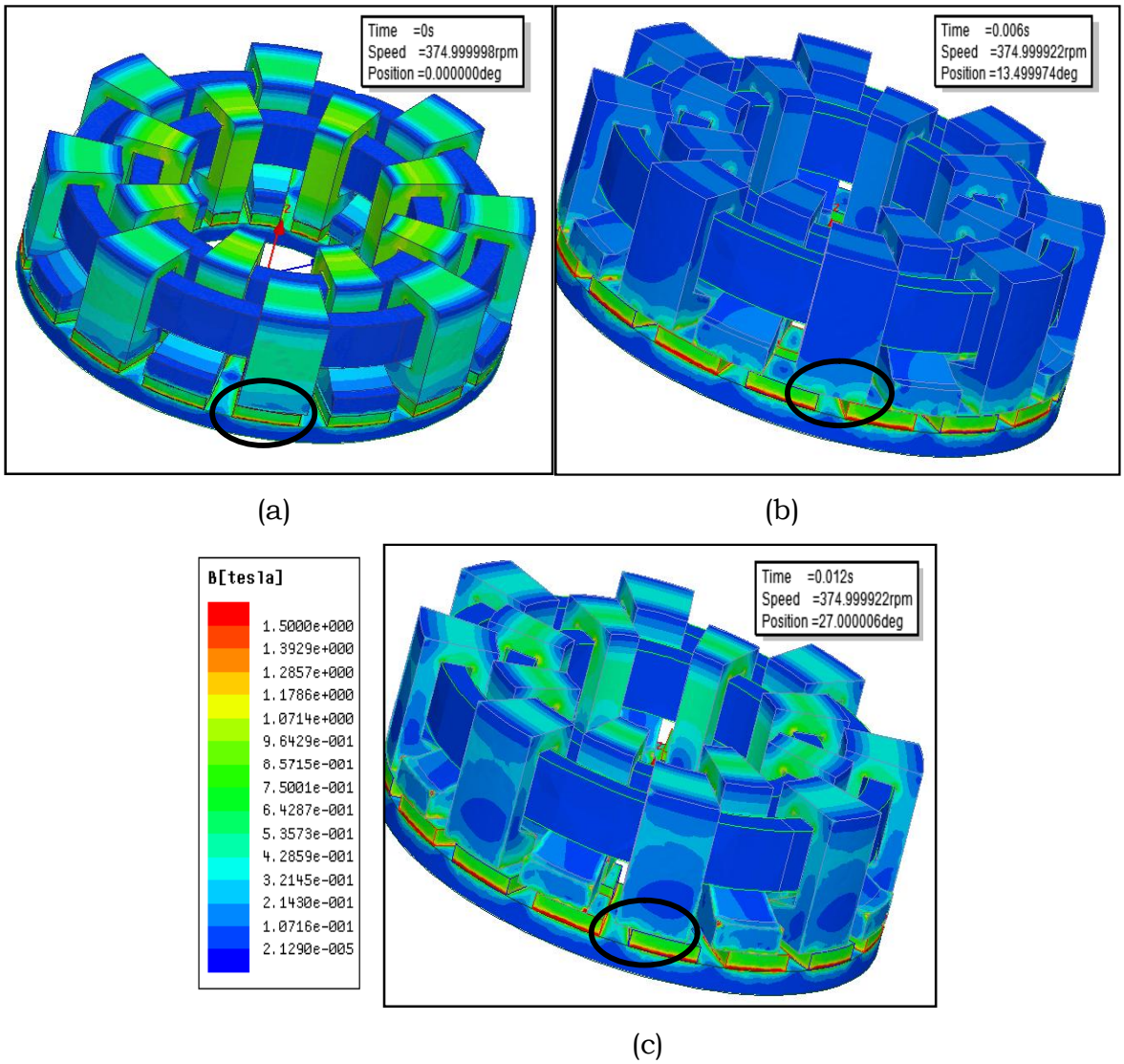

Fig.4.25: Flux density distribution of A-TFPMSM:(a)Stator core aligned to the magnetic poles; (b) Stator core between two poles and (c) Stator core nearly almost opposite to the magnet poles.

In state one Fig.4.25 (a) the stator core unit is aligned to the closest rotor poles. In this case, the stator core flux density is 1T and the air-gap flux density is 0.78 T. In state two Fig. 4.25 (c) the stator core unit is nearly aligned to the rotor poles and the flux lines generated by the permanent magnets cross the air-gap. In this case, the stator core flux density is 0.6 T. In state three Fig.4.25 (b), the stator core unit is located between two rotor poles and the flux line generated by the permanent magnet cross the air-gap, and in this case the stator core flux density is 0.35T. The magnetic conditions of the A-TFPMSM prototype are acceptable, showing no significant saturation area in the design.

2.7 Conclusion

Engineering judgment is used to establish the principal flux paths and model the machine in sufficient detail to pony only the salient magnetic properties However, using the MEC approach, the offsets of magnetic saturation are obtained directly from knowledge of the material characteristics and machine geometry, as in the FEM model.

The developed MEC of novel A-TFPMSM has been used for the analyses of the air-gap flux density, of the no-load back EMF and of the flux linkage. In order to validate the analysis, a 3-D FEM simulation is used.

In this chapter provides a description of the A-TFPM machine design, that utilize a two-dimensional, reluctance network to represent the magnetic stat of this system. In beginning, in the linear magnetic region, the MEC method is presented and compares it's with 2D FEA, compare favorably with our wishes. However, when the machine operates at high levels of magnetic flux, the MEC model shows poor agreement with FEA analyses.

In addition the using a magnetic equivalent model to predict output performance of electric machinery. Air gap flux density results from MEC method are presented and good agreement with FEA simulation, and demonstrate the capability of the MEC method.

Bibliography -4-

[1] D. SVECHKARENKO. “On Design and Analysis of a Novel Transverse Flux Generator for Direct-driven Wind Application”. Doctoral Thesis. Stockholm, Sweden 2010.

[2] A. Reinap. “Design of Powder Core Motors”. Doctoral Thesis. Stockholm, Sweden 2004.

[3] F. M. Sargos and A. Rezzoug. “Calcul analytique du champ engendré par des aimants dans l'entrefer d'une machine à rotor denté”. Journal de Physique III, 1(1) :103-110, Jan 1991.

[4] Z. Zhu, D. Howe, E. Bolte, et B. Ackermann. “Instantaneous magnetic field distribution in brushless permanent magnet DC motors”. I. Open-circuit field”. Magnetics, IEEE Transactions on, 29(1):124-135, 1993.

[5] V. Ostovic. “Dynamics of Saturated Electric Machines”. Springer Verlag, 1989.

[6] L. Albert. Modélisation et optimisation des alternateurs à grifes. Application au domaine automobile”. Thèse de Doctorat, 2004.

[7] Z. Zhu, Y. Pang, D. Howe, S. Iwasaki, R. Deodhar, and A. Pride. “Analysis of electromagnetic performance of flux-switching permanent magnet Machines by nonlinear adaptive lumped parameter magnetic circuit model”. Magnetics, IEEE Transactions on, 41(11):4277-4287, 2005.

[8] M. Hecquet and P. Brochet. “Modélisation d'un alternateur automobile par un réseau de perméances couplé à des circuits électriques”. J. Phys. III France, 6:1099-1116, 1996.

[9] E. Lovelace. “Optimization of a magnetically saturable interior permanent-magnet synchronous machine drive”. Thèse de Doctorat, 2000.

[10] W. H. Hayt, “Engineering Electromagnetics”, McGraw-Hill, New York, 1989.

[11] V. Lionel. “Etude d'actionneurs électriques a double excitation destinées au transport. Dimensionnement de structures synchrones”. Thèse de Doctorat, ENS CACHAN, 2004.

[12] C. Delforge-Delmotte and B. Lemaire-Semail. “Modélisation d'une machine asynchrone par réseaux de perméances en vue de sa commande”. J. Phys. III France, 6 :17851809, 1996.

[13] N. Bernard, H. Ben Ahmed, and B. Multon. “Semi-analytical inductance calculation on an axial-field synchronous machine for a flywheel storage system using surface permeances”. Electric Machines and Drives Conference, 2001. IEMDC 2001. IEEE International, pages 382390, 2001.

[14] C. Bernez. “Conception et modélisation dactionneurs électriques à très forte accélération : application aux soupapes électromagnétiques”. Thèse de Doctorat, SATIE ENS Cachan, France, 2006.

[15] S. Hlewi, “Etude dune machine a double excitation”. Thèse de Doctorat, Universite de Besancon, 2009.

[16] Z. Zhong, S Jiang and G. Zhang. “Magnetic Equivalent Circuit Model of Interior Permanent-Magnet Synchronous Machine Considering Magnetic Saturation”. EVS28, kintex, Korea, May 3-6, 2015.

Conclusion

The work presented in this thesis deals with the study of the axial-transverse flux permanent magnets machine (A-TFPMSM). The quasi-U stator core is very useful for this type of machine, as that core is easy to be manufactured and each of the three phase windings contributes separately to the generation of the electromagnetic torque. An initial design program is developed for generate quickly the machine dimensions. The next attempt is developed the machine model, the model of Axial-transverse PMs synchronous machine is based upon magnetic equivalent circuit techniques (MEC), using a reluctance network to model the flux path within the A-TFPMS machine. Output results show good agreement with finite element analyses (FEA). This A-TFPMSM topology was investigated because it is believed to yield reduction in manufacturing cost.

After critically reviewing previously proposed designs of radial, axial and transverse flux machines, a special type of axial-transverse flux permanents magnets machine having quasi-U core in the stator, two permanents magnets groups in the rotor and ring type winding was invented. The invention is based on the flux direction required for the machine's construction, and also because of the flux surface mounted construction (which surface mounted magnets was found preferable compared to flux concentrated at low speed). The back iron rotor and magnets two groups' thirty-two identical core parts (or sixteen parts with two different diameters) build up the rotor. The stator is equally simple with three half ring coils and twelve identical core parts (or six parts with two different layouts). The core parts are made of iron silicon or Soft Magnetic Composites (SMC); consisting of iron powder particles that are individually insulated and can be readily pressed into complex geometries. Furthermore, A-TFPMSM stator cores can use steel laminations, because the path of magnetic flux lines is two dimensional. Iron core loss is reduced in this way while the magnetic flux density is increased.

This A-TFPMSM machine is single face can be compensated by using the second configuration of this machine. This configuration leads to the multidisc or multistage A-TFPMSM model proposed in this thesis. In this configuration, the stator core pitch and the rotor magnet pole pitch are equal, maximizing the torque density and the flux linkage, and obviously minimizing the leakage flux.

To obtain accurate design results, finite element analysis is necessary. The traditional 2-D model isn't suitable for an accurate simulation as the magnetic flux leakage of A-TFPMSM between adjacent poles is significant. A 3-D finite element analysis is therefore necessary; The FEA of the axial transverse flux machine provides the magnetic flux density values in the different sections of machine at load and no-load conditions. The flux density values are within normalized design intervals, the magnetic flux density distributions are shown.

The results obtained were studied and allowed to validate the design methodology. Then, we moved to a gradual improvement of the different magnetic models of the machine. After modeling the ferromagnetic parts of the machine, we integrated the phenomenon of magnetic saturation and magnetic leakage. At each stage of the modeling, the results obtained were compared with those determined by FEA simulations. The developed MEC of novel A-TFPMSM has been used for the analyses of the air-gap flux density, of the no-load back EMF and of the flux linkage.

Future Work

- *Improving the analytical model. There was still some disagreement between the results from the improved analytical model and FEM-simulated results. In order to improve the analytical model the reluctance paths, that have been derived, can be further divided into several more paths.*
- *Modeling of the temperature distribution would also add to the knowledge, especially useful when designing the winding and the cooling system.*
- *Optimal length of the magnet. Use the improved analytical model together with FEM analysis in order to find an optimal length ratio between the length of the pole and the length of the magnet.*
- *Other alternative applications for A-TFPMS machines should be investigated, for example, a large motor for direct-drive traction applications. A high power factor would still be important but for such an application the number of poles could be higher (40-80 number of poles) as the frequency (and speed) would be much lower (about 50 rpm).*
- *Alternative building of A-TFPMS to give more reality on our invention.*